# MECHANISTIC AND KINETIC STUDIES ON $F_{420}H_2$: $NADP^+$ OXIDOREDUCTASE FROM *ARCHEOGLOBUS FULGIDUS*

by

CUONG QUANG LE

Presented to the Faculty of the Graduate School of

The University of Texas at Arlington in Partial Fulfillment

of the Requirements

for the Degree of

DOCTOR OF PHILOSOPHY

THE UNIVERSITY OF TEXAS AT ARLINGTON

August 2015

ACKNOWLEDGEMENTS

I would like to thank my research advisor, Professor Kayunta Johnson-Winters for her mentoring, guidance and patience during my period at UT Arlington. It is impossible to go all the way without your initiation and help, both mentally and in research. Your intelligence and determination have positively transformed me into a new person. Your guidance has also effectively and positively helped me to improve my writing skills. Thank you very much. I thank the Department of Chemistry and Biochemistry at UT Arlington and National Science Foundation (NSF) for financially supporting my project and Ph.D. degree. The research was supported by NSF Grant 1120837 (to my research advisor, KJW). I thank my committee members, Prof. Subhrangsu S. Mandal and Prof. Alejandro Bugarin for their direction. I thank Dr. Ebenezer Joseph for his friendly discussions and valuable techniques. I thank my group members (Tijani Osumah, Mercy A. Oyugi, Siqi Du, and Md Hasmat Ullah) for research discussions. One special thanks to Toan Q. Nguyen for his scientific input and participation in my projects. It is a lost to the research community that Toan has decided to attend medical school. I acknowledge my collaborators (Mohammad S. Hossain and his research advisor, Prof. Frank W. Foss, Jr) for organic synthesis and my colleagues (Arunoday K. Bhan, Venkata Adiraju, Munuve Mwania, Hope Umutesi, and Paromita Deb) for helpful discussions.

Last, but not least, I acknowledge my father and mother (Xuan Le and Hoa Le) and siblings (Thai Le, Vinh Le, Phu Le, Christie Le, and Anh Le) who unconditionally, mentally, and financially supported me during my complex and interesting journey to the Ph.D. destination. Thank you all very much! My Ph.D. degree is a product of a catalyst reaction that required my work energy and you all as enzymes and coenzymes.

August 10, 2015

ABSTRACT

MECHANISTIC AND KINETIC STUDIES ON $F_{420}H_2$: $NADP^+$ OXIDOREDUCTASE FROM ARCHEOGLOBUS FULGIDUS

Cuong Quang Le, PhD

The University of Texas at Arlington, 2015

Supervising Professor: Kayunta Johnson-Winters

$F_{420}H_2$: $NADP^+$ Oxidoreductase (Fno) is an $F_{420}$ cofactor dependent enzyme that catalyzes the reversible reduction of $NADP^+$ to NADPH by transferring a hydride from the reduced $F_{420}$ cofactor. $F_{420}$ cofactor is an essential electron transfer carrier in methanogens. Methanogens play a critical role in carbon cycling because the methanogenic pathway reduces carbon dioxide to produce methane and is therefore linked to energy (*1*). The focus of this thesis is to study the hydride transfer mechanism of Fno from the extreme thermophile, *Archeoglobus fulgidus* using site directed mutagenesis, steady-state and pre-steady state kinetic methods.

$F_{420}$ is essential for catalysis within enzymes that are dependent upon this unique cofactor. We are able to purify apoFno and intercalate the cofactor back into the enzyme, and therefore produce active Fno. Our work focuses in part, upon the synthesis of the catalytically active $F_{420}$ precursor, FO (chapter 2), which is much simpler to obtain, with higher purity than previously published methods grown from bacteria. Using the newly synthesized FO, Fno activity was restored in the absence of $F_{420}$. Investigating the FO-dependent $NADP^+$/NADPH redox process by stopped-flow spectrophotometry,

steady-state kinetics were defined as having a $K_m$ of 4.00 ± 0.39 μM and a $k_{cat}$ of 5.27 ± 0.14 $s^{-1}$.

Chapter 3 reports the optimized expression and purification method for recombinant Fno. The Fno gene was optimized for expression in *Escherichia coli*. Modified growth conditions, and purification protocol involving a key polyethyleneimine precipitation step resulted in a highly purified, homogeneous preparation of Fno that displayed high catalytic activity with FO.

Once the key components of the reaction, FO and Fno were easily obtainable, efforts were then focused on rigorous kinetic analysis of the enzyme. We have characterized *wt*Fno, as well as Fno variants using steady state and pre-steady state kinetic methods. We report the very first example of half-site reactivity and negative cooperativity involving an $F_{420}$ cofactor dependent enzyme. While the steady state kinetic analysis showed classic Michaelis-Menten kinetics with varying concentrations of FO, such plots were not displayed with varying NADPH concentrations. When the NADPH steady-state data was converted to a double reciprocal plot, it displayed a downward concave shape, suggesting that negative cooperativity occurs between the two identical monomers. The pre-steady state kinetic data was biphasic, displaying a fast phase and a slow phase. The amplitude of the burst phase corresponds to 50% of FO reduction. This is likely due to only one functional active site at a time, which suggests half-site reactivity.

To kinetically characterize the functionality of the active site I135 residue, we converted it to a glycine, alanine, and valine. The steady-state and pre-steady state kinetic data reveals that decreasing the length of the side chain of the 135$^{th}$ residue decreases $k_1$ and the affinity of the FO cofactor for the enzyme.

TABLE OF CONTENTS

LIST OF FIGURES

LIST OF SCHEMES

LIST OF TABLES

LIST OF ABBREVIATIONS

| | |
|---|---|
| Fno | $F_{420}H_2$: $NADP^+$ oxidoreductase |
| NADPH | Nicotinamide adenine dinucleotide phosphate (reduced form) |
| Fno | $F_{420}$ $H_2$: $NADP^+$ Oxidoreductase |
| $NADP^+$ | Nicotinamide adenine dinucleotide phosphate (oxidized form) |
| *E. coli* | *Escherichia coli* |
| FO | $F_{420}$ cofactor precursor |
| LB | Luria Bertani broth |
| $K_d$ | Dissociation constant |
| $k_{cat}$ | Michaelis-Menten catalytic rate constant (turnover number) |
| SDS-PAGE | Sodium dodecyl sulfate polyacrylamide gel electrophoresis |
| $F_{420}$ | $F_{420}$ cofactor |
| g | Acceleration of gravity |

Chapter 1

# $F_{420}$ DEPENDENT ENZYMES AND THEIR COFACTORS

## 1.1 Introduction

The availability of an unusual electron-transfer coenzyme, known as the $F_{420}$ cofactor (a 7,8-didemethyl-8-hydroxy-5-deazaflavin transferring agent) (Figure 1.1) has been understood to be vital for catalysis in certain enzymes

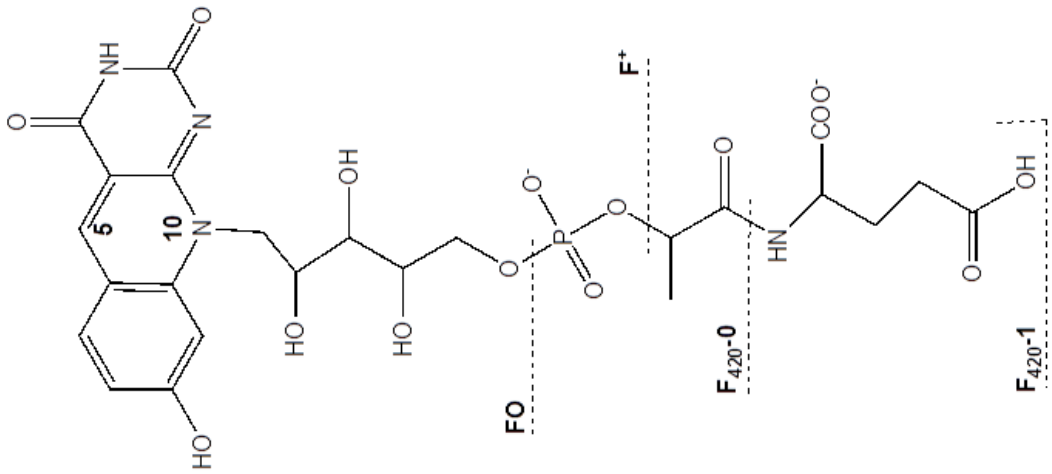


Figure 1.1 $F_{420}$-1 cofactor and its smaller fragments (FO and $F^+$).The only difference is the length of the side chain (*2*).

The $F_{420}$ cofactor is chemically equivalent to $NAD^+$, which is exclusively involved in hydride transfer reactions (Equations 1.1 and 1,2). However, the chemical structure is reminiscent of an isoalloxazine chromophore with a side chain comprising of ribitol, phosphate, and lactate residues as well as a ɣ-linked polyglutamate tail that varies in length ($F_{420}$-1 to $F_{420}$-9), depending upon the species in which the coenzyme is found (3).

$$F_{420}{:}H_2 + XH \rightarrow F_{420} + XH_2 \qquad \text{(Equation 1.1)}$$

$$F_{420} + XH_2 \rightarrow F_{420}{:}H_2 + XH \qquad \text{(Equation 1.2)}$$

The $F_{420}$ cofactor can be oxidized or reduced and is therefore, spectrophotometrically

distinct (Figure 1.2). In a basic solution, the cofactor is oxidized and bright yellow in color, with an absorbance maximum between 401-420 nm (Figure 1.2) (*4, 5*). The oxidized cofactor is an obligate two-electron acceptor under physiological non-photoreductive conditions(*4*).

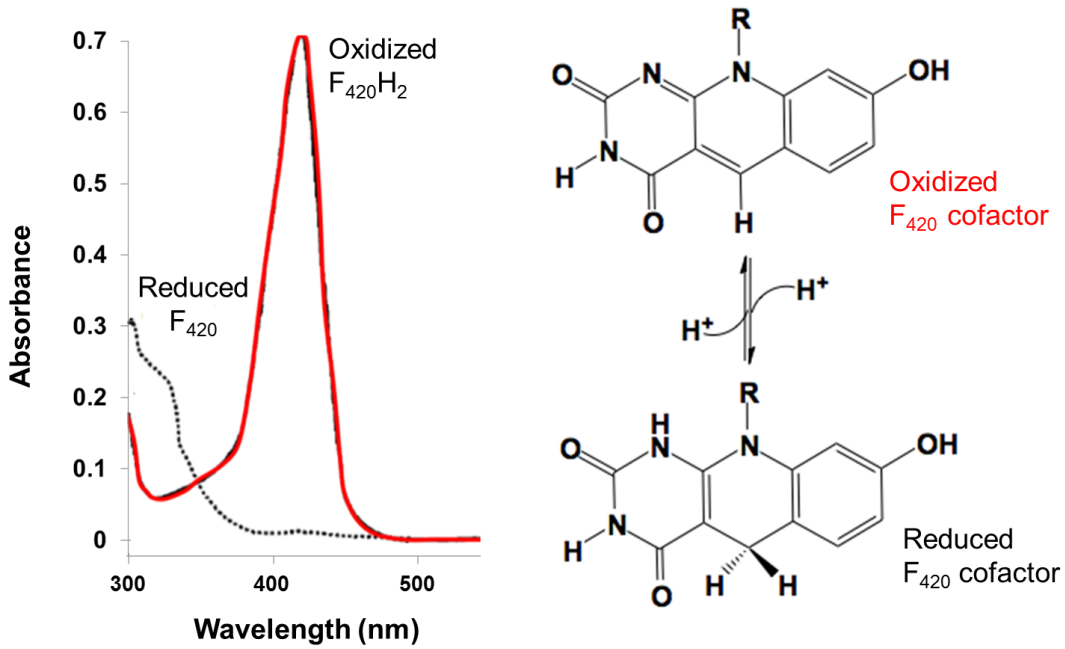


Figure 1.2 Spectra of the oxidized and reduced $F_{420}$ cofactor along with corresponding structures. (A. oxidized $F_{420}$, B. reduced $F_{420}$:$H_2$ cofactor). Data are from Tzeng and other coworkers (*1, 5*).

Upon reduction, it loses the 420 nm absorbance and gains a new absorbance at 320 nm (*1*). with a much lower extinction coefficient (at pH 8.85, $\varepsilon_{420}$ of $F_{420}$ is 45,500 $M^{-1}cm^{-1}$ and at pH 8.8, $\varepsilon_{320}$ of $F_{420}$ $H_2$ is 10,800 $M^{-1}cm^{-1}$ (*6, 7*).Below pH 6.0, the maximum absorbance of the oxidized cofactor shifts from 420 nm towards lower wavelengths (*6, 7*). The isosbestic point between pH 4-10 has been previously determined to be 401 nm. However, as the pH is increased, the hydroxyl proton at the 8 position ($pK_a$ = 6.3) (*6*) of the $F_{420}$ cofactor (Figure 1.3; structure A) is removed, consequently converting the $F_{420}$

cofactor into an anionic form, which has two resonance structures (Figure 1.3; structure B and C) (*8*). These resonance structures attribute for the shifting of the absorbance wavelength *(7*). Also, at a basic pH, another proton is removed from the 3-NH ($pK_a$ = 12.2), resulting in the formation of structure D (Figure 1.3), this also results in absorbance shifts to longer wavelengths (9, 10 ).

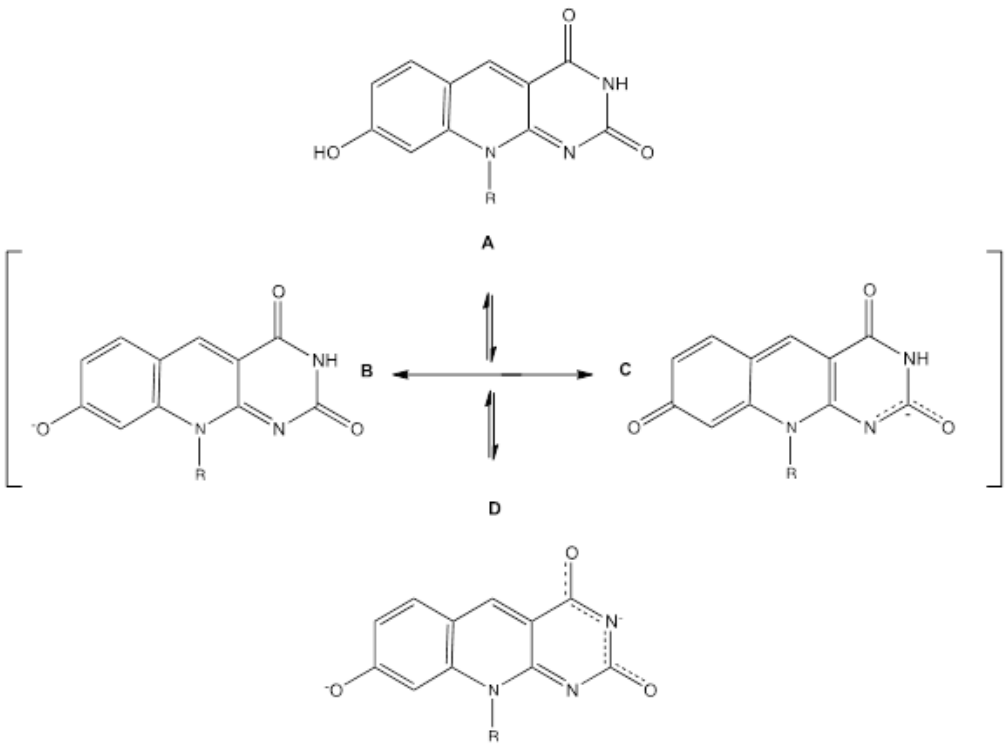


Figure 1.3 Ionization and resonance structure of $F_{420}$ cofactor (7). Removing a proton of the 8-OH group ($pK_a$ = 6.3) (*6*) of the $F_{420}$ cofactor (Structure A) converts $F_{420}$ into an anionic form, which has two resonance forms (Structure B and C) (*7*). These resonance structures are responsible for the shifting of the absorbance wavelength. At highly basic pH, another proton is removed from the 3-NH ($pK_a$ = 12.2) resulting in the formation of structure D and the absorbance shift to a longer wavelength (The maximum peak of the oxidized form will no longer at 420 nm; it is slightly higher than 420 nm wavelength) (*7*).

Similar to the chemical structure, the fluorescence spectral properties of the $F_{420}$ cofactor are also pH and redox sensitive (*1, 7*). The oxidized cofactor has strong fluorescence at 425 nm, while the reduced form does not. FO and $F^+$ (Figure 1.1), two of

several acid-hydrolysis products of the $F_{420}$ cofactor, exhibit spectral properties that are similar to those of the unaltered $F_{420}$ cofactor. However, these hydrolysis products have an extinction coefficient at 420 nm that is approximately 15% less than that exhibited by the $F_{420}$ cofactor. Also, FO and $F^+$ have been observed to possess a shorter nitrogen-10 side chain than that of the $F_{420}$ cofactor. Nonetheless, both FO and $F^+$ compounds are catalytically active in several $F_{420}$-dependent enzymatic reactions (*6, 7*). Additionally, the $F_{420}$ cofactor is photosensitive, rapid decomposition occurs when it is exposed to a strong white light, especially at basic pH (*11*).

The redox potential of the $F_{420}$ cofactor is between -340 to -350 mV (much lower than that of flavins) (*12*). This lower redox potential has been attributed with several major cellular implications. For example, instead of mediating transfer of electrons between $NAD^+$ and higher potential one- and two-electron acceptors such as flavins, the $F_{420}$ cofactor has the capacity to mediate the reduction of $NAD^+$ with electrons from hydrogen or via formate oxidation (*13*). In comparison to flavins, which have accessible semiquinone, the absence of the semiquinone or its formation has no deleterious effects on this role.

Nonetheless, the $F_{420}$ cofactor serves as a useful biochemical tool in the studies of flavoprotein catalysis. It is stable to air and boiling at near neutral pH, degraded by light at high pH and the side chain is cleaved in a low pH environment. It remains unknown whether, except in the photolyase, the $F_{420}$ cofactor is ever enzyme bound. It appears to behave as a soluble electron-transfer cofactor, but it has not been thoroughly investigated for its ability to covalently bind to proteins (*4*).

## 1.2 $F_{420}$ cofactor

### *1.2.1 Phylogenetic distribution of the $F_{420}$ cofactor*

The infrequent presence of the $F_{420}$ cofactor and its biosynthesis in certain prokaryotes has been utilized in comparative phylogenetic analysis and genomics-based investigation of organisms that employ this cofactor in their metabolic pathways. The $F_{420}$ cofactor has been previously discovered to be distributed sporadically amongst certain prokaryotic organisms, but observed universally in mycobacteria (*9, 10*).

Table 1.1 Distribution of 7,8-didemethyl-8-hydroxy-5-deazariboflavin (1).

| **Organism** | **Content expressed in pmol/mg (dry weight)** |
|---|---|
| *Methanogenic archaebacterial* | |
| *Methanobacterium thermoautotrophicum* | 3800 |
| *Methanospirillum hungatei* | 3700 |
| *Methanobacterium formicium* | 2400 |
| *Methanosarcina barkeri* | 190 |
| | |
| *Nonmethanogenic archaebacteria* | |
| *Halobacteria* | |
| *Strain GN-1* | >210 |
| *Halococcus salinarium* | >33 |
| | |
| *Acidophilic archaebacteria* | |
| *Thermoplasma strain 122-1B3* | >5 |
| *Sulfolobus solfataricus* | >1 |
| | |
| Eubacteria | |
| *Streptomyces spp.* | <20 |
| *Mycobacterium tuberculosis* | 13.5 |
| *Nocardia aurantia* | 8.5 |
| *Anacystus nidulans* | NR |

However, before this discovery, the $F_{420}$ cofactor was known to play an extensively significant role only in methanogenic bacteria and archaea. While this distribution is wide-ranging, the $F_{420}$ cofactor is abundant only in methanogenic bacteria where it is believed to function primarily as a redox carrier in energy metabolic pathways.

Although the cofactor is not unique to methanogens, it has become an important indicator for the identification of methanogens because of its high abundance in these cells and its intense fluorescence, especially when compared to other species in which this cofactor is found (Table 1.1) (1, 9, 14-15).

In fact, the $F_{420}$ cofactor was found in all methanogens examined at levels varying from 1.2 mg/kg of cell dry weight as in the case of Methanobervibacter ruminatium to approximately 65 mg/kg of cell dry weight as seen in *Methanobacterium thermoautotrophicum* (*16*). All methanogenic bacteria subsequently discovered have been observed to possess genes that encode for the synthesis, and ultimately the utilization of the $F_{420}$ cofactor in one way or another (*2, 16*).Because of its abundance, this deazaflavin cofactor apparently plays a critical role in the physiology of methanogens. Several authors have postulated that the $F_{420}$ cofactor is a functional substitute for ferredoxin (*16*). This idea has been supported by the absence of ferredoxin in several methanogens that have been studied. Also, an investigation of *Methanosarcina barkeri* found that it possessed an $F_{420}$ cofactor with polyglutamate derivatives at an order of magnitude much lower than in other methanogens, but contained ferredoxin (*17*). Most biochemical and energetic studies have been performed with a few methanogenic genera: *Methanosarcina, Methanobacterium and Methanococcus*. Since these genera are phylogenetically distantly related (Figure 1.4), the results obtained were hence considered to be representative for all methanogens (*4, 14).*

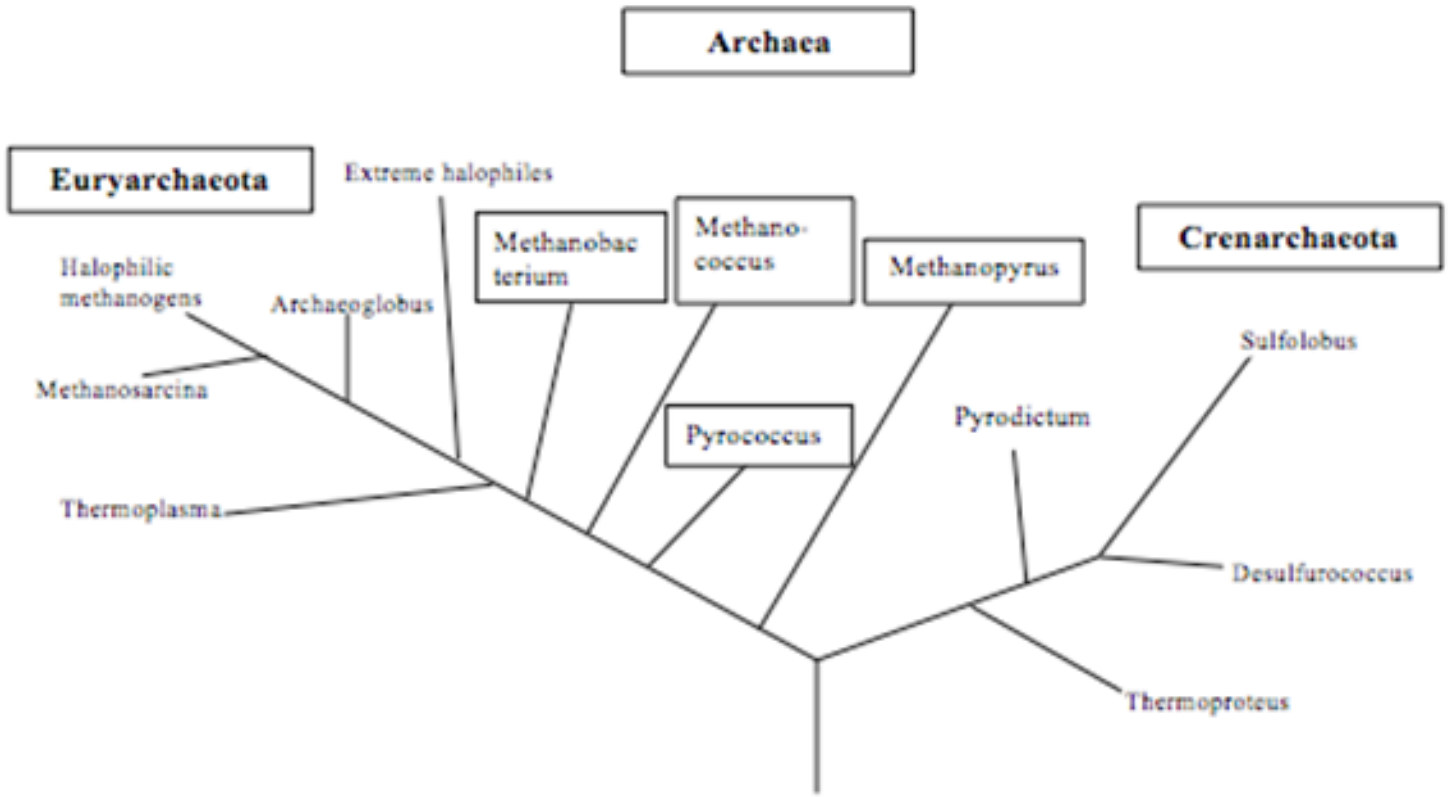


Figure 1.4 Phylogenetic tree of the archaea indicating the phylogenetic relationshipbetween various methanogenic genera, *Archaeoglobus* and *Pyrococcus (4).*

Also, the $F_{420}$ cofactor is found in Archaeoglobus fulgidus, where it participates in a series of two-electron transfer reactions. *A. fulgidus* is the first sulfur metabolizing organism to have its genome sequence determined. It possesses all of the enzymes and cofactor required for methanogenesis and produces a measurable amount of methane during sulfate reduction. Levels of cofactor $F_{420}$ found in *A. fulgidus* are similar to methanogens (*4, 18*).The discovery of this cofactor in other organisms suggests that the chemistry of the compound has been useful in other areas of cellular metabolism.

Although the structure of the $F_{420}$ was initially determined from a methanogenic bacterium (17), it was present in all Streptomyces species examined, as well as a pool of other related organisms such as *Nocardia* (*1-4*). It is also present in one genus of eukarya, and in some other archaea. Analysis of Streptomyces showed that some $F_{420}$ is excreted by the organism during growth; however, it is released in the form of FO. More so, compared to methanogens, the levels of cofactor $F_{420}$ in Streptomyces was found to be about 10-fold lower. The role of the cofactor $F_{420}$ in most Streptomyces is not known, but in specific Streptomyces, it is vital for the synthesis of chlortetracycline, oxytetracycline, and lincolnomycin, as well as DNA light repair (*1-3, 19*). Also, the biosynthesis of riboflavin in *Methanobacterium thermoautotrophicum* was studied by Eisenrich et al. (1991) and was found to be identical to that in eubacteria and fungi (*14, 20*). In the green algae Scenedesmus, the deazaflavin ring of the $F_{420}$ cofactor is required for DNA photolyase function (*1, 9, 19*).

In 2002, the $F_{420}$ cofactor became popular as investigation into its function and mechanism in mycobacteria amassed rapid attention. Purwartini and Daniels have shown that the $F_{420}$ cofactor is involved in the oxidation of glucose-6-phosphate dehydrogenase

by and $F_{420}$ dependent glucose-6-phosphate dehydrogenase (FGD1, Rv0407 – MTB gene). By doing so, the $F_{420}$ cofactor is biochemically modified to its reduced form (*9*). Phylogenetic investigation of $F_{420}$ biosynthesis, using M.bovis as a model, were also studied. Choi et al (2001, 2002) showed that fbiC gene participates in the earlier steps of $F_{420}$ biosynthesis between pyrimidinedione and hydroxyphenyl pyruvate to form FO by encoding for synthase. fbiAB genes are responsible for the biosynthesis of $F_{420}$ from the precursor, which involves the addition of a phospho-lactate group and condensation of glutamate on . *M. tuberculosis, M. bovis, M. avium, M. leprae, Nocardia farcinica, Streptomyces coelicolor, S. avermitilis, Thermobifida fusca and Rubrobacter xylanophilus* all have proteins with high homology for full length fbiC as shown in multiple amino acid sequence alignment of fbiC using representative organisms (Figure 1.5). In contrast, *Archaeoglobus fulgidus, Methanobacterium thermoautotrophicum, Methanococcus jannaschii, Halobacterium sp., Synechocystis sp., and Nostoc sp.* all have two polypeptides (located adjacent or non-adjacent) which encode for fbiC (*21-23*).

Selengut and Haft (2010) implemented partial phylogenetic profiling (PPP) to discover protein families that utilize the $F_{420}$ cofactor (*10*). This method was efficient in determining these protein families due to the possibility that the distribution of the $F_{420}$ cofactor may not span the entire profile. By applying hidden Markov models (HMMs) to a set of all 1,451 bacterial and archaeal genomes available from the National Center for Biotechnology Information (NCBI), several $F_{420}$-utilizing enzymes in mycobacteria based on the pattern of the $F_{420}$ cofactor biosynthesis trait were identified.

The most prominent family in the distribution was the Luciferase-like Monooxygenase (LLM) family. A few LLM family proteins have previously been discovered in archaea to be $F_{420}$ dependent; one has even been characterized (*10*).

Figure 1.5 Multiple sequence alignment of the FbiC protein in *Mycobacterium sp.*, *Norcadia sp.* and *Streptomyces sp.(23).*

The second most prominent family of enzymes from the partial phylogenetic profiling was the deazaflavin-dependent nitroreductase (DDN) families. This family was determined to be limited to only $F_{420}$-producing species.

Like the LLM family, the only characterized member of this family is $F_{420}$ dependent. The DDN family is known to include the deazaflavin-dependent nitroreductase Rv3547, this protein is active in the activation of the promising antimycobacterial prodrug, PA-824 (*9-10, 21, 23, 24*). The third family discovered from this profiling was the pyridoxamine 5'-phosphate oxidase (PPOX, or PNPOx). At the time of this discovery, there were no known $F_{420}$-dependent members of the PPOx family, however, several FMN-dependent enzymes were known. More recently, two families of $F_{420}$ dependent reductases (FDR-A and –B) which were previously uncharacterized have been identified. These enzymes were discovered to be distantly related to PPOXs (Figure 1.6).

However, the PPOx and FDR families are functionally dissimilar. Structurally and phylogenetically, the FDRs and PPOxs appear to have a common evolutionary origin, yet these enzyme families have evolved to utilize different cofactors.

Irrespective of their structural similarities, there are at least two major chemical differences between the two cofactors. As a result, catalyzed reaction by the two enzyme families is opposite (oxidation by the PNPOxs versus reduction by the FDRs).

Taylor et al. suggests that this difference in catalytic activity resulted in the evolutionary expansion of the FDRs in *M. smegmatis* (28 genes) compared with the single PPOx gene. Due to the high reducing power of $F_{420}$, these enzymes have hence

been allowed to catalyse the reduction of a wide variety of compounds, particularly xenobiotics (*10, 25*).

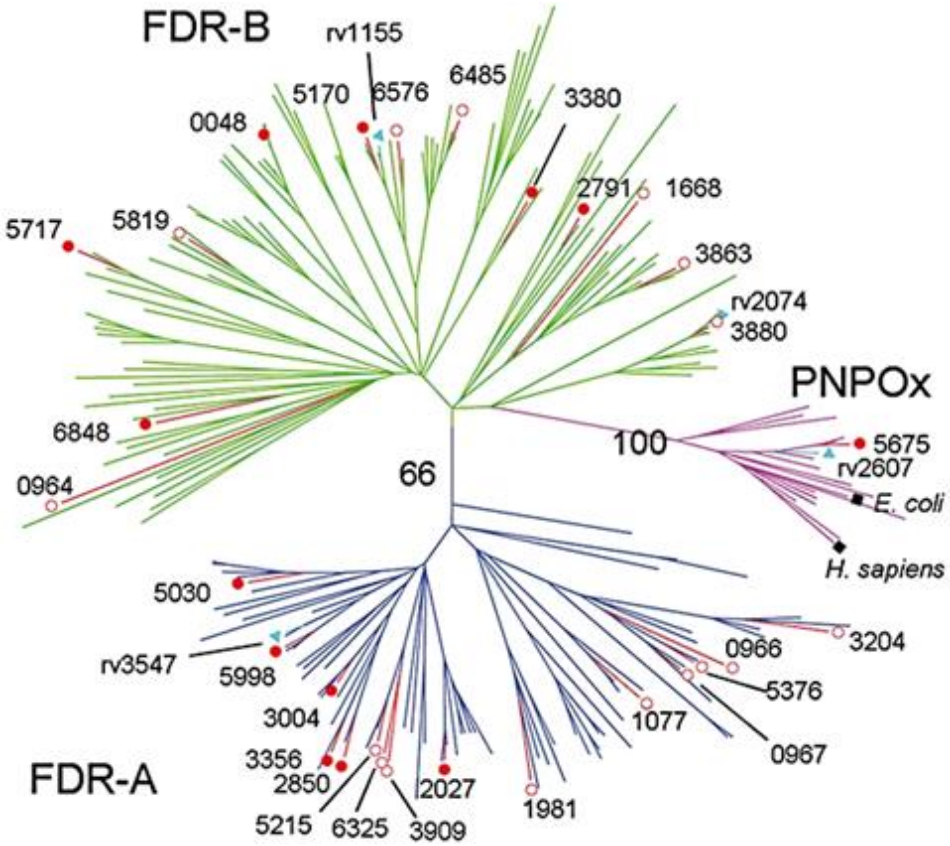


Figure 1.6 Phylogenetic relationship between the PPOx, FDR-A, FDR-B families (*26*).

These three (LLM, DDN and PPOx) families account for 32 genes in *Mycobacterium tuberculosis* (Figure 1.7) and 123 genes in *Mycobacterium smegmatis*. Partial phylogenetic profiling was also able to identify other members of LLM and PPOx as $F_{420}$-cofactor related, however, it was unable to determine how many and which ones specifically amongst the uncharacterized actually bind to the cofactor (*10*).

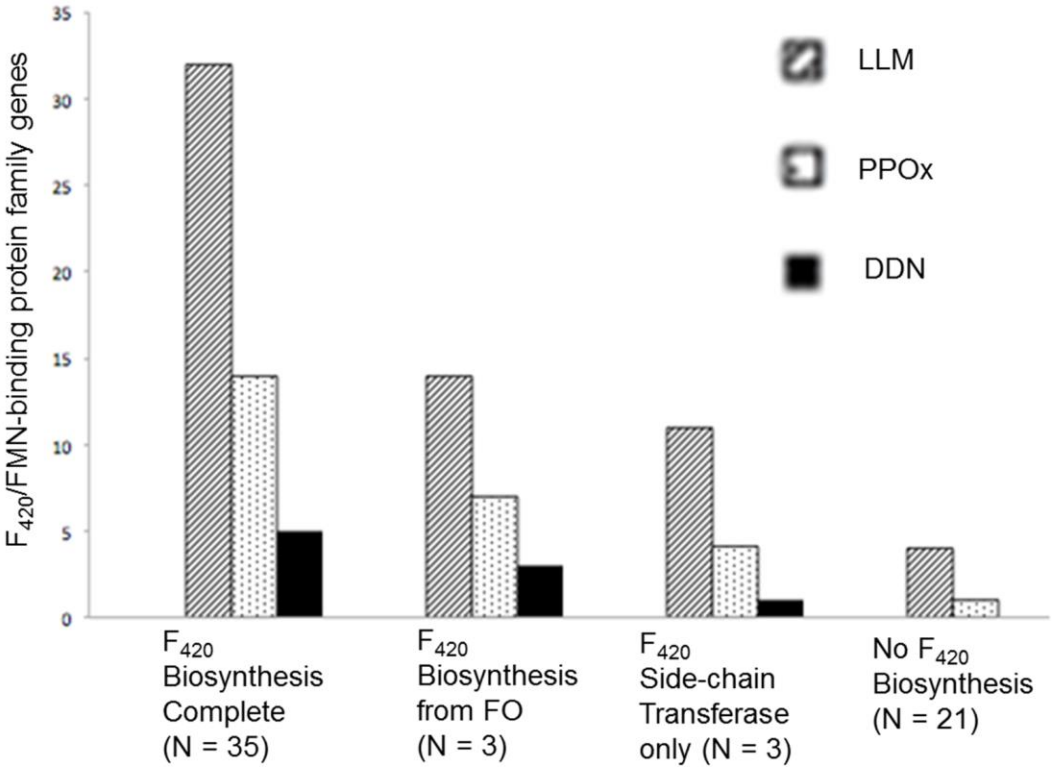


Figure 1.7 Average numbers of putative $F_{420}$/FMN-binding protein family genes in actinobacterial species (*9,10*).

*1.2.2 Biosynthesis of the $F_{420}$ cofactor*

By utilizing the cloning and over-expression of *Methanococcus jannaschii* genes along with purification of over-expressed enzymes, researchers such as Dr. Robert White among others have unraveled many of the steps in archaeal $F_{420}$ cofactor biosynthesis (*27*).

More recently, advances by Grochowski (2009) determined the genes and enzymes involved in the second step of archaeal $F_{420}$ cofactor biosynthesis, which was previously unknown (28). This reaction includes the conversion of 2-amino-5-formylamino-6-ribosylamino-4(3H)-pyrimidinone 5'-monophosphate (FAPy), structure (II),

to 2,5-diamino-6-ribosylamino-4(3H)-pyrimidinone 5'-phosphate (APy), structure (III) and formate by the enzyme formamide hydrolase, which was named ArfB.

The early steps in the biosynthesis of FO, which is the precursor to the $F_{420}$ cofactor, differ in eukaryotic and bacterial pathways. Although the biosynthesis of the $F_{420}$ cofactor has been largely resolved in the past 10 years, there still remain some discrepancies as to which enzymes are involved as well as their mechanisms.

However, it is widely accepted that the initial reaction for the biosynthesis of the $F_{420}$ cofactor is catalyzed by utilizing an archaeal enzyme known as Guanosine triphosphate (GTP) cyclohydrolase III (ArfA) (*29*). GTP cyclohydrolase III is encoded by the MJ0145 gene in M. jannaschii, which forms 2-amino-5-formylamino-6-ribosylamino-4(3H)- pyrimidinone 5' monophosphate (FAPy) (II) (Figure 1.8, reaction 1).

As mentioned earlier, ArfB or formamide hydrolase transcribed from the MJ0116 gene in M. jannaschii, functions in the hydrolysis reaction of FAPy (II) to form 2,5-diamino-6-ribosylamino-4(3H)-pyrimidinone 5'-phosphate (APy) (III). Additionally, APy (III) is then reduced to triaminopyrimidine phosphate (IV) by a specific NADP dependent reductase, known as 2,5-diamino-6-ribosylamino-4(3H)-pyrimidinone 5'–phosphate reductase or ArfC (Figure 1.8, Reaction 3) (*29*).

The 5-amino-6-ribitylamino-2,4(1H,3H)-pyrimidinedione (ARP), structure (VI), is the branch point for the production of final functional coenzymes, such as FMN or FAD, which are vital for life in biological systems.

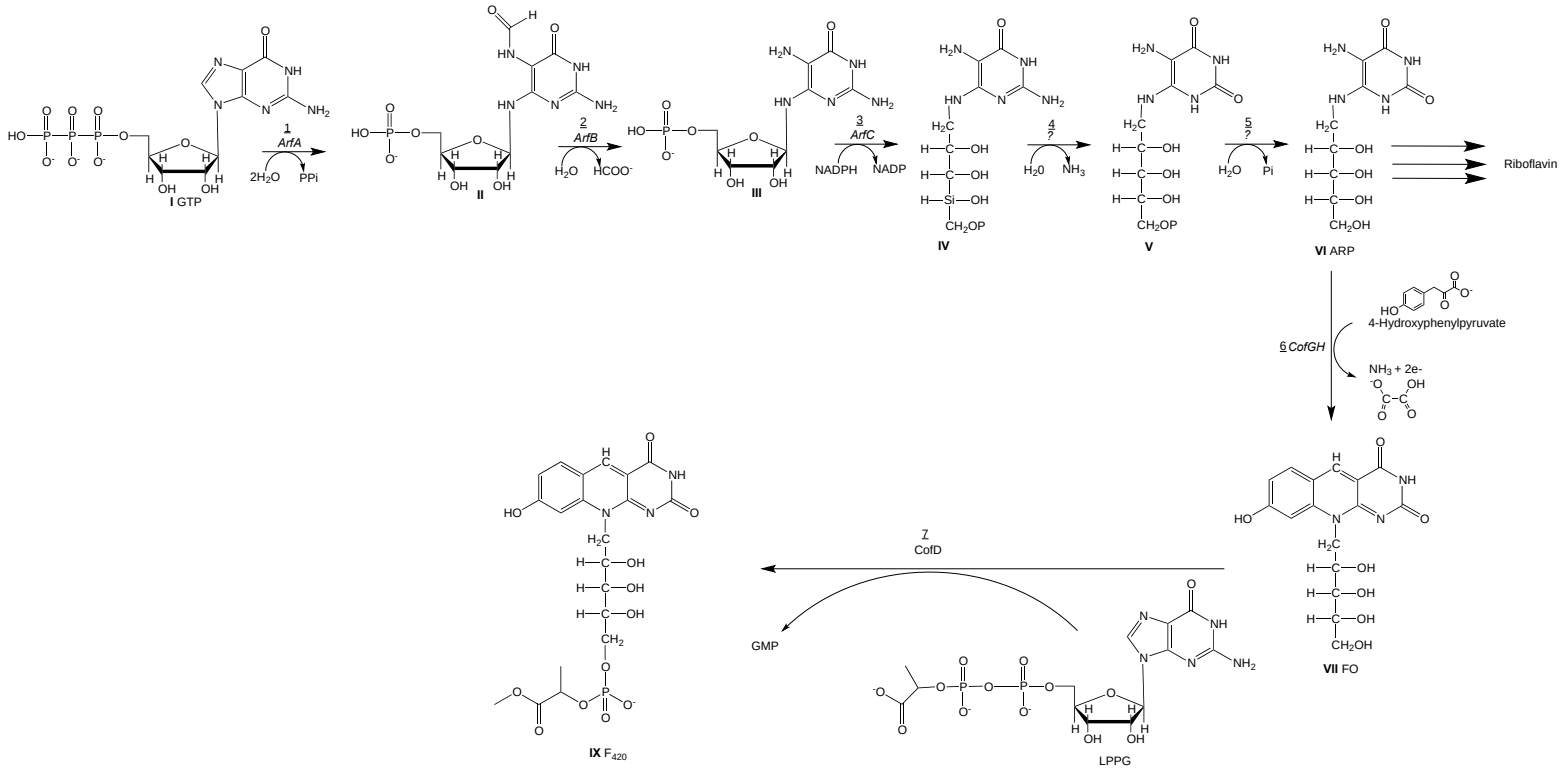


Figure 1.8 Overall biosynthesis of $F_{420}$-0 cofactor. (I) GTP, (II) 2-amino-5-formylamino-6-ribosylamino-4(3H)-pyrimidinone 5'-monophosphate or FAPy, (III) 2,5-diamino-6-ribosylamino-4(3H)-pyrimidinone 5'-phosphate or APy, (IV) triaminopyrimidine phosphate, (V) 2-amino-5-formylamino-6-ribosylamino-4(3H) pyrimidione 5'-monophosphate or ARP-P, (VI) 5-amino-6-ribitylamino-2,4(1H,3H)-pyrimidinedione or ARP, (VII) 7,8-didemethyl-8-hydroxy-5-deazariboflavin or FO, (VIII) lactyl-2-diphospho-5'-guanosine or LPPG, lastly (IX)$F_{420}$-0.

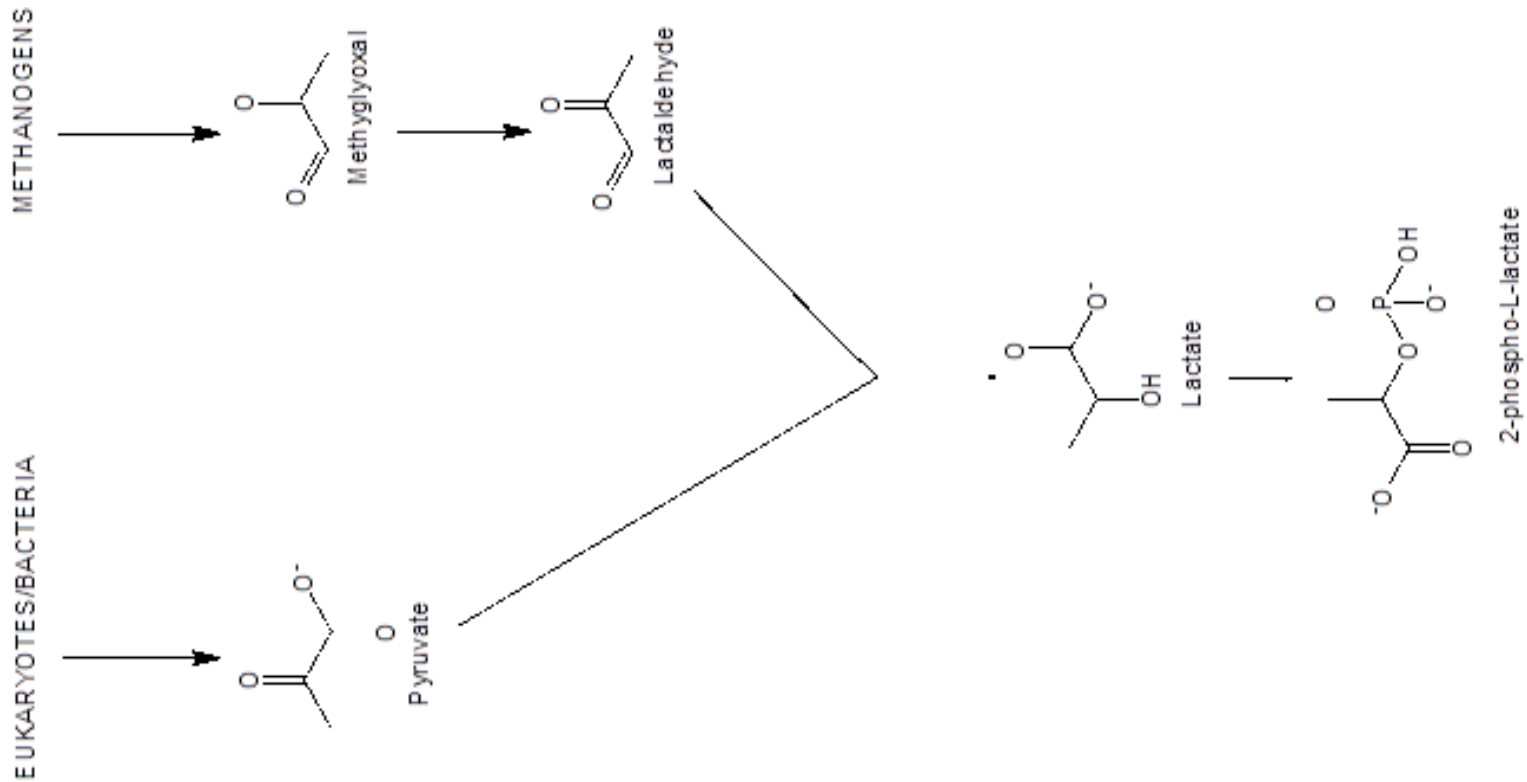


Figure 1.9 The two pathways involved in the production of 2-phospho-L-Lactate. Eukaryotes and Bacteria follow the 1A route with Pyruvate Dehydrogenase catalyzing the conversion of pyruvate to lactate. Alternatively, methanogens utilize route 1B converting methylglyoxal to lactate and finally forming 2-phospho-L-lactate. The enzymes responsible in the second pathway are not yet known (*27*).

The production of ARP (VI) includes the removal of a phosphate from 2-amino-5-formylamino-6-ribosylamino-4(3H) pyrimidione 5'-monophosphate (ARP-P) (V). The subsequent reaction to form ARP (VI) from ARP-P (V) requires an unknown enzyme (Figure 1.8) (*30*).

The unknown enzyme catalyzes the hydrolytic deamination of the opened ring structure of APy (III) at the C-2 position of the pyrimidine to produce ARP-P (V), (Figure 1.8, Reaction 4). Consequently, compound V is dephosphorylated by another unknown enzyme producing ARP (VI) (Figure 1.8, Reaction 5).

The biosynthesis of 7,8-didemethyl-8-hydroxy-5-deazariboflavin (FO) (VII), which serves as a precursor to the $F_{420}$ cofactor requires the fusion of ARP (VI) with 4-hydroxyphenylpyruvate by FO synthase (CofGH) (Reaction 6, Figure 1.8). FO synthase catalyzes the transfer of the hydroxybenzyl group from 4-hydroxyphenylpyruvate (a tyrosine precursor) to 5-amino-6-ribitylamino-2,4(1H,3H)-pyrimidinedione (an intermediate in flavin biosynthesis) to form FO (VII) *(2)*

A major component of the complete $F_{420}$ cofactor structure requires the formation of 2-phospho-L-lactate, which requires the phosphorylation of L-lactate (Figure 1.9). Two routes have been observed to form 2-phospho-L-lactate. The first pathway is catalyzed by lactate dehydrogenase, which converts lactate to pyruvate (Figure 1.9, Reaction 1A). Both bacteria and eukaryotes use this pathway. The second pathway converts methylglyoxal to 2-phospho-L-lactate in methanogens (Figure 1.9, Reaction 1B). However, the enzymes involved in these reactions are still unknown (*31).*

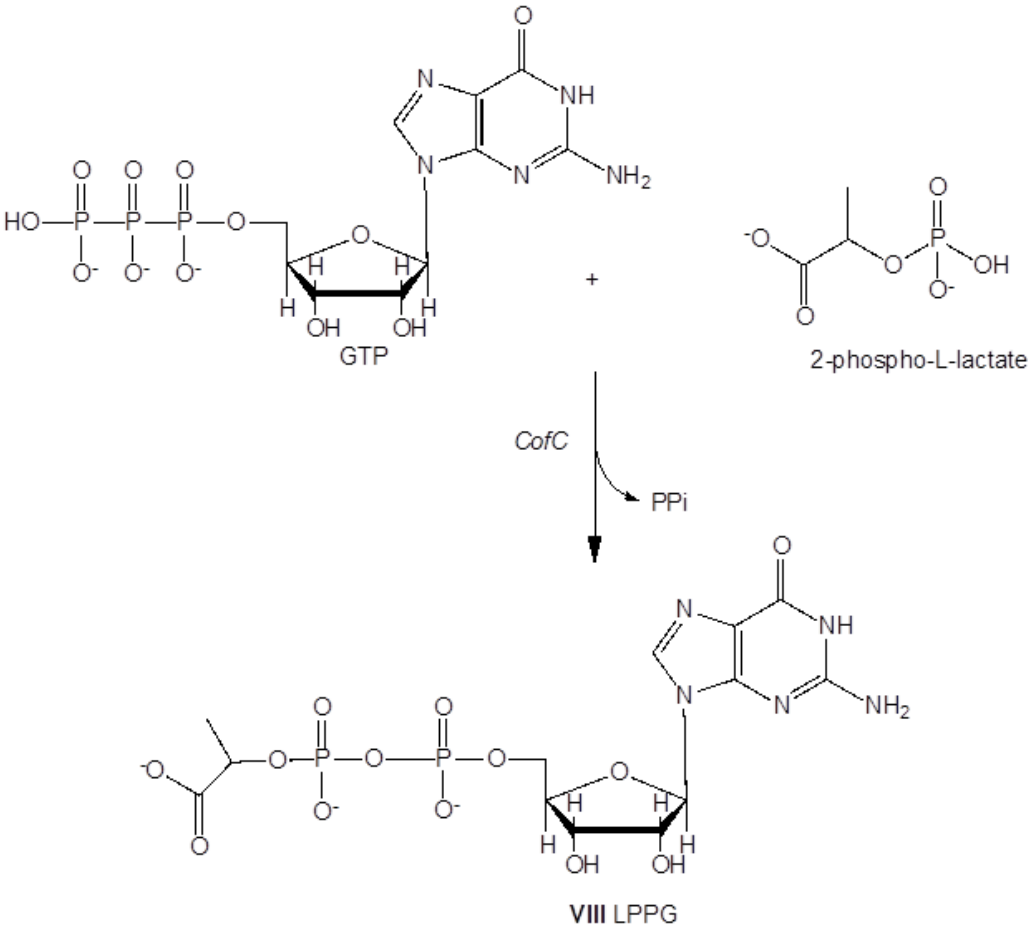


Figure 1.10 Structure VIII, lactyl-2-diphospho-5'-guanosine or LPPG is formed from the fusion of GTP with 2-phospho-L-lactate utilizing enzyme phospho-L-lactate guanylyltransferase (CofC) which releases a pyrophosphate

The addition of 2-phospho-L-lactate to the $F_{420}$ cofactor requires the formation of lactyl-2-diphospho-5'-guanosine (LPPG ) (VIII), which acts as a transfer molecule to FO (VII). LPPG (VIII) is formed by the addition of 2-phospho-L-lactate to GTP (Figure 1.10). The enzyme responsible for catalyzing this reaction was identified as phospho-L-lactate guanylyltransferase; named CofC from the MJ0887 gene, which has a similar structure to nucleotidyl transferases (*30*). Lastly, the 2-phospho-L-lactate component of LPPG (VIII) is transferred to FO (VII) by the enzyme 2-phospho-L-Lactate transferase (CofD, MJ1256) forming the $F_{420}$-0 cofactor (IX), which does not contain a glutamate tail (*31*).

Structural characteristic of the $F_{420}$ cofactor that unites different methanofurans include the formation of the phosphodiester bond along with the presence of a tail made of γ-linked glutamic acid residues. Formation of the phosphodiester bond in the $F_{420}$ cofactor is understood to follow the same reaction scheme as that of the DNA ligase reaction as well as the biosynthesis of coenzyme B12 and phospholipids (*32*). Phosphodiester bond linkages are present in other cofactors such as NAD, FAD, Coenzyme A, and molybdopterin. Consequently, the addition of a glutamate tail forms the complete $F_{420}$ cofactor structure.

The poly-glutamate of the $F_{420}$ cofactor is lengthened one glutamate at a time after the sequential addition of the first two glutamate residues (*21*). In M. jannaschii, the $F_{420}$ cofactor contains three glutamates. The first glutamate residue is attached to the amino group of the carboxylic acid in lactate, while the second residue is linked to the γ-carboxylic acid of the initial glutamate. The final glutamate is attached to the α-carboxylic acid of the second residue. The additions of the first two glutamate residues are added sequentially by the same enzyme CofE, a product of the MJ0768 gene. The terminal residue and any subsequent glutamate residues are added individually by (*2*) CofF; MJ1001 (*2*) It is suggested that the type of glutamyl linkage, α or γ, in the terminal glutamate residues varies in different archaeal species.

## 1.3 $F_{420}$ dependent enzymes

### *1.3.1 Enzymes: Relevance of cofactor through enzymes*

The $F_{420}$ cofactor was first found in methanogenic bacteria by Wolfe and his co-workers (*11*). It was initially thought to be a unique cofactor to methanogens (*17*), but was later discovered to be present in several other organisms including Streptomyces (3,

30, 33). Mycobacteria (*34-35*). Cyanobacteria (*35, 36-37*), green algae (*38*) and halobacteria (*7*). Methanogens play a critical role in carbon cycling because the methanogenic pathway reduces carbon dioxide to produce methane (Equation 1.3).

$$\mathrm{H_2 + CO_2 \rightarrow CH_4 + H_2O} \qquad \text{(Equation 1.3)}$$

As mentioned previously, several $F_{420}$ cofactor dependent enzymes have been identified and observed to require this cofactor for catalysis (Table 1.2) (*1*). The most important component of the $F_{420}$ cofactor needed for catalytic activity is the isoalloaxine chromophore (*39*) (Figures 1.1 & 1.2). The consequence of the carbon substitution at the 5-position is the conversion of the central ring from a pyrazine to a pyrimidine. This change significantly modifies the thermodynamics and kinetics of the redox processes involved with this cofactor. Because of this change, 5-deazaflavins, like the $F_{420}$ cofactor, are restricted to the two electron transfer cycles and only wield half the versatility of flavins. As a result, they are reduced more slowly when constituted with apoflavoenzymes, but reduced rapidly when the specific oxidant is a two-electron acceptor (*40*).

The alteration of other portions of the $F_{420}$ cofactor has also been observed to have a significant effect on $F_{420}$ flavoenzyme kinetics. For example, it has been shown that changing the length of the side chain at nitrogen 10 (as in FO and $F^+$) alters the rates of enzymatic reactions or the $K_m$ for the substrate, but the nature of catalysis remains the same (*39*). The $F_{420}$ reducing hydrogenase in cell extracts of *Methanobacterium* strain *M.o.H* has an apparent $K_m$ of 25 µM for the cofactor; however, it exhibits a higher $K_m$ of 100 µM for $F^+$ and FO compound (*17*). More so, for the $F_{420}$-specific secondary alcohol dehydrogenase, the hydroxyl at Carbon 8 (C-8) position influences the spectroscopic

properties of the $F_{420}$ cofactor and the pH activity profiles of the enzyme. Furthermore, methylation at C-8, C-7, or C-5 reduces the catalytic activity of the $F_{420}$ cofactor, and an alteration of the ring structure inactivates the cofactor (*39*).

Table 1.2 $F_{420}$-dependent enzymes (*1, 7*)

| **Enzymes** | **Organisms** | **Corresponding cofactor in non-$F_{420}$ reactions** |
|---|---|---|
| 1. $F_{420}$ reducing hydrogenase | Methanogenic bacteria | feredoxin |
| 2. NADP/$F_{420}$ oxidoreductase | Methanogenic bacteria | N/A |
| 3. Formate dehydrogenase | Methanogenic bacteria | N/A |
| 4. $F_{420}$-dependent alcohol dehydrogenase | Methanogenic bacteria | $NAD^+$ |
| 5. $F_{420}$-dependent pyruvate Dehydrogenase (pyruvate synthase) | Methanogenic bacteria | feredoxin |
| 6. α-ketoglutarate dehydrogenase (α-ketoglutarate synthase) | Methanogenic bacteria | feredoxin |
| 7.methylenetetrahydromethanopterin dehydrogenase | Methanogenic bacteria | $NAD(P)^+$ |
| 8.methylenetetrahydromethanopterin Reductase | Methanogenic bacteria | $NAD^+$ |
| 9. deoxyribomucleate cyclobutane dipyrimidine photolyase | Broad host range (*Mb. Thermoautotrophicum, Streptomyces sp., Anacystus nidulans)* | Methenyltetrahydrof-olate |
| 10. chlorotetracycline synthase | *Streptomyces aurofaciens* | N/A |

*1.3.2 $F_{420}$ reducing hydrogenase (FRH)*

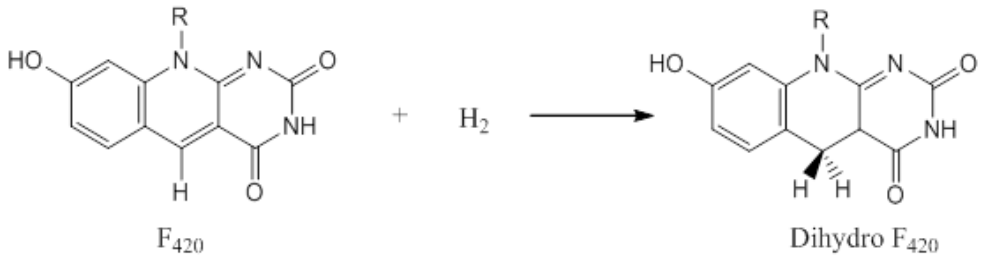


Figure 1.11 Reaction catalyzed by the $F_{420}$-reducing hydrogenase (*14*).

The $F_{420}$ reducing hydrogenase is the most thoroughly studied of all the $F_{420}$-dependent enzymes. This flavoprotein is primarily associated with the catalysis of the oxidation of molecular hydrogen by reducing the $F_{420}$-cofactor and the one-electron acceptor methylviologen (Figure 1.11, Equation 1.4, Equation 1.5):

$$\mathrm{H_2} \rightarrow 2\mathrm{H^+} + 2\mathrm{e^-} \qquad \text{(Equation 1.4)}$$

$$\mathrm{H_2} + \mathrm{F_{420}} \rightarrow \mathrm{F_{420}H_2} \qquad \text{(Equation 1.5)}$$

The $\Delta G°'$ associated with this reaction is approximately -11 kJ/mol. In most *Methanococcus* species and M. kandleri, there are two versions of the $F_{420}$-reducing hydrogenases, FrcABG (which contains a cysteine) and FruABG (contains a selenocysteine). The reduced $F_{420}$ cofactor, which is generated in the above reaction, is required for the reduction of $N^5$,$N^{10}$-methenyltetrahydromethanopterin to $N^5$,$N^{10}$-methylenetetrahydromethanopterin, which is subsequently reduced by the $F_{420}$ cofactor to $N^5$-methyltetrahydromethanopterin (*14*), these reactions will be subsequently discussed.

As previously inferred, the $F_{420}$ cofactor dependent reducing hydrogenase catalyzes both one- and two-electron transfer reactions. These reactions have been

previously investigated with the use of methyl viologen dyes (*7*) and the $F_{420}$ cofactor, respectively. Several $F_{420}$-reducing hydrogenases have been purified, however, only the enzymes from *Methanobacterium formicicum*, *Methanococcus voltae* and *Methanobacterium thermoautotrophicum* have been thoroughly characterized and have their structural and catalytic properties rigorously investigated.

As a matter of fact, not only has the FRH from the *M. thermoautotrophicum* strain ΔH has been purified, its encoding genes have also been previously determined. Like most hydrogenases, this $F_{420}$-reducing dehydrogenase has three subunits each weighing 47, 31, and 26 kDa respectively as well as three associated redox centers (nickel, iron-sulfur cluster, and FAD) (*41*).

Mechanistically, it has been postulated that the nickel site is the initial site for "hydride transfer in" from $H_2$. The iron-sulfur cluster was observed to behave as a one-electron conduit to the bound FAD. The reduced $FADH_2$ is therefore expected to be the site of the "hydride transfer out", from which the hydride is transported to the C-5 position of the $F_{420}$ cofactor. The FAD therefore serves as a one electron/two electron switch in the reduction of the $F_{420}$ cofactor (*42*).

The reduction of the $F_{420}$ cofactor provides a thermodynamic advantage to flavoproteins such as $F_{420}$-reducing hydrogenase (FRH) and formate dehydrogenase (FDH) in methanogenic bacteria (*42*)

By the oxidation of $H_2$ or $HCOO^-$ and passing on the two electron equivalents to generate $F_{420}H_2$, methanogenic bacteria easily generate a kinetically stable and low potential energy which is utilized in their cellular metabolism.

By donating electrons to the $F_{420}$ cofactor rather than $NADP^+$ directly, methanogens yield an additional 1.6 kcal/mol in the energy available for the oxidation of $H_2$ or $HCOO^-$. More so, $NAD^+$ reducing hydrogenase has been described to have a similar enzymatic mechanism (*13, 43*).

### *1.3.3 $F_{420}$-dependent $N^5$,$N^{10}$-methylenetetrahydromethanopterin dehydrogenase (MTD)*

The $F_{420}$ cofactor dependent $N^5$,$N^{10}$-methylenetetrahydromethanopterin dehydrogenase catalyzes the reversible dehydrogenation of $N^5$,$N^{10}$-methenyltetrahydromethanopterin with the reduced $F_{420}$ cofactor, $F_{420}H_2$, to $N^5$,$N^{10}$-methylenetetrahydromethanopterin (Figure 1.12, Equation 1.6). Like all other $F_{420}$ dependent enzymes, this reduction occurs via a hydride transfer and is more than likely stereospecific.

$$\mathrm{CH} \equiv \mathrm{H_4MPT} + \mathrm{F_{420}H_2} \leftrightarrow \mathrm{CH_2} = \mathrm{H_4MPT} + \mathrm{F_{420}} + \mathrm{H^+} \qquad \text{(Equation 1.6)}$$

The $\Delta G^{\circ\prime}$ associated with this reaction is about +5.5kJ/mol. The reaction catalyzed by this enzyme is coupled with the reaction catalyzed by the $F_{420}$ reducing hydrogenase to mediate the reduction of the substrate, $N^5$,$N^{10}$-methenyltetrahydromethanopterin, with $H_2$. MTD has been purified and characterized from *M. barkeri* and *A. fulgidus*.

### *1.3.4 $F_{420}$-dependent $N^5$,$N^{10}$-methylenetetrahydromethanopterin reductase (MER)*

The $F_{420}$-dependent methylene-$H_4$MPT reductase catalyzes the reversible reduction of methylene-$H_4$MPT ($N^5$,$N^{10}$-methylenetetrahydromethanopterin, $H_2C$=$H_4$MPT) to methyl-$H_4$MPT($N^5$-methyltetrahydromethanopterin, $CH_3$—$H_4$MPT) with the coupled

oxidation of the $F_{420}H_2$ deazaflavin cofactor to $F_{420}$ by $F_{420}$-reducing dehydrogenase during $CO_2$-methanogenesis (*4, 44*) (Equation 1.6). Like the preceding enzyme, MTD, this enzyme has been discovered in every $H_2/CO_2$ grown methanogen that has been investigated (Figure 1.13, Equation 1.7).

$$F_{420}H_2 + H_2C = H_4MPT + F_{420}H_2 \rightarrow CH_3 - H_4MPT + F_{420} \quad \text{(Equation 1.7)}$$

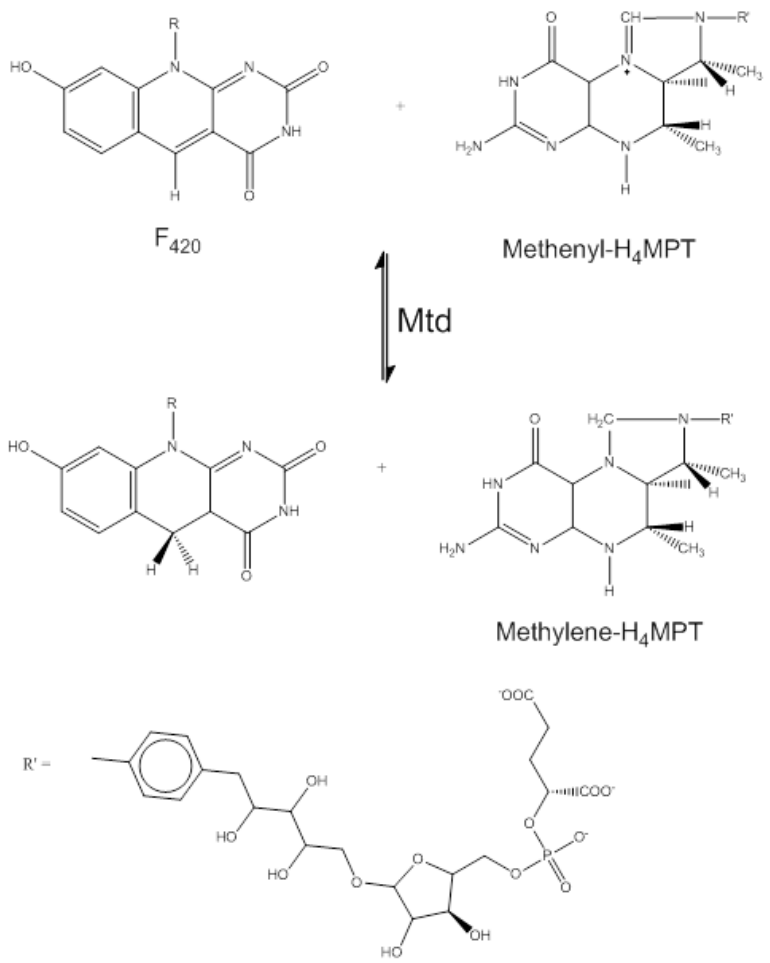


Figure 1.12 Reaction catalyzed by the $F_{420}$-dependent methylenetetrahydromethanopterin dehydrogenase (MTD).Together with the $F_{420}$-reducing hydrogenase, MTD catalyzes the reduction of methenyl-H4MPT to methylene-H4MPT.

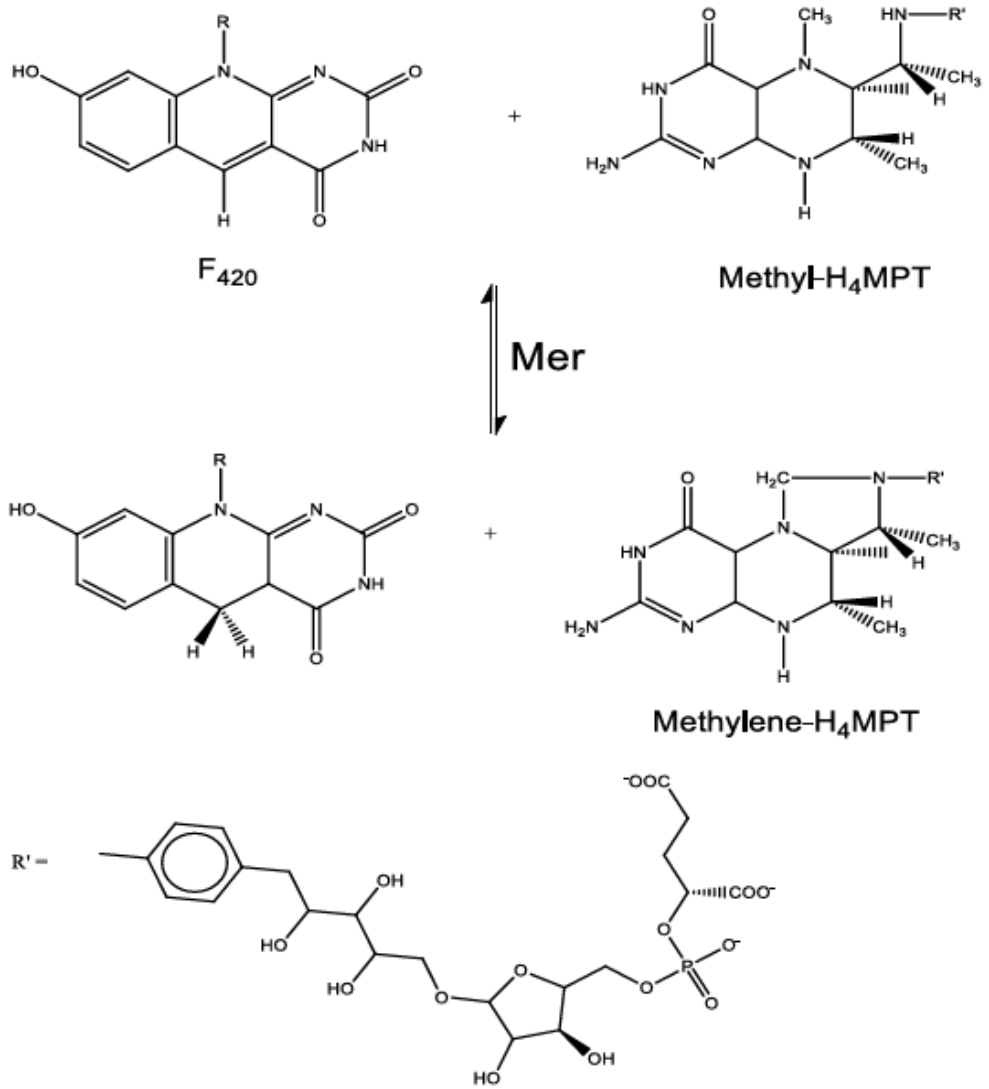


Figure 1.13 Reaction catalyzed by the $F_{420}$-dependent methylene tetrahydromethanopterin reductase (MER). Together with the $F_{420}$-reducing hydrogenase, MER catalyzes the reduction of methylene H4MPT with $H_2$ to N5-methyl-H4MPT (*45*).

The $\Delta G^{\circ\prime}$ associated with this reaction is -6.2kJ/mol, the $F_{420}$ cofactor serves as the electron carrier. Unlike several other $F_{420}$-dependent enzymes, MER does not contain any FAD or FMN, hence MER is not similar to $N^5$,$N^{10}$-methylenetetrahydrofolate reductase found in eubacteria and eukaryotes (*14*).This is particularly interesting because tetrahydromethanopterin is an analog of tetrahydrofolate. MER has been purified from *Methanobacterium thermoautotrophicum* strain Marburg and ΔH, *Methanosarcina barkeri, Methanopyrus kandleri* and *A. fulgidus*. More so, the crystal structure of MER has been resolved.

*1.3.5 Formate dehydrogenase (FDH)*

The $F_{420}$ cofactor is the physiological electron carrier for formate dehydrogenase found in methanogenic bacteria. $F_{420}$-dependent formate dehydrogenase activity was first described in *Methanogenium ruminantium* (*46*)., but it has been subsequently purified from *Methanogenium vannielii* (*46*) and *Methanobacterium formicicum* (*47-48*). This enzyme transfers electrons from formate to the $F_{420}$ cofactor (Figure 1.14). However, the reduction of the deazaflavin by formate dehydrogenase is dependent on the presence of an enzyme-bound FAD.

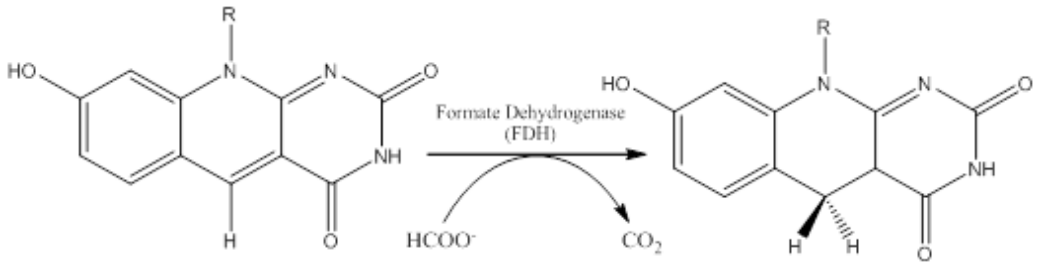


Figure 1.14 Reduction of the $F_{420}$ cofactor or FO catalyzed the FDH from *M. formicicum.*

Upon investigation of the mechanism of its catalyzed reaction, it is observed to have some similarities to $F_{420}$-reducing hydrogenase. Both enzymes have three subunits and three associated redox centers (iron-sulfur clusters, FAD, and either molybdenum or nickel).

However, unlike the $F_{420}$-dependent reducing hydrogenase, FDH utilizes molybdenum, not nickel. Like the $F_{420}$ reducing hydrogenase, it is probable that the molybdenum site of formate dehydrogenase is the initial site for "hydride transfer in" from formate. This reaction is comparable to the function of nickel in $F_{420}$ reducing hydrogenase in transferring hydride. Formate dehydrogenase can also utilize FAD, FMN and methyl viologen as alternate electron acceptors but not $NAD^+$ or $NADP^+$ (*46-49*).

*1.3.6 $F_{420}$-dependent alcohol dehydrogenase*

Although methanol can serve as a substrate for certain methanogens, virtually, most methanogens cannot grow on alcohol as the sole source of carbon and energy. However, it has been demonstrated that several methanogens use various primary and secondary aliphatic alcohols as well as cyclic alcohols, as the sole hydrogen donor for $CO_2$-based methanogenesis. These methanogens have been observed to express alcohol dehydrogenase (ADH) (*50-55*).As expected, ADH is vastly expressed when an alcohol is exclusively used as the source of reducing equivalents during growth, and also in some case if cells growing on formic acid (HCOOH) are starved of $H_2$ (*51*) (Equation 1.9).

$$\mathrm{F_{420}} + \mathrm{Isopropanol} \rightleftharpoons \mathrm{F_{420}H_2} + \mathrm{Acetone} \qquad \text{(Equation 1.9)}$$

Research with cell extracts of several methanogens shows that ADH activities from cells grown in alcohol and $CO_2$ use either $NADP^+$ or $F_{420}$ as electron carriers (*50-55*); activities that reduce $F_{420}$ with alcohol reduce $NADP^+$ very poorly if at all, and the reverse is also true. Alcohol dehydrogenase enzymes from methanogenic bacteria often show preference for either primary or secondary alcoholic groups (Figure 1.15) (*56*). For example, the ADH activity in the cell extract of *Methanobacterium palustre strain* F grown in 2-propanol plus $CO_2$ is an $NADP^+$-dependent enzyme, but it does not reduce the $F_{420}$ cofactor. Upon investigation, it was observed to oxidize 2-propanol, 2-butanol, 2,3-butanediol and cyclopentanol but not ethanol, 1-propanol, and 1-butanol (*50*). Interestingly, the $NADP^+$-dependent ADH activity from the cell extracts of ethanol and $CO_2$-grown *Methanogenium organophilum* which oxidized both 2-propanol and ethanol also converts acetaldehyde to acetate, and can thus catalyze dismutation of acetaldehyde to acetate and ethanol (*53*). An $F_{420}$-dependent alcohol dehydrogenase has been purified from $H_2$-starved *Methanogenium thermophilum* (*51*) and its crystal structure has been resolved. The $F_{420}$ cofactor was observed to co-purify with this enzyme, this is indicative of a tight binding between the cofactor and the enzyme. The enzyme does not use NAD(P), FMN or FAD, and oxidizes 1-propanol and ethanol 1000-times slower than it does 2-propanol.

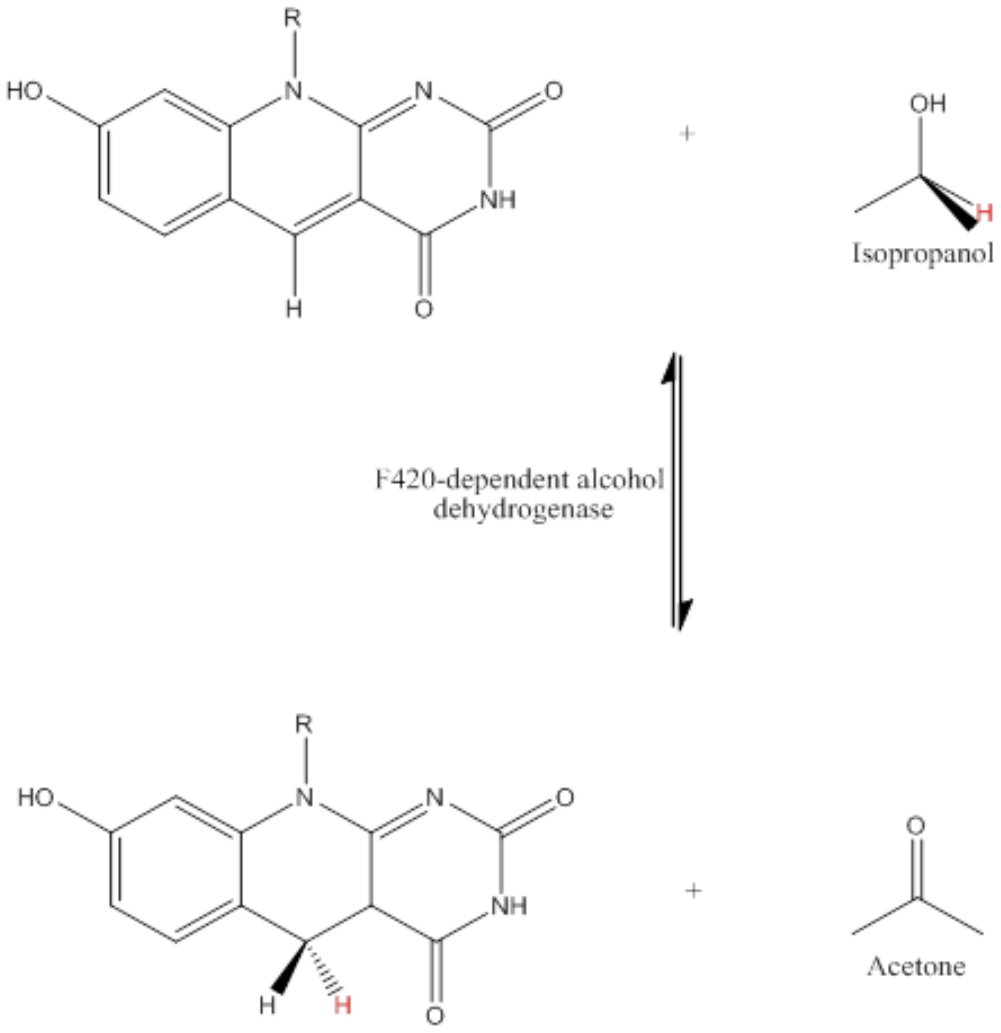


Figure 1.15 $F_{420}$-dependent alcohol dehydrogenase catalyzes the oxidation of isopropanol to acetone with the coupled reduction of $F_{420}$ to $F_{420}H_2$ (*56*).

*1.3.7 $F_{420}$-dependent glucose-6-phosphate dehydrogenase (FGD)*

Unlike most of the previously discussed enzymes, the $F_{420}$ dependent Glucose-6-Phosphate dehydrogenase enzyme (FGD) plays no role in methanogenensis or sulfite reduction. FGD has been discovered in *Mycobacteria and Norcadia* species, but, its crystal structure has only been solved from *Mycobacterium tuberculosis* (Mtb). FGD

catalyzes the conversion of glucose-6-phosphate (G6P) to 6-phosphogluconolactone (Equation 1.10). This reaction is a vital metabolic step in survival of the species in which this enzyme is present.

$$\mathrm{F_{420} + G6P} \rightleftharpoons \mathrm{F_{420}H_2 + 6-Phosphogluconolactone} \qquad \text{(Equation 1.10)}$$

Similar to every $F_{420}$ dependent enzyme, the reduction of the $F_{420}$ cofactor is achieved by the hydride transfer from the substrate molecule (G6P) to the $C_5$ position of the isoalloxazine chromophore. However, the role of the $F_{420}$ cofactor to Mtb in general has not been fully investigated or understood.

Nonetheless, the $F_{420}$ cofactor has been discovered to have some therapeutic significance. PA-824 is a nitroimidazopyran pro-drug which was synthesized in the efforts of combating the tuberculosis pandemic. Probing the mechanistic interactions between the pro-drug and the $F_{420}$ cofactor, it was discovered that the cofactor is indirectly responsible for the activation of the pro-drug. The studies showed that the reaction which FGD catalyzes produces reduced $F_{420}$ to an accessory protein which in turns activates PA-824 (*2, 9, 57-58*).

*1.3.8 $F_{420}$-dependent $NADP^+$ Oxidoreductase (Fno)*

The complete function of NADPH in methanogenesis and cellular carbon biosynthesis has not yet been fully investigated. However, NADPH may likely be the source of a significant portion of the reducing potential for the reduction of $CO_2$ into cellular carbon (*59*) and some other cellular intermediates (*1*). Fno ((E.C. 1.5.1.40) catalyzes the reversible reduction of $NADP^+$ to NADPH using the reduced $F_{420}$ cofactor (Figure 1.16, Equation 1.8):

$$\mathrm{NADPH} + \mathrm{H}^+ + \mathrm{F}_{420} \rightleftharpoons \mathrm{NADP}^+ + \mathrm{F}_{420}\mathrm{H}_2 \qquad \text{(Equation 1.8)}$$

The $\Delta G^{o\prime}$ associated with this reaction is -5.8 kJ/mol. The pH maxima for the forward and reverse reactions are 4.8 and 7.9 respectively. More so, at pH 7, the $k_{cat}$ of the reverse reaction is 24 times greater than that of the forward reaction, showing that the production of NADPH is the favored process (*14*).

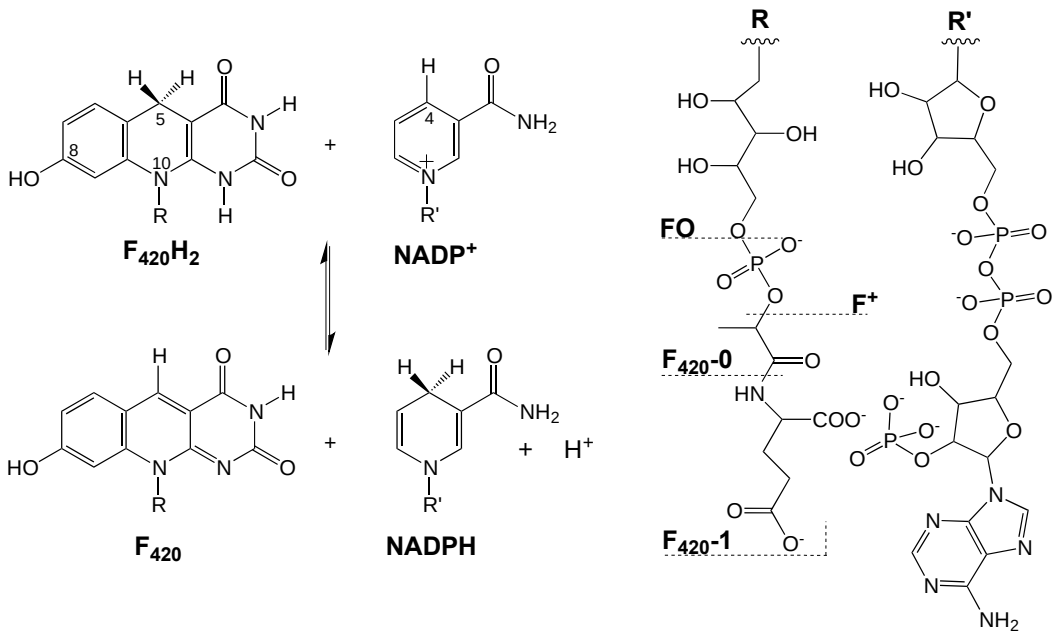


Figure 1.16 Structures of $F_{420}$ cofactor and $NADP^+$ and the reversible Fno reaction. This reaction is catalyzed by $F_{420}H_2$:$NADP^+$ oxidoreductase**.**The re-faces of the $F_{420}$ cofactors are shown. Fno catalyzes the reversible reduction of NADPH (*60-63*). Forms of reduced $F_{420}$ ($F_{420H2}$ or $F_{420,red}$) and oxidized $F_{420}$ ($F_{420}$ or $F_{420,\ ox}$) include the phosphorylated form ($F^+$), the $F_{420}$-0, the monoglutaminated form ($F_{420}$-1), or polyglutaminated forms with (n) number of glutamates ($F_{420}$-n).

In vivo, the Fno catalyzed reaction could be coupled with the reactions catalyzed by formate dehydrogenase or $F_{420}$ reducing hydrogenase (electrons from molecular hydrogen or formate can reduce $NADP^+$ to NADPH using $F_{420}$ as an intermediate electron carrier) (*49,64*). The Fno enzyme from *Archaeoglobus fulgidus* exhibits an apparent $K_m$ of

10 μM for the reduced $F_{420}$ cofactor and 40 μM for $NADP^+$ at 65° and pH 5.5. Further kinetic studies on the Fno enzyme showed that the N-10 side chain was not essential for catalytic activity, however, the introduction of a methyl group at the 8-position prevented reduction by the enzyme.

Fno exhibits high specificity for $NADP^+$ and $F_{420}$, hence, it cannot use $NAD^+$, FAD, or FMN (*7*). However, Fno can catalyze the reverse reaction. Fno has been purified from several methanogenic species, which include, *Methanogenium vannielli*, *Methanogenium thermoautotrophicum*, *Streptomyces griseus, Archaeoglobus fulgidus and Methanogenium organiphilum* (*64-65*).

Fno has also been purified and crystallized from *A. fulgidus*. *A. fulgidus* Fno belongs to the NAD(P)-binding Rossman-fold domain superfamily as defined by the Structural Classification of Proteins (SCOP) database (*66*). Each monomer contains an *N*-terminal Rossman-fold domain that binds $NADP^+$ and a *C*-terminal domain that binds $F_{420}$ (*60*). An initial kinetic characterization indicated that a ternary complex forms between Fno, $F_{420,red}$ and $NADP^+$ (*67*) and a similar complex is visualized by X-ray crystallography as a stable ligand structure in which the *Si*-face of $F_{420}$ neighbors the *Si*-face of $NADP^+$, suggesting that a hydride is transferred from the *proS* position at C5 of $F_{420,red}$ to the *proS* hydrogen position on C4 of the resulting NADPH product (*60*). Binding affinity experiments suggest that Fno follows an ordered mechanism in which an initial NADP(H) binding event helps to form the Fno binding pocket (*60*).

Previous experimental studies with Fno from *Methanobacterium thermoautotrophicum* have revealed that the reduction potential of FO ($F_{420}$ cofactor precursor) is between -340 to -350 mV, as determined by equilibration methods (*12*).

Jacobson and Walsh found that the ionization of the 8-OH substituent (p$K_a$ of 5.7) in the oxidized FO, stabilized by cross-conjugation throughout the tricyclic deazaflavin, suppresses FO reactivity toward redox chemistry. However, in the reduced FO ($FOH_2$), the phenolic group is electronically isolated to a single benzoic ring, resulting in a higher p$K_a$ of 9.7 (*12*). The present experiments were conducted with the redox active moiety of cofactor $F_{420}$, the deazaflavin, FO, as a facsimile for the $F_{420}$ cofactor, which is difficult to isolate in sufficient quantity for biophysical studies (*63*). Moreover, synthetic FO is fully catalytically active with Fno and has a higher purity than what can be produced from native sources. A detailed description of the improved synthesis of FO has been communicated elsewhere (*63*).

As shown in Figure 1.17, the crystal structure of Fno from *A. fulgidus* was solved in 2001 (60). The structure revealed that the enzyme is homodimeric with an α,β twisted fold. The structure was solved with one $F_{420}$ cofactor molecule and one $NADP^+$ molecule bound per monomer. These prosthetic groups are within 3.1 Å of one another, which is an acceptable donor-acceptor distance for a hydride transfer (*8, 12, 60, 68-71*). Previous steady state kinetic analysis confirmed the existence of the ternary complex (*59-63, 67, 72-74).*). Steady state data indicated a $K_m$ of 20 μM and 40 μM for $F_{420}H_2$ and $NADP^+$ respectively, at 65 °C and pH 5.5 (*60*). While the order of substrate addition could not be deduced from steady state kinetics, additional experiments were performed, which suggests that the presence of $NADP^+$ aids $F_{420}$ binding (*60*).

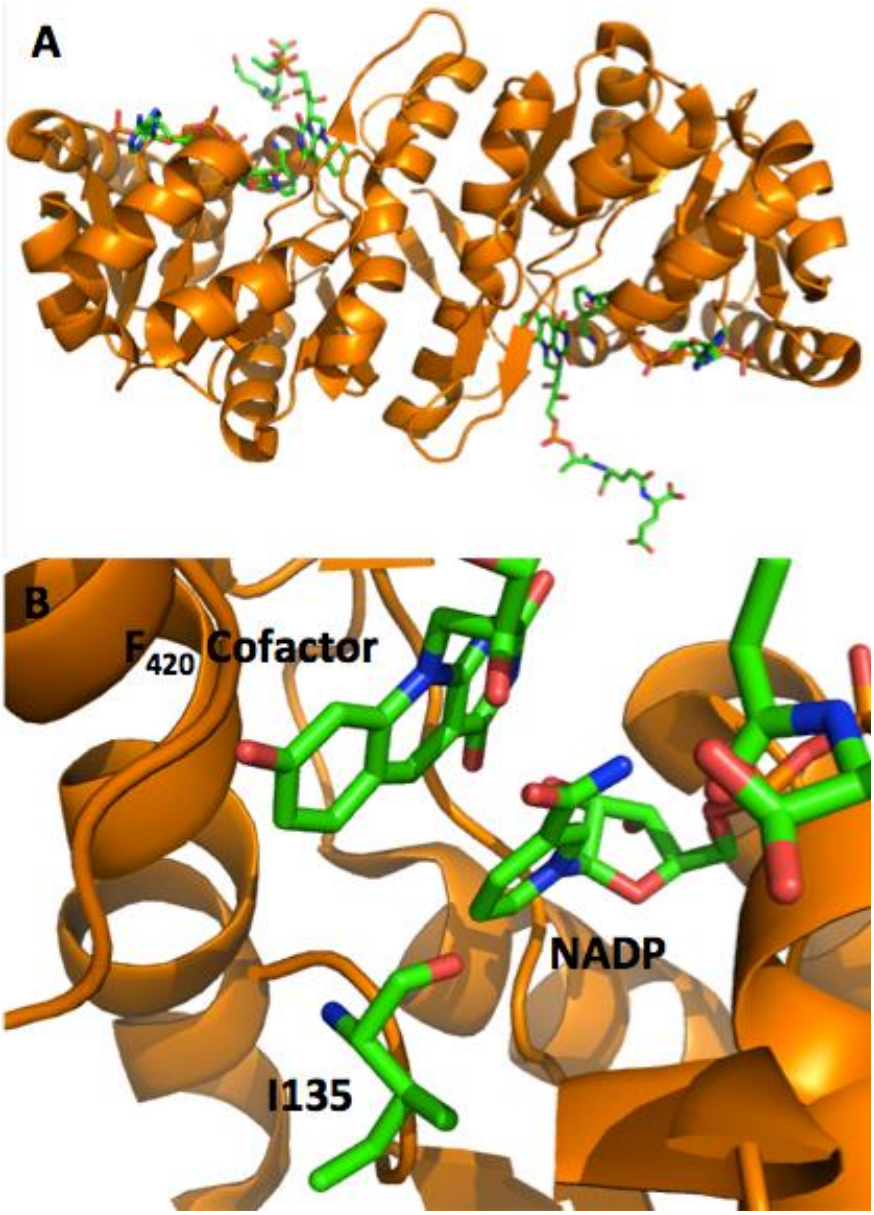


Figure 1.17 Crystal structure of Fno. A: homodimeric overall fold of Fno, in the presence of the $F_{420}$ cofactor. B: active site of Fno.

## 1.4 Conclusion

In this comprehensive review, we have attempted to explore the importance and application of the $F_{420}$ cofactor. The $F_{420}$ cofactor is versatile as it is found in a variety of

enzymes. It has proven to be essential to a plethora of organisms that utilize this deazaflavin for multiple metabolic processes.

As mentioned earlier, the interaction of the $F_{420}$ cofactor in the FGD enzyme has been associated with the promising anti-tuberculosis prodrug, PA-824. Although the kinetics of this enzyme has not been rigorously studied, the $F_{420}$ cofactor has been hypothesized to have a significant impact on hydride transfer mechanisms that activate the drug. More so, the reductive degradation of aflatoxin, a toxic compound, by a newly discovered family of $F_{420}$ dependent enzymes has been recently subjected to thorough biomedical investigation. Studies on curbing the poisonous effects from exposure to this compound have also surfaced in recent years (*26*).

Additionally, the $F_{420}$ cofactor has been found in several vital enzymes involved in methanogenesis. Methane is an important biofuel that has been used to replace several contemporary energy sources. Exploration into how to amplify methane production from methanogens is underway, in order to increase the use of more environment-friendly energy sources.

Minimal research has been undertaken with the $F_{420}$ cofactor and its corresponding dependent enzymes. Some of these enzymes could serve as useful models for understanding hydride transfer reactions and mechanisms. Furthermore, understanding the catalytic chemistry of these enzymes and their interaction with the cofactor could aid in treatment of various diseases as well as the implication of renewable energy.

Chapter 2

# CONVENIENT SYNTHESIS OF DEAZAFLAVIN COFACTOR FO AND ITS ACTIVITY IN $F_{420}$-DEPENDENT $NADP^+$ REDUCTASE

## 2.1 Introduction

Cofactor $F_{420}$ (Figure 1.1), a 7,8-didemethyl-8-hydroxy-5-deazariboflavin derivative, was discovered in the 1970's (*6, 1)* and is functionally similar to nicotinamide cofactors, NAD(P)+, while structurally reminiscent of the isoalloxazine tricyclic system found in flavin cofactors, FAD and FMN. Found primarily in prokaryotes (*1, 3-6, 14-15, 37*). $F_{420}$ and its precursor 5-deaza-7,8-didemethyl-8-hydroxy-5-deazariboflavin (FO, Figure 1.1), are unique organic redox-active coenzymes (E1/2 = -340 to -350 mV) capable of reducing both NAD(P) (ca. -320 mV) and FAD/FMN (ca. -210 mV) in a thermodynamically favourable manner(*12*). Due to the relatively acidic phenolic residue at C8, the activity of these species is pH dependent. In the neutral state, reduced FO ($FOH_2$) performs hydride transfer reactions with relatively enhanced reducing power as compared to NADH. Deprotonated FO was discovered to be a light-harvesting molecule for DNA photolyase in Drosophila (*75*). We set out to prepare FO synthetically as part of our studies of $F_{420}$-dependant $NADP^+$ oxidoreductase (Fno), an important enzyme for methanogens, which convert $CO_2$ to $CH_4$ (*76*).

The final intermediates of FO biosynthesis (*77* were recently identified from the proposed shikimate pathway (*78*); however, robust biological systems for the generation of FO and $F_{420}$ are underdeveloped. One report isolated FO efficiently from the lysate of fruit flies(75). Chemical approaches to deazariboflavins were defined prior to the discovery of $F_{420}$ (*79*). However, only one synthesis of each naturally occurring deazaflavin (FO, by Ashton et al. (*80-81*) and $F_{420}$ by Yoneda and coworkers) has been

communicated (Scheme 2.1). These chemical preparations contain significantly unstable intermediates, making these synthetic achievements quite impressive, but leave the field without convenient preparations of FO or $F_{420}$ (*79, 84*). This work displays a preparation of FO in the context of prior methods, which were instructional to the overall synthesis. Stability of intermediates was gained by a protection strategy for 3-aminophenol that added a single step to the synthesis and allowed for normal phase chromatography. The reported procedure does not require anaerobic ion exchange chromatography. In addition to the synthesis of FO, a deuterated C5D-FO precursor was prepared and wild-type $F_{420}$-dependent $NADP^+$ oxidoreductase (Fno) activity was studied directly with synthetic FO, displaying FO's function and kinetics in $F_{420}$-dependent enzymes.

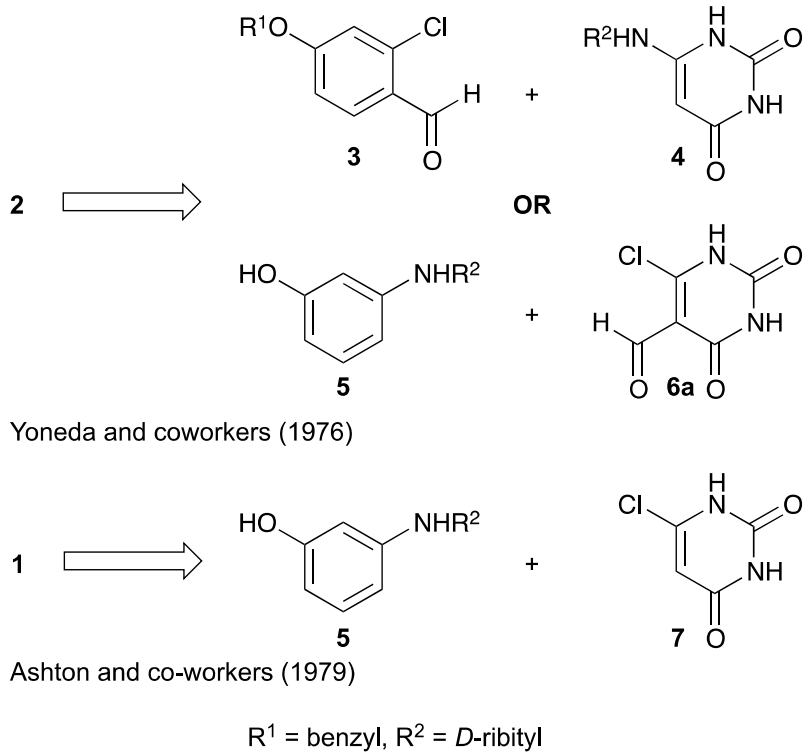


Scheme 2.1 Prior syntheses of compounds **(Fo, 1)** and **($F_{420}$, 2)**

The photo-degradation of riboflavin and related cofactors to lumichrome or lumiflavin is indicative of the intermediate instability challenging syntheses of FO (*85*). Purification challenges for natural and non-natural deazariboflavins and riboflavins pre-date FO and $F_{420}$ syntheses, but the electron-rich and acidic 8-hydroxyl substituent of FO and $F_{420}$ increase the challenges to these preparation (*86*). Prior work (Scheme 2.1) required anaerobic and dark conditions for early-stage intermediates, specifically involving compound 5, in addition to separations of polar, acidic intermediates by ion-exchange chromatography (*80-81, 87*).

## 2.2 An improved procedure to synthesize and purify FO cofactor

We wondered if a combination of prior approaches and steric Oprotection of 3-aminophenol could address the instability and related purification challenges of early-stage polar intermediates. Redox shuttle additives in batteries (e.g. di-tert-butyl-1,4-dimethoxybenzene) are kinetically stabilized by steric hinderance, rather than thermodynamically stabilized by alteration of their electron density (*88*). Satisfyingly, the introduction of a tertbutyldimethylsilyl (TBDMS) protecting group to 3-aminophenol addressed numerous issues, including: chemoselective O- vs. N-protection, enhanced redox stability, and simplified purification. Furthermore, the protecting group imparted no apparent effect on later transformations and, as described below, concomitant TBMDSO deprotection was achieved during the final HCl-generating transformation. Related silyl-protecting group, TBDPS-, was investigated, but negatively impacted the final condensation cyclization and required an additional reaction for O-deprotection under more harsh conditions. Conversely, benzyl-protection, used in Yoneda's synthesis of $F_{420}$, yielded only 75% of the O-protected product, with the N-protected byproduct. Unfortunately, the Obenzyl protected analogue of 11 did not cyclize with 6a, leading us to

believe that the facile deprotection of TBDMS- reveals the more electron-rich phenolate, aiding in final cyclization.

Selective O-protection of commercial 3-aminophenol 8 was achieved in 93% isolated yield (Scheme 2.2) (*89*). Protected 9 and Dribose were refluxed in dry methanol to yield N-ribosylaniline 10 as a white powder, which was purified by flash chromatography (silica). The resultant N-ribosyl compound was reduced to the corresponding N-ribitylaminophenol 11 (*87*), as an amorphous white solid after purification, again by normal phase flash chromatography. In our experience, handling the unprotected ribityl species 5 was a major source of anguish, especially during purification. This was presumably due to (photo) oxidation products, i.e. careful anaerobic and dark techniques did improve yields by limiting, but not eliminating, the formation of a brown multicomponent impurity, which could not be carried through subsequent reactions. Purified 11 was stable at room temperature for a few hours and could be stored at -20 ºC for over a month with no noticeable degradation.

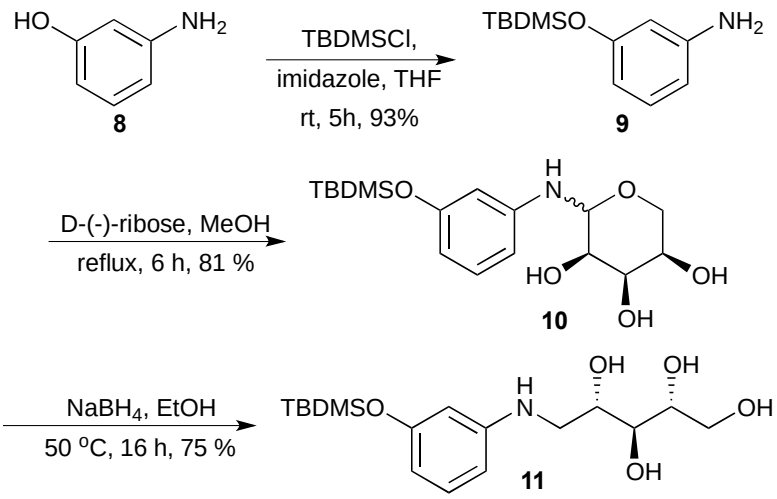


Scheme 2.2 Preparation of stable, hydrophobic fragment **11**

We found Yoneda's uracil derivative 6a (Scheme 2.3) to be the best condensation partner for fragment 11 (in comparison to 7 or 13). To prepare this species, barbituric acid 12 was converted to 2,4,6- trichloro-5-formyluracil 13a by Vilsmaier-Haack conditions (*90*). The resulting trichloroformyluracil 13a was converted to 6-chloro-5-formyluracil 6 in good yields by Yoneda's method (*91*). This two-step procedure also allowed access to deutoro-6 (6b) when DMF-d7 was substituted for DMF. The convergent synthesis of 1 was completed by condensation of 6a and 11 at 130 ºC in DMF for ca. 90 minutes. TBDMS-O was fully deprotected during the cyclization, which generates HCl.

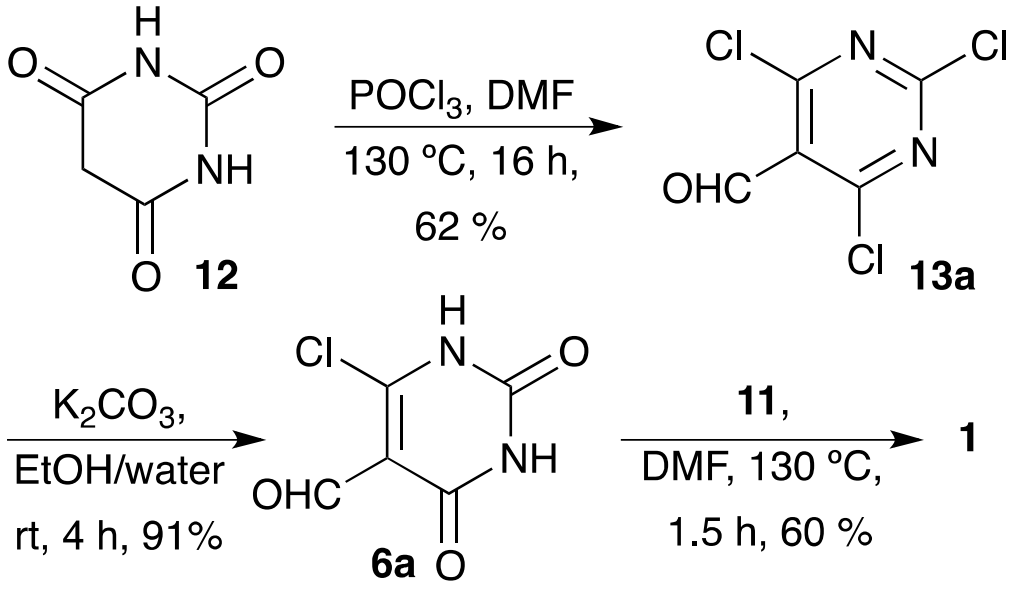


Scheme 2.3 Synthesis of Uracil **6a** and Condensation to FO, **1**.

With synthetic FO in hand, we investigated its reduction by NADPH in the place of $F_{420}$ in wild-type Fno (*wt*Fno, Figure 2.1) from *Archaeoglobus fulgidus*, which was expressed and purified in *C41(DE3) E. coli* cells. FO's activity in Fno (200 nM) was

examined aerobically by steady-state kinetics with a saturating concentration of NADPH, 600 μM, and varying concentrations of FO from 2 μM to 30 μM. Standard Michaelis-Menten kinetics were observed at pH 6.5 and 23 ºC (Figure 2.1). The $k_{cat}$ for *wt*Fno was 5.27 ± 0.14 s-1. The $K_m$ for oxidized FO under the same conditions was found to be 4.00 ± 0.39 μM. Previously reported $K_m$ values of *wt*Fno were: 20 μM at 65 ºC for the natural substrate, reduced $F_{420}H_2$; and 10 μM at 65 ºC for oxidized $F_{420}$ (*60, 72*). FO lacks the charged poly-glutamate tail of $F_{420}$ cofactor, eliminating putative points of contact between the coenzyme and Fno's binding site. However, oxidized FO still binds relatively tightly to Fno, in comparison to $F_{420}$. The detailed expression protocol and kinetic data for Fno using synthetic FO will be reported in due course.

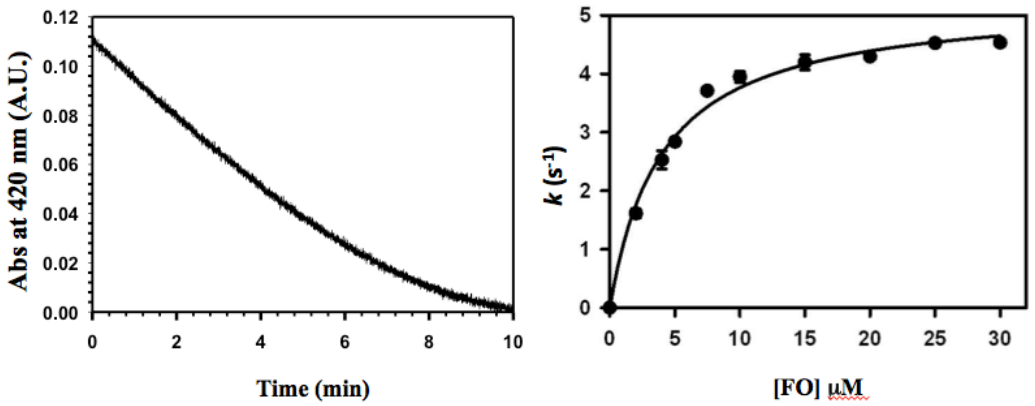


Figure 2.1 Steady-state kinetic monitoring of Fno catalysis. **Left:** A loss of $Abs_{420}$ nm is observed due to the Fno catalyzed reduction of $FO_{ox}$ in the presence of saturating NADPH and is linear for the initial ~7 min. **Right:** The steady state kinetics of reduction of FO by Fno is shown for varying FO concentrations. The reaction is carried out in 50 mM MES/NaOH (pH 6.5) buffer at 22 °C in a stopped-flow spectrophotometer. A constant NADPH concentration of 600 μM was used. . The data points were fit with the Henri-Michaelis-Menten equation ($k = \frac{k_{cat}\,[S]}{K_m+[S]}$). The plot of FO concentration vs rate constant during the steady state kinetics shows normal rectangular hyperbola with a $K_m$ and a $k_{cat}$ of 4.00 ± 0.39 μM and 5.27 ± 0.14 $sec^{-1}$ respectively (*63*).

## 2.3 Conclusion

$F_{420}$ cofactor is believed to be a major electron transfer entity in methanogenic bacteria, where it exists in high concentration and transfers electrons from hydrogen or formate to the consecutive intermediates of methane biosynthesis. $F_{420}$'s relatively low redo potential enables specific energy producing reactions such as the conversion of carbon dioxide to methane (*4*). A number of enzymes use $F_{420}$ as a cofactor in the metabolism of key pathogens, making the synthesis of $F_{420}$, FO, and deazaflavin mimics valuable. The synthetic route employed in this work involves significantly stable and hydrophobic intermediates, which are suitable for purification by conventional methods with aerobic bench-top procedures. Furthermore, the four step synthesis from 3-aminophenol is achieved in 33% compared to the 13% by previous methods. Intermediate 6a is generated in 56% yield. This preparation of FO should aid future biochemical researchers to investigate the different applications of $F_{420}$ in nature, especially in the metabolism of various pathogens. The biochemical utility of FO is shown in place of $F_{420}$ and the ability to use FO and related analogues may have great potential in biotechnology. On the next chapter, we are going to discuss the purification of Fno in detail.

Chapter 3

# OPTIMIZATION OF EXPRESSION AND PURIFICATION OF RECOMBINANT *ARCHEOGLOBUS FULGIDUS* $F_{420}H_2$: $NADP^+$ OXIDOREDUCTASE, AN $F_{420}$ COFACTOR DEPENDENT ENZYME

## 3.1 Introduction

A previous purification protocol (*60*) of Fno from *Archeoglobus fulgidus*, renders the protein with an unusually high absorbance at 260 nm, which is indicative of the presence of nucleic acids. The presence of nucleic acids is undesirable for a variety of reasons, particularly for accurate enzyme concentrations required for quantitative chemical kinetic rate studies. Here, we report an improved purification protocol of Fno from *A. fulgidus*, that is 99% free of nucleic acids. The Fno gene was optimized for heterologous expression in *Escherichia coli*. Modified growth conditions, and purification involving a key polyethyleneimine precipitation step resulted in a highly purified, homogeneous preparation of Fno that displayed high catalytic activity with FO. This improved method should is essential for advancing our kinetic analysis of the enzyme.

## 3.2 Materials and Methods

### *3.2.1 Reagents*

A truncated form of the $F_{420}$ cofactor, FO (Figure 1.16), was synthesized using a method we reported previously (Chapter 2) (*63*). NADPH was purchased from Akron Biotech. The parent pET24b plasmid was from Novagen. Luria Broth was purchased from US Biologicals. Isopropyl β-D-1 thiogalactopyranoside (IPTG) was from Gold Biotechnology and $KH_2PO_4$ buffer from BDH. $K_2HPO_4$ buffer was purchased from

Amresco and MES buffer from Acros Organics. The *E. coli C41(DE3)* strain was purchased from Lucigen. Kanamycin and $(NH_4)_2SO_4$ were from Fisher Scientific.

*3.2.2 Cloning, heterologous overexpression and harvesting*

The protein sequence of *A. fulgidus* Fno (NCBI Protein Database GI:74513452) was used to derive a DNA coding sequence with codons optimized for heterologous expression in *E. coli*, and this sequence was synthesized and incorporated into a shuttle vector by GenScript USA Inc. (*117*). The codon-optimized Fno coding sequence was subsequently cloned into the pET24b expression vector between restriction sites Nde I and BamHI to create the plasmid pET24b-Fno, and the entire coding region of the vector was verified by DNA sequencing at the GenScript facility to insure there were no unintended mutations. The pET24b-Fno plasmid was transformed into *C41(DE3) E. coli* cells using the procedures recommended by Lucigen and the resulting transformants selected for plasmid incorporation by growth at 37 °C on LB-agar plates supplemented with kanamycin (50 µg / mL). Single colonies were selected and used to inoculate overnight cultures from which glycerol-supplemented (20% v/v) stock solutions were prepared, flash frozen using liquid $N_2$, and stored at -80 °C.

Starting from a frozen cell stock of *E. coli C41(DE3)* (pET24b-Fno), starter cultures were grown overnight in LB medium supplemented with kanamycin (50 µg / mL), and these were used to inoculate 2 × 5 L cultures of LB medium supplemented with kanamycin (50 µg / mL), each grown in a 10 L flask kept at 37 °C in a water bath and constantly aerated using sterile filtered house air. Once the $OD_{600}$ of the cultures reached 0.6 absorbance units, expression of Fno was induced by addition of IPTG (1 mM), followed by continued incubation and aeration overnight (16 h) at 37 °C. Cells were

harvested by centrifugation at 6,750 *g*, and the resulting supernatant discarded. A typical batch yields approximately 9 g cell paste / L culture.

*3.2.3 Cell lysis*

Unless otherwise noted, the subsequent Fno purification procedures were completed at 4 °C. Starting with approximately 30 g cell paste, cells were re-suspended in $KH_2PO_4$ buffer (1.5 M) at pH 8.0 and lysed by sonication over ice using a Branson Digital Sonifier S-250D with a ½'' Dia. Tapped Bio Horn.mdd

*3.2.4 Heat precipitation and ammonium sulfate fractionation*

After lysis, the cell debris was pelleted by centrifugation (16,000 × *g*) and discarded. Unlike the heterologous host strain *E. coli*, the parent organism *A. fulgidus* is hyperthermophilic, and this property of Fno is exploited for this initial purification step. The remaining supernatant was heated in a water bath at 90 °C for 30 min to denature and precipitate most non-thermophilic proteins, followed by cooling to room temperature and centrifugation (16,000 × *g*) for 30 min at 4 °C to pellet and discard any precipitated proteins. The proteins remaining in the supernatant were then fractionated by slow addition of $(NH_4)_2SO_4$, with stirring, to 40% saturation, followed by centrifugation (16,000 × *g*) for 30 min to pellet and discard any precipitated proteins. Additional $(NH_4)_2SO_4$ was slowly added, with stirring, to the remaining supernatant to reach 70% saturation, followed by centrifugation (16,000 × *g*) for 30 min to pellet and save the precipitated proteins. The remaining supernatant was discarded.

*3.2.5 Polyethyleneimine precipitation and dialysis*

The protein pellet precipitated by $(NH_4)_2SO_4$ (40 – 70% saturation) was resuspended in Tris-HCl (50 mM) at pH 7.5, and treated with polyethyleneimine (0.05 % w/v) for 15 min to precipitate any remaining nucleic acids. The solution was centrifuged (16,000 × *g*) for 10 min and the resulting pellet discarded. The remaining supernatant was placed in dialysis tubing with a 14 kDa molecular-weight cutoff (MWCO) and dialyzed overnight (16 h) against 1 × 2 L buffer (50 mM Tris-HCl, pH 7.5). The dialysate was centrifuged at 16,000 × *g* for 20 min to precipitate and then discard any precipitated proteins.

*3.2.6 Ion exchange and size exclusion chromatography*

Unless otherwise noted, all the column chromatography steps were carried out at 4 $^{o}$C using a flow rate of 1 mL / min with a Bio-Rad BioLogic LP chromatography system. The supernatant prepared in the prior step was loaded onto an anion exchange column (D3764, DEAE-Cellulose from Sigma, 2.5 × 6 cm), and then washed with Tris-HCl (50 mM) at pH 7.5. A linear gradient of increasing NaCl (0-250 mM) over 300 mL was used to selectively elute bound proteins, with fractions containing Fno activity eluting near 200 mM NaCl. Fractions with Fno activity were pooled (typically 60 mL total) and concentrated using a centrifugal filtration device with a 30 kDa MWCO (Millipore) to a final volume of approximately 1 mL.

The resulting sample was loaded onto a size exclusion column (Sephacryl S-200 HR from GE Healthcare, 1 × 40 cm), pre-equilibrated with MES buffer (50 mM) at pH 6.5. The same buffer was used to chromatograph the remaining proteins, with purified Fno eluting after about 0.5 column volumes. Fractions containing Fno activity were pooled

(typically 10-15 mL total) and concentrated using a centrifugal filtration device with a 30 kDa MWCO (Millipore), to result in the final purified Fno protein solution. For long term storage, the purified Fno solution in MES (50 mM) pH 6.5 was made to 20 % glycerol (v/v), well mixed, flash frozen in aliquots using liquid $N_2$, and stored at -80 °C. Prior to subsequent use, each aliquot is slowly thawed on ice.

*3.2.7 Quantification of protein*

Protein solutions were quantified by measuring absorbance at 595 nm through the method of Bradford (*92*) using bovine serum albumin as a standard.

*3.2.8 Estimation of molecular weight and purity*

The proteins contained in aliquots of various purification steps, including the final purified protein and molecular weight markers, were resolved using a gradient sodium dodecyl sulphate - polyacrylamide gel electrophoresis gel (SDS-PAGE, precast gel, 4 - 20% Tris-HCl; BioRad) using a Tris-glycine buffer (*93*) to determine the purity and apparent molecular weight of Fno and used to compare with previous reports (*94*). Gels were run using a potential of 150 V, and then stained for protein using EZ-Run Staining Solution (Fisher) followed by washing with deionized water according to the manufacture's procedure (*95*).

*3.2.9 Fno kinetic assay*

To monitor steady-state kinetics of Fno-catalyzed reduction of $FO_{ox}$ and oxidation of NADPH, we used a previously described method (*60*). The reaction assay containing 50 mM MES/NaOH pH 5.5, 5 uM FO, 2 M $(NH_4)_2SO_4$, and 5 µL of *wt*Fno solution was

incubated in 65$^0$C for 5 minutes. The reaction was then initiated using 600 µM NADPH. FO reduction was monitored using a Cary 100 Bio spectrophotometer at 420 nm. The reaction assays displayed in Table 3.1 were conducted at room temperature (23 $^o$C) under the following conditions: 50 mM MES/NaOH pH 6.5, 5 uM FO, 600 µM NADPH, and 5 µL of *wt*Fno solution. The reduction of FO was measured at 420 nm by the same spectrophotometer.

Table 3.1 Purification table for recombinant *A. fulgidus* Fno

| Purification Step | Total Protein (mg)[a] | Total Activity (µmol/s)[b] | Specific Activity (U/mg) | Abs[d] 260 nm / 280 nm | Yield (%)[e] | Fold [f] Purification |
|---|---|---|---|---|---|---|
| Cleared Lysate | 1950 ± 7 | 93.3 ± 0.9 | 2.9 ± 0.9 | ~1.8? | 100 | 1 |
| Heat Treatment | 58.9 ± 0.9 | 51.7 ± 0.9 | 52.7 ± 0.9 | 2.0 ± 0.3 | 55 | 18 |
| $(NH_4)_2SO_4$ ppt[c] | 48.7 ± 0.1 | 42.1 ± 0.1 | 51.9 ± 0.1 | 2.00 ± 0.03 | 45 | 18 |
| Polyethyl-eneimine ppt[c] | 13.5 ± 0.3 | 18.4 ± 0.3 | 81.3 ± 0.7 | 1.03 ± 0.07 | 20 | 28 |
| Ion Exchange | 10.4 ± 0.1 | 13.5 ± 0.8 | 77.9 ± 0.8 | 0.59 ± 0.04 | 14 | 27 |
| Size Exclusion | 7.6 ± 0.1 | 9.1 ± 0.1 | 71.8 ± 0.1 | ~0.5±0.01 | 10 | 25 |

[a] Apparent protein amounts (shown as mg) were determined using diluted samples and Bradford reagent.

[b] Kinetic assays were performed at 23 °C.

[c] Precipitation

[d] Absorbance

[e] Yield (%) = (Total Activity $_{\text{each step}}$ / Total Activity $_{\text{Cleared Lysate}}$) × 100

[f] Specific Activity $_{\text{each step}}$ / Specific Activity $_{\text{Cleared Lysate}}$

## 3.3 Results and Discussion

### *3.3.1 Purification of Fno using previous methods*

Starting with the codon optimized pET24b-Fno expression vector described above, we followed a previously published protocol for heterologous expression of *A. fulgidus* Fno in *E. coli BL21(DE3)* in a mineral salts medium and the subsequent purification of Fno (*60*). No yields or absorbance spectra were previously reported for purification of recombinant *A. fulgidus* Fno. In our hands, this protocol also consistently provided homogenous protein that displayed only one significant band in Coomassie-stained SDS-PAGE gels (data not shown). However, when further characterizing Fno in preparation for detailed kinetic studies, we consistently found a significant absorbance peak at 260 nm (Figure 3.1) rather than a dominant peak at 280 nm as was expected for the apoprotein. We suspected that the peak at 260 nm might indicate a significant concentration of nucleic acids remaining in the final purified protein mixture. Contaminating nucleic acids are a potential concern for kinetic studies where accurate enzyme concentration determinations are required. For example, nucleic acids can significantly impact the accuracy of the Bradford protein assay (*96*). A broad DNA absorbance peak with a typical $Abs_{260/280}$ nm ratio of approximately 1.8 could also impact the use of $Abs_{280}$ nm readings to quantify Fno concentrations using its extinction coefficient ($\varepsilon_{280}$ = 13,980 $M^{-1}cm^{-1}$) as calculated by ProtParam (*97*). Additionally, because the $F_{420}$ cofactor carries a polyglutamate substitution, there is also the potential that anionic DNA could compete for binding to the accessible polyglutamate binding region of Fno and affect $K_d$ or $K_m$ measurements. To avoid these complications, we developed an optimized method for the heterologous expression and purification of recombinant *A.*

*fulgidus* Fno that eliminates this contamination.

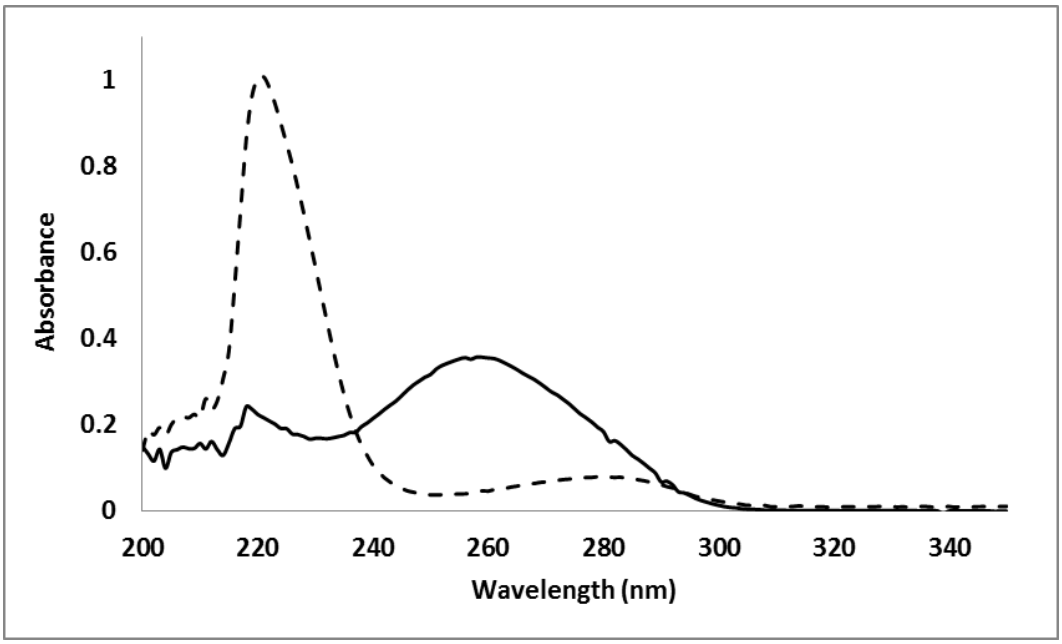


Figure 3.1 Absorbance spectra of purified Fno from different protocols. Fno prepared using a previous method (*60*) shows a dominant peak at 260 nm (solid line). Fno purified using the method described herein shows a spectrum more consistent with that expected for protein, with the aromatic amino acids contributing to the 280 nm peak and the peptide bonds to the 220 nm peak (dashed line).

*3.3.2 Heterologous overexpression of Fno*

Previous methods used a coding sequence for Fno derived from *A. fulgidus* and expressed the protein in an *E. coli BL21(DE3)* strain grown using a minimal medium (*60*). We first sought to increase expression levels by using a synthetic gene encoding Fno with codons optimized for expression in *E. coli*. We found that higher concentrations of Fno were produced when we substituted *E. coli C41(DE3)* cells as the expression host and used a rich LB growth medium (comparison data not shown).

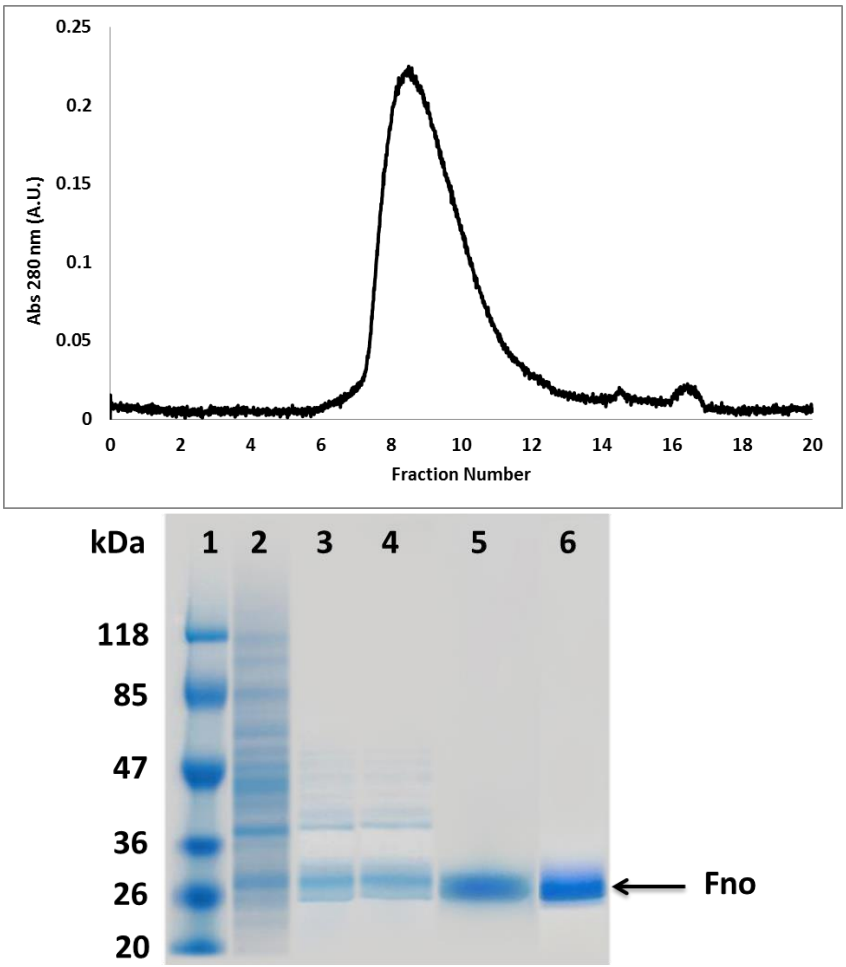


Figure 3.2 Purification of Fno.**Upper:** Chromatogram of the size exclusion column. A small contaminant is observed to elute after the main peak (Fno). **Lower**: SDS-PAGE gel of various purification steps. Lane 1: Molecular weight markers; Lane 2: Cleared Lysate; Lane 3: Supernatant after heat precipitation; Lane 4: Resuspended $(NH_4)_2SO_4$ precipitate (40 - 70 %); Lane 5: Pooled and concentrated Fno fractions after anion exchange chromatography; Lane 6: Pooled and concentrated fractions of Fno after size exclusion chromatography.

The C41 strain contains mutations that enhance expression of some toxic proteins (*98*). Heterologous overexpression of Fno from the pET24b-Fno vector in *E. coli C41(DE3)* cells using LB medium results in robust cultures that produce approximately 9 g/L culture after the induction period. In the SDS-PAGE analysis of cleared lysates (Figure 3.2), a significant band slightly above the 26 KDa molecular weight marker is

apparent and is assigned as Fno. The molecular weight of Fno is smaller (approximately 23 KDa) as calculated from the amino acid sequence using ProtParam (*97*). However, the mobility observed here matches that of Fno purified directly from *A. fulgidus*, which runs with an apparent molecular mass of 28 kDa (*72*).

*3.3.3 Purification of Fno*

To monitor each purification step, aliquots were assayed to determine total protein, total Fno activity, specific activity, the ratio of absorbance at 260 nm and 280 nm ($Abs_{260/280}$ nm), yield, fold purification, and to resolve by SDS-PAGE (Table 3.1, Figure 3.2). The heat denaturation / precipitation of non-thermotolerant proteins is shown to be the most effective purification step, although this step is also accompanied by the largest loss in yield and does not significantly impact the initial $Abs_{260/280}$ nm ratio. The subsequent $(NH_4)_2SO_4$ precipitation step does not appear to provide any increase in Fno purity as assayed by SDS-PAGE or by specific activity, but does provide a rapid way to greatly reduce sample volume before the following step. We next introduced a polyethyleneimine precipitation step specifically intended to reduce contamination by nucleic acids. This large cationic polymer precipitates nucleic acids through an entirely different method than the $(NH_4)_2SO_4$ protein precipitation step and adds a different dimension to the purification (*99*). As intended, this precipitation step provides the most effective reduction of the $Abs_{260/280}$ nm ratio, halving the value. Further removal of nucleic acids is accomplished in the subsequent anion exchange chromatography step, which reduces the $Abs_{260/280}$ nm ratio to approximately 0.6. Additionally, this chromatographic step removes the remaining contaminating proteins visualized by SDS-PAGE and increases the specific activity. The anion exchange chromatography step is shown to be

the second most effective purification step, albeit with an accompanying loss in yield that is the second largest in the overall method. The final size exclusion chromatography step does not appear to remove any additional protein bands as gauged by SDS-PAGE (Fno already appears homogeneous), nor does it impact the specific activity. However, a small, late eluting peak is separated in the chromatogram (Figure 3.2). More importantly, the gel filtration step is a convenient and effective method to remove salt introduced in the previous step and to transition purified Fno into a different buffer system at a different pH in preparation for kinetic characterization. This overall procedure produces approximately 2 mg of homogeneous Fno/L culture volume and effectively eliminates the contaminating $Abs_{260}$ peak from the final sample (Figure 3.1).

*3.3.4 Steady-state kinetic characterization of purified Fno*

The specific activity of purified Fno was determined using the truncated $F_{420}$ cofactor $FO_{ox}$ at 23 °C and found to be 71.8 ± 0.1 U / mg. For comparison with previous published preparations, we also determined the specific activity at an elevated temperature of 65 °C to be 230 ± 20 U / mg, which is very similar to a previously reported value of 280 U / mg, determined using $F_{420}$-$2_{ox}$ (*60*). Since the molecular weight of Fno is the same in both of these preparations, this result indicates that the two preparations have similar $k_{cat}$ values for the $FO_{ox}$ and $F_{420}$-$2_{ox}$ cofactors, respectively. Our optimized purification protocol provides enzyme demonstrated to be suitable for use in monitoring catalysis during the initial linear rate of $FO_{ox}$ reduction by NADPH (Figure 2.1). We have previously used Fno purified by this method to determine $k_{cat}$ (5.3 ± 1 $s^{-1}$) and $K_m$ (4.0 ± 0.4) values while varying $FO_{ox}$ concentrations in the presence of saturating NADPH at pH 6.5, 23 °C (*63*). The $K_m$ value compares favorably with that of a previous report for *A. fulgidus* using $F_{420}$-$2_{ox}$ at the higher temperature of 65 °C ($K_m$ = 10 μM). Therefore,

although functional differences between FO and $F_{420}$ will be characterized in future experiments, their comparison here indicates that our purification protocol provides active enzyme suitable for kinetics studies.

The optimized protocol for expression and purification of *A. fulgidus* Fno presented here differs significantly from previous reports, and results in good yields of homogeneous, catalytically active, purified protein that lacks any significant contaminants with $Abs_{260}$ and is suitable for kinetic studies. This protocol will accelerate studies of Fno and how this thermophilic enzyme interacts with and manipulates the reactivity of its unusual $F_{420}$ cofactor during catalysis.

Chapter 4

# EVIDENCE OF NEGATIVE COOPERATIVITY AND HALF-SITE REACTIVITY WITHIN AN $F_{420}$-DEPENDENT ENZYME: KINETIC ANALYSIS OF $F_{420}H_2$:NADP+ OXIDOREDUCTASE

## 4.1 Introduction

Here, we report the first pre-steady state kinetic analysis of Fno hydride transfer activity. Our data suggest that this enzyme exhibits kinetic behavior consistent with negative cooperativity and half-site reactivity (*100-102*). Several enzymes display either negative cooperativity or half-site reactivity (*102, 103-112*). Two flavin dependent enzymes have been reported recently. For example, Flavin reductases, related to bioluminescence (such as LuxG) have been studied by stopped-flow spectrophotometry (*102*). The data suggest that LuxG follows a sequential ordered mechanism in which NADH was the first cofactor to bind, followed by FMN. Initially the LuxG•NADH•FMN complex forms, resulting in hydride transfer. The reactions with NADH in LuxG are biphasic. The two phases were both due to reduction of FMN and each accounted for ~50% of the total absorbance change. The fractions in the two phases remained constant over a wide range of FMN concentrations. From this information, it was concluded that LuxG displays half-site reactivity and it was suggested that negative cooperativity could be involved (*102*).

A second, more complex example, was reported for mercuric reductase, a flavoprotein that catalyzes the reduction of $Hg(SR)_2$ by NADPH in a variety of bacterial strains (*112-115*). Biphasic kinetics, along with redox titration experiments, suggest half-site reactivity within this enzyme (*114*). However, the data could not distinctly confirm negative cooperativity, because three types of abnormal behavior had been observed

(*114*). Miller *et al.* observed a sigmoidal curve, with binding or activity as a function of substrate concentration that was indicative of positive cooperativity. The negative derivations observed from hyperbolic plots were indicative of a sequential negative cooperative interaction between subunits (*114*). Miller *et al.* reported models for asymmetric dimers and negative cooperativity (*114*).

Here, we report the first example of an $F_{420}$ cofactor dependent enzyme that displays both half-site reactivity and negative cooperativity. Additionally, we report, for the first time, the dissociation constants of FO and NADPH from the ternary enzyme – cofactor complex. Overall, the results obtained provide valuable new insights into the kinetics and mechanism of Fno reactions. We believe the information obtained will prove to be of significant interest in helping to elucidate the reactivity details of the numerous other $F_{420}$ dependent enzymes.

## 4.2 Materials and Methods

### *4.2.1 Reagents*

FO was synthesized as reported elsewhere (*63*). NADPH was purchased from Akron Biotech. The plasmid pET24b used for Fno gene insertion was purchased from Novagen. LB Broth was purchased from US Biologicals. Isopropyl β-D-1 thiogalactopyranoside (IPTG) was purchased from Gold Biotechnology. Potassium phosphate monobasic buffer was purchased from BDH. Potassium phosphate dibasic buffer was purchased from Amresco. MES buffer was purchased from Acros Organics. *E. coli* C41*DE3* cells were purchased from Lucigen. Kanamycin, Tris buffer and ammonium sulfate were purchased from Fisher Scientific.

*4.2.2 Expression and Purification*

The Fno gene from *A. fulgidus* was synthesized in vitro as described in the published article (*72*) and cloned into pET24b plasmid by Genescript. The plasmid was transformed into C41(DE3) *E. coli* according to Agilent Technologies protocol. The method reported by Warkentin *et al.* (*116*) was modified for the purification of Fno. Briefly, the frozen *E. coli* C41(DE3) cell stock containing the Fno gene in pET24b plasmid was inoculated in a 10 L LB culture in the presence of 50 µg/ml of kanamycin until an $OD_{600}$ of 0.6. The culture was induced with 1 mM IPTG at 37 ºC overnight followed by harvesting. The cell pellet was lysed by sonication at 4 °C after re-suspending the cells in 1.5 M potassium phosphate buffer, pH 8.0. The supernatant after centrifugation (16,000 x g) was heated in a water bath at 90 °C for 30 minutes and then centrifuged (16,000 x g). Ammonium sulfate was added to 40% and centrifuged at 16,000 g for 30 minutes. Ammonium sulfate (70%) was added to the supernatant and centrifuged at 16,000 g for 30 minutes. The ammonium sulfate precipitate was re-suspended in 50 mM Tris-HCl, pH 7.5, and was treated with 0.05% polyethylenimine. The supernatant was then dialyzed in 50 mM Tris-HCl buffer pH 7.5 overnight and loaded onto a DEAE-Cellulose from Sigma, (2.5x 6 cm), which was equilibrated with 50 mM Tris-HCl (pH 7.5). The active fractions were combined and concentrated by filtration (30 kDa cut-off) (Millipore) to about 1 mL. The 1 mL sample was loaded onto a 1 x 40 cm size exclusion column (Sephacryl S-200 HR from GE Healthcare). The column was previously equilibrated with two column volumes of 50 mM MES/NaOH (pH 6.5). The purified protein was stored at -80 °C in 50 mM MES/NaOH (pH 6.5) buffer in the presence of 20% glycerol. All column chromatography was operated through a Bio-Rad FPLC system. The concentration of the

pure protein was determined using Bradford reagent at 595 nm. A detailed report of the purification protocol will be reported elsewhere (*117*).

*4.2.3 Binding of FO and NADPH to Fno*

FO binding studies were performed using fluorescence spectroscopy (Horiba FluoroMax Spectrofluorometer). To obtain the dissociation constant ($K_d$) of FO, 0.2 μM of Fno was titrated with varying concentrations of FO in 50 mM MES/NaOH at pH 6.5. The binding assay was monitored in a Spectrosil® Quartz sub-micro cell (160 μl nominal volume) from Starna Cells. The sample was excited at 290 nm and the emission scan was performed between 300-800 nm. To obtain the $K_d$ of NADPH 0.2 μM of Fno was titrated with varying concentrations of NADPH in 50 mM MES/NaOH at pH 6.5. The binding assay was monitored in a similar fashion as described above for the FO binding studies.

The excitation and emission slit widths were 4 and 8 nm, respectively. Either 1 or 2 μl aliquots of FO (0-300 nM) or NADPH (0-1780 nM) were titrated into a solution containing Fno. A decrease in tryptophan emission at 340 nm was observed for both FO and NADPH titration and was used for calculation of the dissociation constants (*116*). A plot of substrate concentration vs normalized fluorescence was used to determine the dissociation constants.

The Hill coefficient and the dissociation constant for FO and NADPH binding were determined by fitting the plots to a sigmoidal function (Equation 4.1), using Sigma Plot version 13.0.

$$\Delta F = [F_{max} [L]^n/(K_d + [L]^n)] \qquad \text{Equation 4.1}$$

where, ΔF is the change in fluorescence emission at 340 nm caused upon addition of either FO or NADPH ligand (L), $F_{max}$ is the maximum normalized fluorescence ($F_{max}$ = 1), $K_d$ is the dissociation constant and n is the Hill coefficient. Ligand concentration was corrected for dilution during addition while inner filter effect of the protein was corrected by subtracting the initial fluorescence from the final spectra.

*4.2.4 Steady state kinetics*

The steady state kinetic measurements were carried out using a Hitech Scientific DX2 stopped-flow spectrophotometer at 22 °C. To determine the FO kinetic parameters, Fno (0.2 μM; 50 mM MES/NaOH, pH 6.5) was mixed with varying FO concentrations (1.3 μM to 30 μM), while the NADPH concentration was held constant at 600 μM in 50 mM MES/NaOH, pH 6.5.

To determine the NADPH kinetic parameters, Fno (0.2 μM; 50 mM MES/NaOH, pH 6.5) was mixed with a constant concentration FO (25 μM), while varying NADPH (~2 μM to 1 mM in 50 mM MES/NaOH, pH 6.5. The time trace measurements were collected in diode-array mode between 350-800 nm following FO reduction at 420 nm. The concentrations of NADPH and FO were determined using an extinction coefficient of 6.22 $mM^{-1}cm^{-1}$ at 340 nm (in 50 mM Tris-HCl, pH 7.4) and 41.4 $mM^{-1}cm^{-1}$ at 420 nm (in 50 mM potassium phosphate buffer, pH 7.0) respectively (*67*). The initial rate of the reaction was calculated using an extinction coefficient of 34.7 $mM^{-1}cm^{-1}$ for FO at pH 6.5 at 420 nm. The initial rate was converted to the macroscopic rate constant by dividing by the concentration of enzyme. A plot of substrate concentration vs rate constant was used to determine the steady state kinetic parameters.

The kinetic data for NADPH were fitted to the double reciprocal plot using Equation 4.2.

$$1/k = (K_m/k_{cat})(1/[S] + (1/k_{cat}) \qquad \text{Equation 4.2}$$

where, $k$ is the first order macroscopic rate constant (or turnover number) obtained by dividing the initial rate by the enzyme concentration; $K_m$ is the Michaelis constant; [S] is concentration of NADPH. The individual rate constants and $K_m$ for the two phases were obtained from linear fits of the two phases.

*4.2.5 Pre-steady state experiment*

The rapid kinetic experiments were performed in the Hitech Scientific DX2 stopped-flow spectrophotometer at 22 °C. Fno (1.0, 1.5 and 2.0 μM; 50 mM MES/NaOH, pH 6.5, respectively) was mixed with FO 25 μM) and NADPH (600 μM) in 50 mM MES/NaOH, pH 6.5. Time trace measurements were made in either single wavelength log mode at 420 nm or diode-array mode between 350-800 nm following FO reduction at 420 nm. The data were plotted to determine the pre-steady state parameters.

SigmaPlot version 13.0 was used to fit the data to the exponential decay function using Equation 4.3,

$$\text{Absorbance} = A_0 * e^{(-k*t)} - (v*t) + c \qquad \text{Equation 4.3}$$

where, $A_0$ is the amplitude of the burst phase, $k$ is the observed burst rate constant, $v$ is the observed steady state rate and c accounts for the non-zero baseline. *wt*Fno (20 μM), FO (4 μM) and NADPH (600 μM) were used for single-turnover kinetic studies. The exponential decay progress curve was fit with Equation 4.4 using SigmaPlot version 13.0.

$$\text{Absorbance} = A_0 * e(-k*t) + c \qquad \text{Equation 4.4}$$

where, $A_0$ is the amplitude, $k$ is the observed rate constant, t is time in seconds and c accounts for the non-zero baseline.

## 4.3 Results

### *4.3.1 Binding assay of wtFno*

Upon addition of FO or NADPH, the tryptophan fluorescence of Fno is quenched indicating a change in the tryptophan environment (Figure 4.1 A & C, respectively). The strong change in fluorescence intensity, as shown in Figure 4.1, with added FO or NADPH, provides an excellent method of measuring both dissociation constants (Figure 4.1 B & D) (*116*). From these fluorescence data, $K_d$ for FO binding was determined to be 3.6 ± 0.7 nM. The binding data for NADPH were fit using the Hill equation (Equation 4.1), as shown in Figure 4.1. The plot gave a Hill coefficient of 0.6 and a $K_d$ of 2.0 ± 0.3 nM.

The data was also fit to the Adair equation (not shown). This fit gave a similar $K_d$ as the Hill equation. However, the fit was better (better R value, with less error) with Hill equation.

To confirm that the binding events observed were real, we conducted a control binding experiment, under the above mentioned conditions using tryptophan, rather than, Fno. Little change in fluorescence was observed for tryptophan addition, in comparison to Fno. No clear binding events with FO could be observed for the control experiments. Binding of Tryptophan with NADPH for the control experiment did not display a good fit.

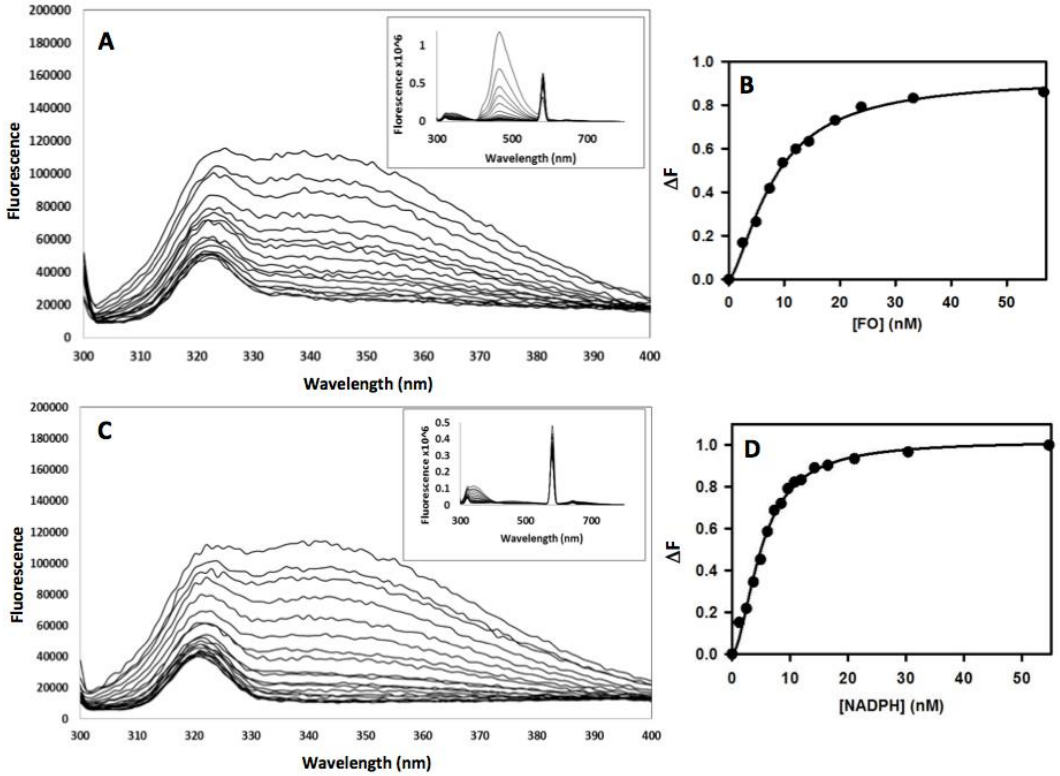


Figure 4.1 The binding of FO and NADPH to *wt*Fno was carried out in 50 mM MES/NaOH (pH 6.50) buffer at room temperature in the Fluorometer. FO or NADPH was titrated into 0.2 μM of Fno and the fluorescence emission was monitored at 340 nm after excitation at 290 nm. Actual fluorescence values were inverted and normalized before plotting. **A:** emission spectra of a *wt*Fno solution containing 0, 2.46, 4.90, 7.32, 9.71, 12.1, 14.4, 19.2, 24.0, 33.4, 57.0, 104, 151, 197, and 313 nM of FO (upper to lower spectra respectively) when excited at 290 nm. **B:** A plot of FO concentration vs normalized fluorescence upon FO addition. The solid circles represent fluorescence at various concentration of FO and the solid line represent fit to **Equation 4.1**. **C:** emission spectra of *wt*Fno solution containing 0, 1.24, 2.48, 3.70, 4.90, 6.10, 7.28, 8.45, 10.8, 11.9, 14.2, 16.5, 21.1, 30.4, 53.5, 99.5, 191, 420, 874, and 1780 nM of NADPH (upper to lower spectra respectively) when excited at 290 nm. **D:** A plot of NADPH concentration vs change in fluorescence upon NADPH addition. The solid circles represent the difference in fluorescence at various concentration of NADPH and the solid line represent fit to Equation 4.1.

*4.3.2 Steady state kinetics of wtFno*

The steady state reduction of FO, as catalyzed by Fno, yields plots of *k* versus substrate concentration that display typical saturation kinetics (Figure 2.1) (*63*). The assay was conducted at pH 6.5 to shift the absorbance peak of FO from 400 to 420 nm in order to avoid interference from NADPH. Above pH 6.5 the reaction slows down considerably.

Table 4.1 Steady state kinetic parameters for Fno catalyzing hydride transfer from NADPH to FO at 22 °C and pH 6.5 based on decrease of FO absorbance at 420 nm.

| **Substrate** | **$K_m$ (μM)** | **$k_1$ (sec$^{-1}$)** | **$k_{cat}$ (sec$^{-1}$)** |
|---|---|---|---|
| FO | 4.00 ± 0.39 | -NA- | 5.27 ± 0.14 |
| NADPH phase 1 | 2.33 ± 0.19 | 4.16 ± 0.07 | -NA- |
| NADPH phase 2 | 61.62 ± 5.87 | -NA- | 5.41 ± 0.04 |

The kinetic parameters $K_m$ and $k_{cat}$ were determined by fitting the plot of varying FO concentration (μM) versus rate constant, *k (*sec$^{-1}$*),* to the Michaelis-Menten hyperbolic equation (Figure 2.1). The $K_m$ and $k_{cat}$ determined from the plot were 4.00 ± 0.39 μM and 5.27 ± 0.14 sec-1, respectively (*63*).

The steady state kinetic parameters for NADPH were determined under the same conditions as described for FO by varying NADPH at a constant FO concentration of 25 μM (final concentration). When NADPH was varied, a plot of NADPH concentration vs *k* (sec$^{-1}$) did not display the typical hyperbola at NADPH concentrations greater than 100 μM. The plot displayed non Michaelis-Menten behavior with increasing concentrations of NADPH. The two phases included a steeper phase at low

concentrations of NADPH. The steady state parameters were determined by using Equation 4.2 as shown in Figure 4.2 using a double reciprocal plot.

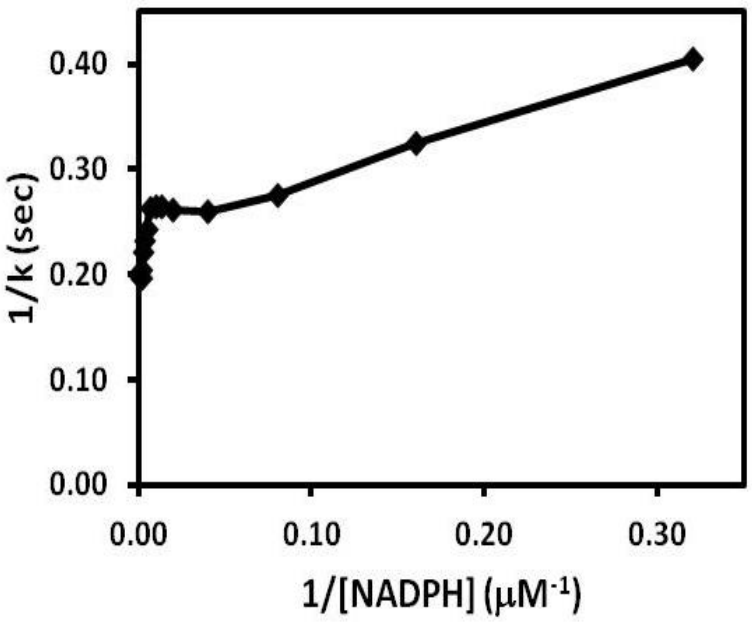


Figure 4.2 A double-reciprocal plot for steady state kinetics of varying NADPH concentrations is plotted using equation 4.3. The reaction is carried out in 50 mM MES/NaOH (pH 6.5) buffer at 22 °C in a stopped-flow spectrophotometer. A constant FO concentration of 25 μM was used. The kinetic parameters are shown in Table 4.1. The plot shows a concave downward curve typical of negative cooperativity

The macroscopic rate constants for the first and second phases are 4.16 ± 0.07 $sec^{-1}$ and 5.41 ± 0.04 $sec^{-1}$, respectively. The rate constant for the second phase matches with the $k_{cat}$ obtained for steady state kinetics varying FO. The values for $K_{m1}$ and $K_{m2}$ were 2.33 ± 0.19 μM and 61.6 ± 5.9 μM, respectively.

The $K_m$ is vastly different from the determined $K_d$. The dissociation constant determination was conducted with just Fno and FO, or Fno and NADPH, but not in the presence of both. The $K_m$ is determined in the presence of both FO and NADPH. If Fno undergoes conformational changes depending upon the presence of the cofactors, this

could affect the enzyme's affinity for the cofactor. Therefore, we determined the $K_d$ of $NADP^+$, which does not absorb at 290 nm (no inner filter effect). Next, we used this number to determine the $K_d$ of oxidized FO in the presence of $NADP^+$. The dissociation constants for $NADP^+$ as well as FO in the presence of $NADP^+$ were all in the low nM range. The difference between $K_m$ and $K_d$ could be due to the motion of Fno during catalysis. This could have an effect on the $K_m$ of both cofactors. However, no catalysis occurs with the binding experiments, which limits the motion of Fno.

*4.3.3 Pre-steady state kinetics of wtFno*

A solution containing *wt*Fno was mixed with equal volumes of solutions containing FO and NADPH in the stopped-flow spectrophotometer. The reduction of the FO peak was monitored by absorbance changes at 420 nm. Spectra collected at different time intervals within the wavelength range of 350 – 800 nm did not show any formation of new peaks during the reaction, suggesting the absence of any observable intermediate peaks for reduction of FO by NADPH. However, the reaction progress curve exhibited initial burst kinetics, followed by a steady state rate, as shown in Figure 4.3A. These data were then fit using equation 4.3. The burst kinetics suggests that the rate limiting step is after the hydride transfer step. The rate limiting step is either product release or a conformational change. The hydride transfer reflected by the fast burst phase is 71.7 ± 1.9 $sec^{-1}$ and the steady state rate constant of 4.56 ± 0.03.

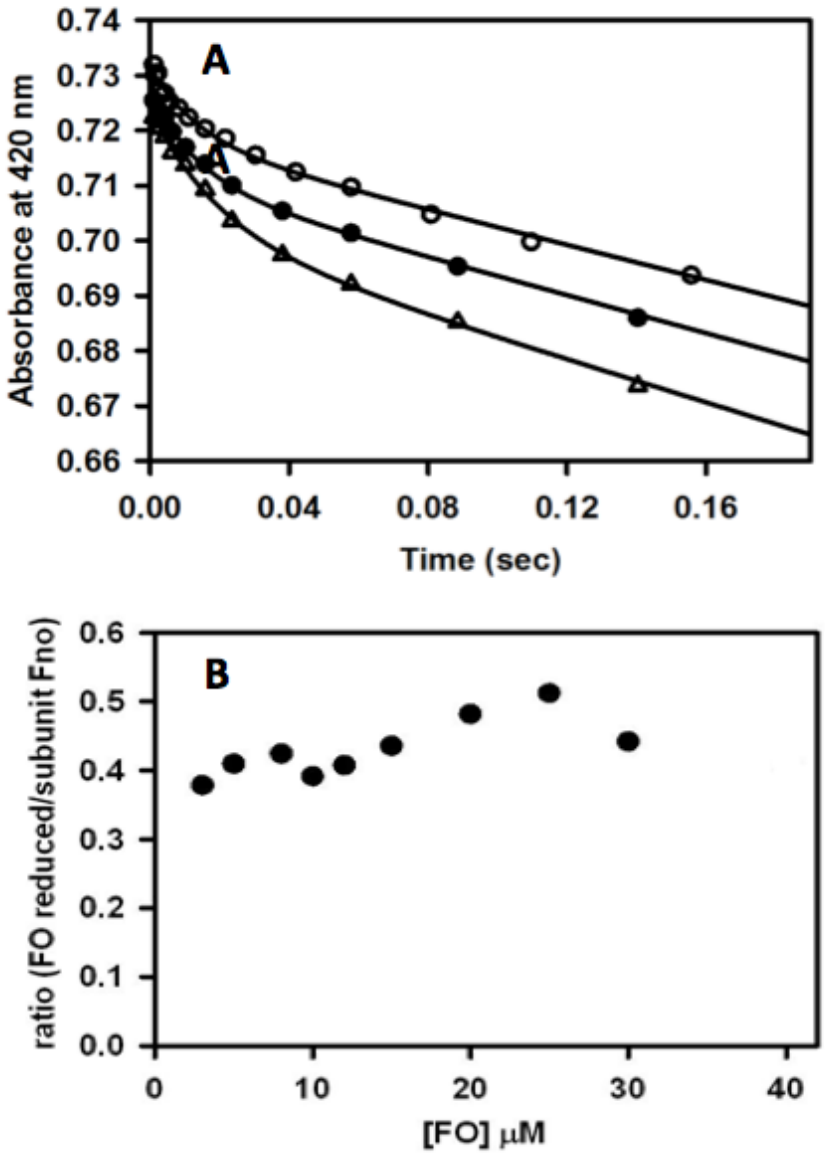


Figure 4.3 Pre-steady state kinetics **A:** The pre-steady state kinetics of hydride transfer to FO from NADPH by Fno is shown for varying Fno concentrations – 1.0 μM (open circle), solid circle (1.5 μM) and open triangle (2.0 μM). The solid lines represent fit using Equation 4.4. The reaction was carried out in 50 mM MES/NaOH (pH 6.5) buffer at 22 °C in the stopped-flow spectrophotometer using 25 μM FO and 600 μM NADPH. The progress curve shows biphasic kinetics with an initial burst phase followed by a steady state phase. **B:** Plot of ratio of FO reduced per Fno subunit with varying FO concentration shows half-sites reactivity.

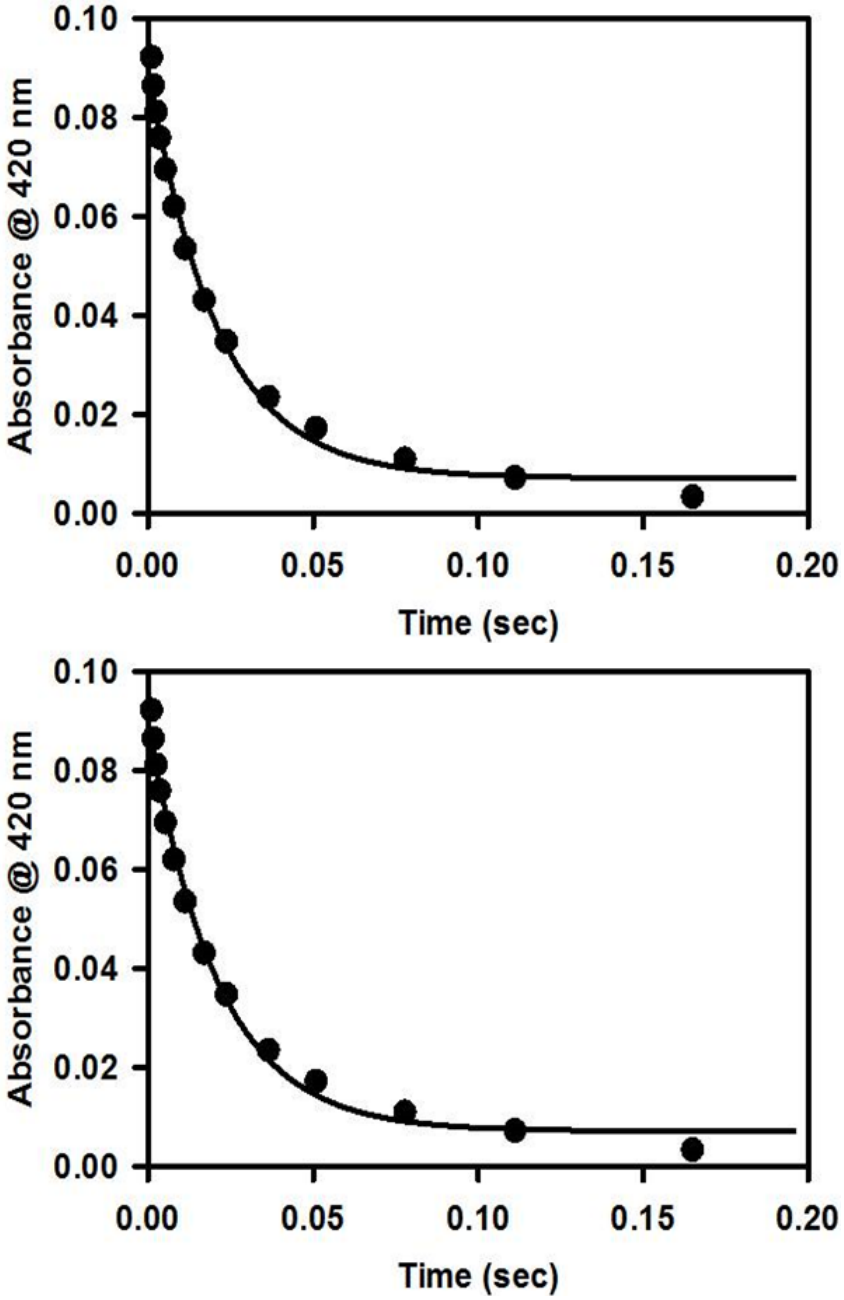


Figure 4.4 Single-Turnover kinetics. Kinetic trace of FO reduction under single-turnover conditions. The solid line represents the curve fit using the single exponential decay equation (equation 4.4). The upper (A) and lower (B) panels represent single-turnover experiments without and with pre-incubation of NADPH with *wt*Fno, respectively.

The magnitude of the burst was directly proportional to the concentration of *wt*Fno. The magnitude of the burst for 1.0, 1.5 and 2.0 μM *wt*Fno corresponds to 0.37, 0.46 and 0.63 μM of FO reduced by NADPH, respectively. This averages out to be 30-37% of product formation (hydride transfer) during the burst phase. This suggests the half-sites reactivity model given in Scheme 4.1 for *wt*Fno. To make sure that the half-sites reactivity is not an artifact, we verified the purity of the enzyme. The *wt*Fno sample is of high purity as indicated by SDSPAGE and gel filtration chromatography (*63*). Further investigation for half-sites reactivity was performed as discussed below by studying the effect of burst amplitude on increasing FO concentration.

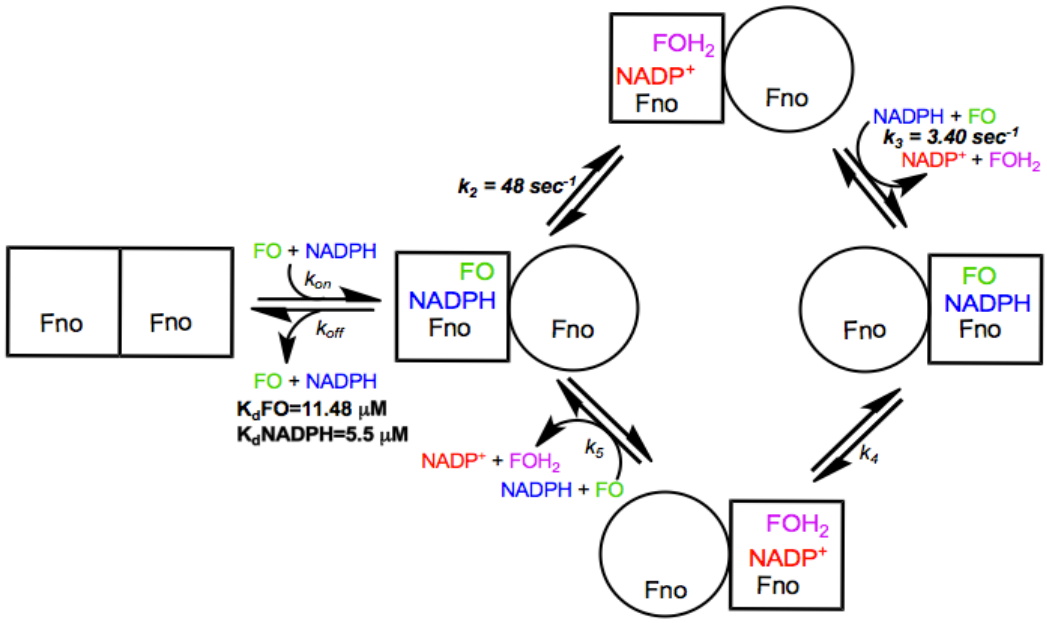


Scheme 4.1 The steady state, pre-steady state as well as binding data revealed allosteric nature of Fno. Based on this model, the hydride transfer reaction from NADPH to FO occurs at one subunit. Once the product(s) is released from one subunit the hydride transfer reaction occurs at the second subunit. Followed by the release of the products from the second subunit, the first subunit is re-engaged for the reaction.

A plot of FO concentration versus burst amplitudes was observed to be ~50% of FO reduction (Figure 4.3b). This supports half-sites reactivity in Fno as indicated earlier

in this section. The $k_{obs}$ under single-turnover conditions (Figure 4.4) were determined as 47.86 ± 0.50 $sec^{-1}$ using Equation 4.4. This is similar to the observed burst rate constant, suggesting that the burst rate constant represents the hydride transfer from NADPH to FO. Pre-incubation of *wt*Fno with NADPH under single-turnover conditions also gave a similar $k_{obs}$ of 53.78 ± 0.60 $sec^{-1}$.

## 4.4 Discussion

Negative cooperativity is a phenomenon that has been observed in a variety of protein systems (*103, 105-106, 118-124*). For multi-subunit proteins in particular (such as Fno) the specific phenomenon in which the affinity is higher for the first ligand, than the second ligand is known as negative cooperativity (*74, 100*). Negative cooperativity can also be described as a decrease in ligand affinity with increasing ligand concentration.

In our study, the steady state kinetic plot for NADPH exhibits a non-hyperbolic curve at concentrations greater than 100 μM. The first phase (NADPH concentrations between 0-100 μM) was determined to be steeper with a lower $K_m$ compared to the second phase (NADPH concentrations between 100-800 μM). The double reciprocal plot with NADPH showed a downward curvature at high substrate concentration, suggesting negative cooperativity (Figure 4.3). This indication of negative cooperativity is explained in detail by the Koshland-Nemethy-Filmer (KNF) model (*118*). Based on this model the protein is assumed to exist in one conformation in the absence of ligand. Once a ligand binds to one site of the protein, it causes a conformational change that is transmitted to a vacant subunit (Scheme 4.1).

Such observations of negative cooperativity in enzyme kinetics were made in one of the initial studies reported by Lewtizki and Koshland for Cytidine Triphosphate (CTP)

synthetase (*74, 101*). Out of several molecular events suggested by them, negative homotropic kinetics for Fno could be due to ligand-induced conformational changes that affect subunit interactions as suggested by our studies.

The crystal structure of Fno reveals that the binding of NADP shows a considerable number of interactions within the Fno active site as compared to the deazaflavin cofactor. Once a NADPH molecule is bound to Fno and the hydride is transferred to FO, it would be easy for $FOH_2$ to be released from the Fno active site. However, the release of NADPH could cause considerable conformation changes that are transmitted to the active site of the other subunit (also accounting for differences between the $K_m$ and $K_d$). This could also account for the strong negative cooperativity observed in the kinetic behavior of NADPH with Fno. This mechanism of action would also suggest the possibility of half-sites reactivity. In fact, our pre-steady state kinetics data through half-site reactivity indicate that only one subunit of Fno is catalytically active at a time. Such half-site reactivity is referred to as extreme cases of negative cooperativity (*119*). There are few flavin dependent oxidoreductases that are reported to exhibit half-sites reactivity. Similar half-sites reactivity is observed in the bacterial 7-acetylflavo-GADPH wherein about 42% of the enzyme-bound flavin cofactor are reduced in a very rapid step followed by a slow step (*101*). A recent finding for another oxidoreductase, Flavin Oxidoreductase LuxG, also shows half-sites reactivity (*102*). Our findings for Fno are the first reports in $F_{420}H_2$: $NADP^+$ oxidoreductases and suggest that Fno is a regulatory enzyme within archaea that is essential for controlling NADPH concentrations and related cellular function. The reaction of Fno is an equilibrium reaction. Metabolites within the cell can change the direction of the equilibrium, depending upon the needs of the cell for NADPH.

Based upon the steady state and pre-steady state kinetics presented here (half-site reactivity), we propose a mechanism for Fno (Scheme 4.1). Initially, FO and NADP bind into the active site of one monomer, followed by the first hydride transfer. This is the first (and fast) phase described in Figure 4.4. Given that the pre-steady state kinetic results reveal burst kinetics, it is plausible that the slow step is product release from the active site, upon binding of FO and NADP into the active site of the second monomer. These steps are followed by a second hydride transfer and product is released again from the active site of the second monomer. FO and NADP both appear to be substrates, which leave the active site, as opposed to cofactors that stay bound within the enzyme.

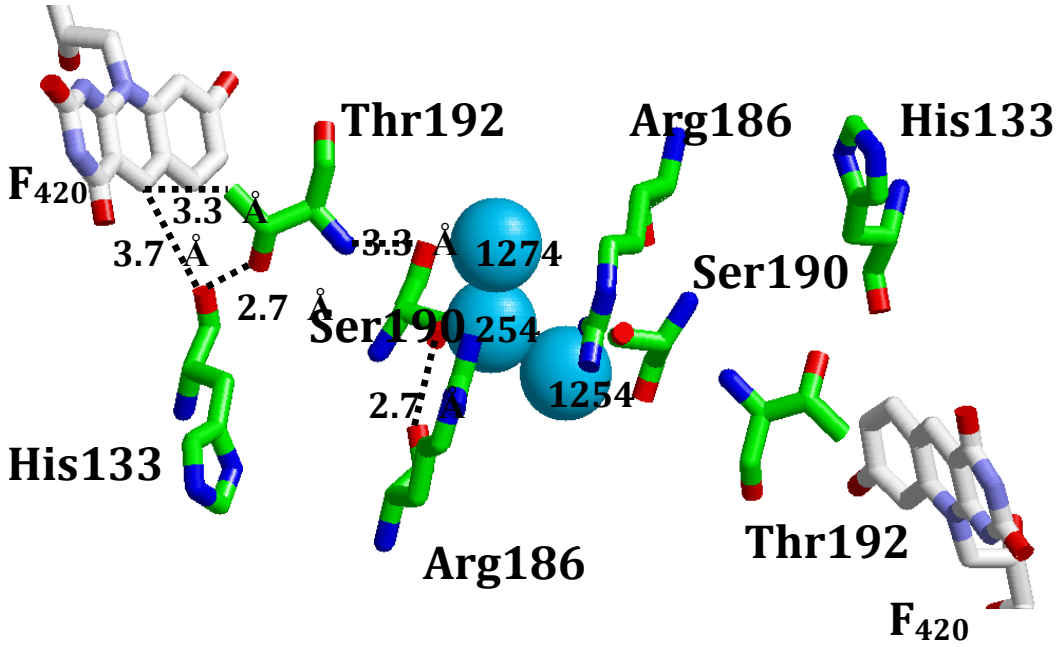


Scheme 4.2 Active site connectivity in Fno homodimer is shown here. Proximities and H-bonds are shown in Fno crystal structure from 1JAY pdb file. Both active sites are connected through a series of H-bonds. As shown for subunit A, similar interactions are observed in subunit B. At the interface of the subunit interactions are Ser190, Arg186 and 3 water molecules (1274, 254 and 1254). Thr192 forms H-bond with Ser190 which is at the subunit interface. Ser190 also forms H-bond with another subunit interface residue, Arg186. Both Arg186 and Ser190 on either subunits form H-bonds.

To understand the possible mechanism of negative cooperativity and half-sites reactivity, we took a closer look at the Fno crystal structure that revealed active site connectivity as shown in Scheme 4.2. His133 and Thr192 are located close to the C5 atom of $F_{420}$ cofactor where the hydride transfer occurs, but do not appear to form any H-bonds with any oxygen or ring nitrogen. The main chain nitrogen of Thr192 forms a H-bond with the main chain oxygen of Ser190, which is at the subunit-subunit interface. The side chain oxygen of Ser190 forms a H-bond with another residue at the interface, Arg186. The side chain amino groups of Arg186 of both the subunits could form H-bond with each other while the side-chain oxygens of Ser190 on both subunits are connected through two water molecules at the interface. We propose that these interactions at the subunit-subunit interface provide the molecular basis for inter-subunit communication during catalysis and play a regulatory role in the negative cooperativity observed in Fno kinetic studies.

Chapter 5

# KINETIC ANALYSIS OF I135 FNO VARIANTS

## 5.1 Introduction

Isoleucine is a conserved amino acid within many enzymes that utilize NADPH. It is believed that this amino acid functions to anchor the utilized cofactors within the active site of enzymes, providing an optimal position for hydride transfer. Within Fno, the residue numbering for the conserved active site isoleucine (I) is I135.

Dihydrofolate reductase (DHFR), is a separate enzyme that is essential for nucleic acids and protein synthesis and therefore, cell survival and also has a conserved active site Isoleucine residue (I14)[6]. I14 within DHFR was converted into an alanine, valine and glycine in order to study not only the functionality of the amino acid, but to examine the effects of I14 upon hydride tunneling, using kinetic isotope effects methods. The data showed a temperature dependent kinetic isotope effect as well as hydride tunneling (*8*).

While DHFR has no direct link to Fno, the two enzymes do have two commonalities. They both participate in hydride transfer reactions and they both have a conserved isoleucine residue. Such studies have not been performed on Fno, nor other $F_{420}$ dependent enzymes. There is only a distance of 3.1 Å between the carbonyl oxygen of I135 and atom C4 of NADP (Figure 5.1) (*60*). Our initial goal is to characterize the Fno I135 residue, using steady state and pre-steady state kinetic methods. We would like to further these studies with kinetic isotope effects experiments. However, that project is beyond the scope of this thesis.

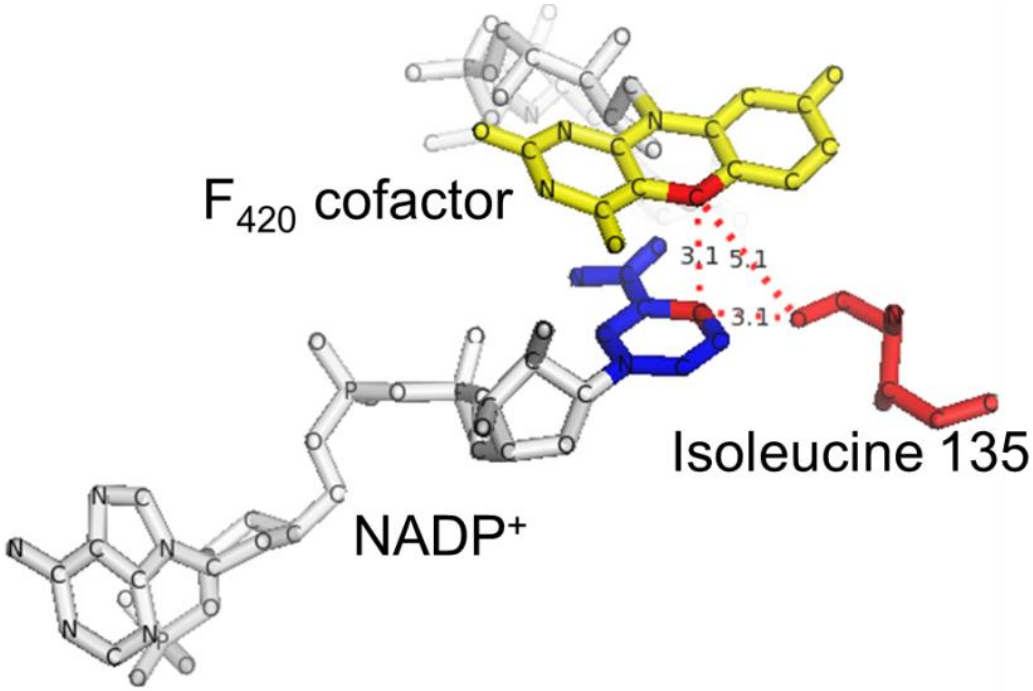


Figure 5.1 Fno active site. I135 residue is also shown (*60*).

## 5.2 Materials and Method

### *5.2.1 Reagents*

NADPH was purchased from Akron Biotech. Isopropyl β-D-1 thiogalactopyranoside (IPTG) was purchased from Gold Biotechnology. FO was synthesized as reported elsewhere (*63*). $KH_2PO_4$ buffer was purchased from BDH. Potassium phosphate dibasic buffer was purchased from Amresco. MES buffer was purchased from Acros Organics. Kanamycin, Tris buffer and ammonium sulfate were purchased from Fisher Scientific. LB Broth was purchased from US Biologicals.

*5.2.2 Mutagenesis*

Cloning of the Fno gene into the pET24b plasmid was conducted by the company, Genescript. The plasmid pET24b used for Fno gene insertion was purchased from Novagen. Site-directed mutations were generated in pET24b using QuikChange site directed mutagenesis (Stratagene), according to the manufacturer's protocol. Site directed mutants and their corresponding primers are described in Table 5.1 and Figure 5.2. Mutations were verified by plasmid DNA sequence analysis using vector specific sequencing primers. The R chain of the I135 residue of the *wt*Fno was decreased by mutating I135 to a valine, alanine and glycine. Table 5.1 displays the primer design for the desired mutations.

Table 5.1 Designed Primers for Fno Site Directed Mutagenesis studies

| **Fno variant** | **Sequence (5' to 3')** |
|---|---|
| *wt*Fno | GCC CTG CAC ACG **ATC** CCG GCA GCT CGT TTT |
| I135Af | GCC CTG CAC ACG **GCC** CCG GCA GCT CGT TTT |
| I135Arc | AAA ACG AGC TGC CGG **GGC** CGT GTG CAG GGC |
| I135Gf | GCC CTG CAC ACG **GGC** CCG GCA GCT CGT TTT |
| I135Grc | AAA ACG AGC TGC CGG **GCC** CGT GTG CAG GGC |
| I135Vf | GCC CTG CAC ACG **GTC** CCG GCA GCT CGT TTT |
| I135Vrc | AAA ACG AGC TGC CGG **GAC** CGT GTG CAG GGC |

```
CGT GTG GCT CTG CTG GGC GGT ACG GGC AAC CTG GGC AAA GGT CTG GCA CTG CGT CTG GCA ACC 69
 R   V   A   L   L   G   G   T   G   N   L   G   K   G   L   A   L   R   L   A   T  21
CTG GGT CAT GAA ATC GTG GTC GGC TCA CGT CGC GAA GAA AAA GCG GAA GCC AAA GCG GCC GAA132
 L   G   H   E   I   V   V   G   S   R   R   E   E   K   A   E   A   K   A   A   E  42
TAT CGT CGC ATT GCA GGC GAT GCT TCG ATC ACC GGT ATG AAA AAC GAA GAC GCA GCT GAA GCG195
 Y   R   R   I   A   G   D   A   S   I   T   G   M   K   N   E   D   A   A   E   A  63
TGC GAT ATT GCC GTG CTG ACC ATC CCG TGG GAA CAT GCA ATT GAC ACG GCT CGT GAT CTG AAA258
 C   D   I   A   V   L   T   I   P   W   E   H   A   I   D   T   A   R   D   L   K  84
AAT ATT CTG CGC GAA AAA ATC GTT GTT AGT CCG CTG GTG CCG GTT TCC CGT GGT GCC AAA GGT321
 N   I   L   R   E   K   I   V   V   S   P   L   V   P   V   S   R   G   A   K   G 105
TTT ACC TAC AGC TCT GAA CGC TCA GCG GCC GAA ATT GTT GCC GAA GTC CTG GAA AGC GAA AAA384
 F   T   Y   S   S   E   R   S   A   A   E   I   V   A   E   V   L   E   S   E   K 126
GTC GTG TCT GCC CTG CAC ACG ATC CCG GCA GCT CGT TTT GCA AAC CTG GAT GAA AAA TTC GAC447
 V   V   S   A   L   H   T   I   P   A   A   R   F   A   N   L   D   E   K   F   D 147
TGG GAT GTC CCG GTG TGT GGC GAT GAC GAT GAA AGC AAA AAA GTT GTC ATG TCA CTG ATT TCG510
 W   D   V   P   V   C   G   D   D   D   E   S   K   K   V   V   M   S   L   I   S 168
GAA ATT GAT GGT CTG CGT CCG CTG GAT GCC GGT CCG CTG AGT AAT TCC CGC CTG GTT GAA TCT573
 E   I   D   G   L   R   P   L   D   A   G   P   L   S   N   S   R   L   V   E   S 189
CTG ACG CCG CTG ATT CTG AAC ATT ATG CGT TTT AAC GGT ATG GGC GAA CTG GGT ATC AAA TTT636
 L   T   P   L   I   L   N   I   M   R   F   N   G   M   G   E   L   G   I   K   F 210
CTG TGA                                                                          642
 L  STOP                                                                         211
```

| | | | |
|---|---|---|---|
| 1. | *wt*Fno | 5' ATC 3' | Isoleucine |
| 2. | I135A Fno | 5' GCC 3' | Alanine |
| 3. | I135G Fno | 5' GGC 3' | Glycine |
| 4. | I135V Fno | 5' GTC 3' | Valine |

Figure 5.2 Site directed mutants and their corresponding primers.

*5.2.3 Transformation, Expression and Purification*

*E. coli* C41*DE3* cells from Lucigen were used for expression of Fno. The pET24b vector, containing the optimized Fno gene was transformed into *E. coli* C41*DE3* cells from Lucigen. *wt*Fno and Fno variants were expressed and purified under the same conditions as described in chapter 2.

*5.2.4 Binding of FO and NADPH to Fno*

The FO and NADPH binding studies of the *wt*Fno were described in chapter 4. The binding studies for the isoleucine variants were performed under the same conditions. The Hill coefficient and the dissociation constant for FO and NADPH binding were determined by fitting the plots to a Equation 4.1 using Sigma Plot version 13.0.

*5.2.5 Steady state kinetics*

Steady-state kinetic studies of the Fno variants were performed aerobically, using Varian Cary-300 spectrophotometer at 22 °C. Initial velocities for mutants were determined by following the reduction of the FO Cofactor with NADPH at 22°C and pH 6.5. The reaction was initiated by addition of NADPH and was measured by following the decrease of absorbance at 420 nm due to the reduction of FO.

The FO and NADPH kinetic parameters for Fno variants were under the same conditions as discussed for *wt*Fno in chapter 4. To determine the FO kinetic parameters, Fno variants (0.2 μM; 50 mM MES/NaOH, pH 6.5) was mixed with varying FO concentrations (1.3 μM to 30 μM), while the NADPH concentrations were held constant at 600 μM in 50 mM MES/NaOH, pH 6.5. To determine the NADPH kinetic parameters, Fno

variants (0.2 μM; 50 mM MES/NaOH, pH 6.5) were mixed with a constant concentration FO (25 μM), while varying NADPH (~2 μM to 1 mM) in 50 mM MES/NaOH, pH 6.5.

The initial rate of the reaction was calculated using an extinction coefficient of 34.7 $mM^{-1}cm^{-1}$ for FO at pH 6.5 at 420 nm. The initial rate was converted to the macroscopic rate constant by dividing by the concentration of enzyme. A plot of substrate concentration vs rate constant was used to determine the steady state kinetic parameters. The kinetic data for NADPH were fitted to the double reciprocal plot using Equation 4.2. The individual rate constants and $K_m$ for the two phases were obtained from linear fits of the two phases.

*5.3.6 Pre-steady state experiment*

The pre-steady state kinetic analysis for the Fno variants conducted under the same conditions as described in chapter 4 for wtFno. The rapid kinetic experiments were performed in the Hitech Scientific DX2 stopped-flow spectrophotometer at 22 °C. SigmaPlot version 13.0 was used to fit the data to the exponential decay function using Equation 4.3. The exponential decay progress curve was fit with Equation 4.4 using SigmaPlot version 13.0.

## 5.3 Results

*5.3.1 Binding assay of I135 variants*

In Chapter 4, we have discussed the binding of FO and NADPH to *wt*Fno. The experimental conditions and observation for Fno variants (I135V, I135A, I135G) were similar to *wt*Fno. Upon addition of FO or NADPH, the tryptophan fluorescence of Fno was quenched, indicating a change in the tryptophan environment (Figure 4.1 A & C,

respectively). The binding isotherms of *wt*Fno and Fno variants for both FO and NADPH are shown in Figures 5.3 and 5.4 and displays a typical hyperbolic shape.

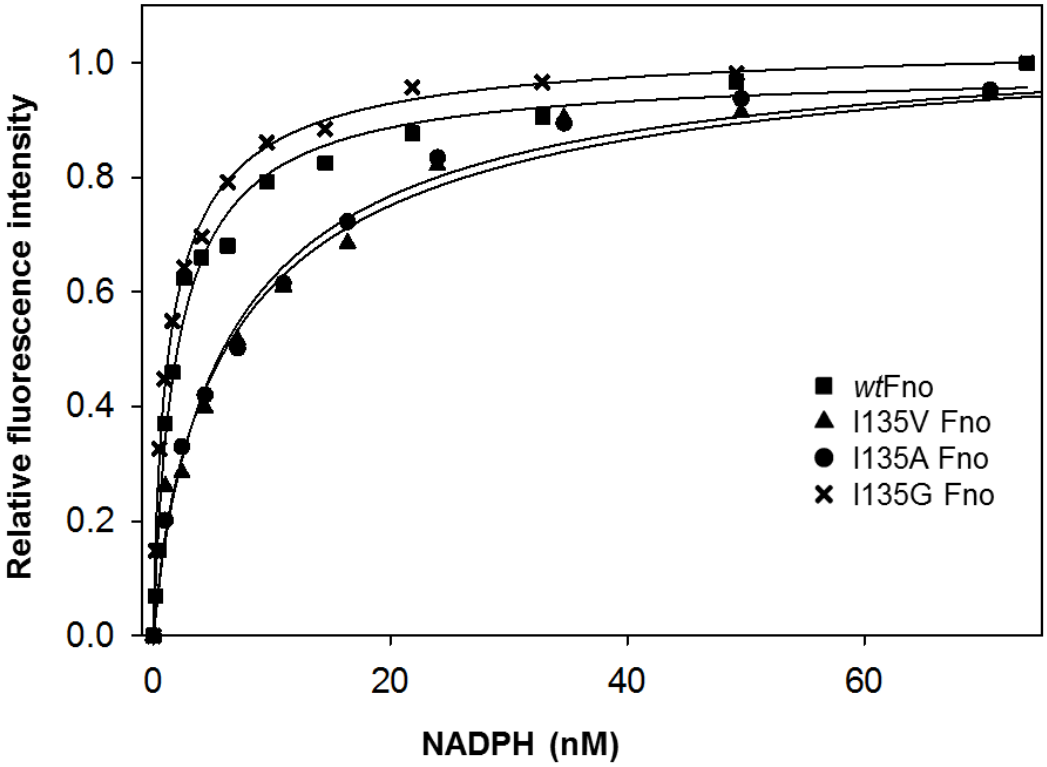


Figure 5.3 The binding of NADPH to *wt*Fno and I135 variants. The experiment was carried out in 50 mM MES/NaOH (pH 6.50) buffer at room temperature in the Fluorometer. NADPH was titrated into 0.2 µM of Fno and the fluorescence emission was monitored at 340 nm after excitation at 290 nm. Actual fluorescence values were inverted and normalized before plotting. Plots of NADPH concentration vs change in fluorescence upon NADPH addition are shown for *wt*Fno and three variants. The solid circles represent the difference in fluorescence at various concentration of NADPH and the solid line represent fit to equation 4.1.

The $K_d$ for FO and NAPDH binding to *wt*Fno and variants were determined and reported on Table 5.2. The binding data were fit using the Hill equation (Equation 4.1), as shown in Figure 5.3 for NADPH and Figure 5.4 for FO. The plots gave a Hill coefficient of less than 1.0. The mutant data was also fit to the Adair equation (not shown). This fit

gave a similar $K_d$ as the Hill equation. However, the fit was better (better R value, with less error) with Hill equation.

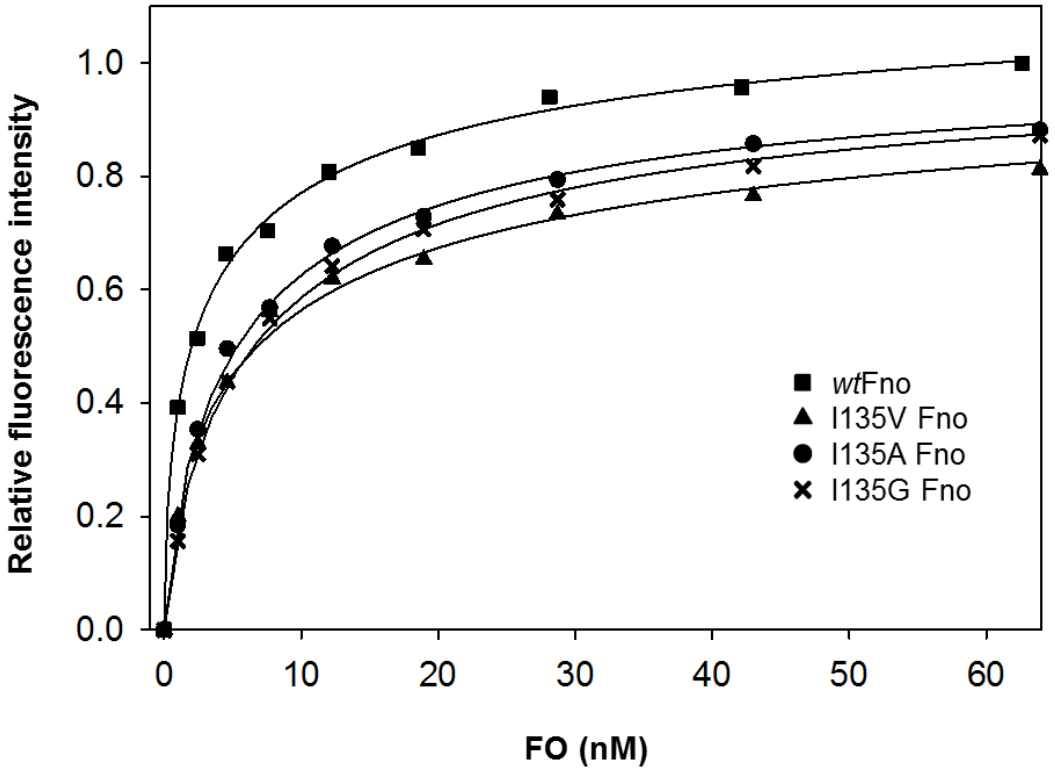


Figure 5.4 The binding of FO to *wt*Fno and I135 variants. The experiment was carried out in 50 mM MES/NaOH (pH 6.50) buffer at room temperature in the Fluorometer. NADPH was titrated into 0.2 µM of Fno and the fluorescence emission was monitored at 340 nm after excitation at 290 nm. Actual fluorescence values were inverted and normalized before plotting. Plots of FO concentration vs change in fluorescence upon NADPH addition are shown for *wt*Fno and three variants. The solid circles represent the difference in fluorescence at various concentration of NADPH and the solid line represent fit to Equation 4.1.

Table 5.2 Dissociation constants of FO and NADPH of *wt*Fno and I135 variants.

| Fno | FO (nM) | NADPH (nM) |
|---|---|---|
| I135 | 3.6 ± 0.7 | 2.0 ± 0.3 |
| I135V | 7.5 ± 0.9 | 7.4 ± 1.1 |
| I135A | 5.6 ± 0.2 | 6.7 ± 0.7 |
| I135G | 6.9 ± 0.3 | 1.45 ± 0.09 |

The binding studies were carried out in 50 mM MES/NaOH (pH 6.50) buffer at room temperature in the Fluorometer. FO or NADPH was titrated into 0.2 µM of Fno and the fluorescence emission was monitored at 340 nm after excitation at 290 nm.

### *5.3.2 Steady state kinetics of I135 variants*

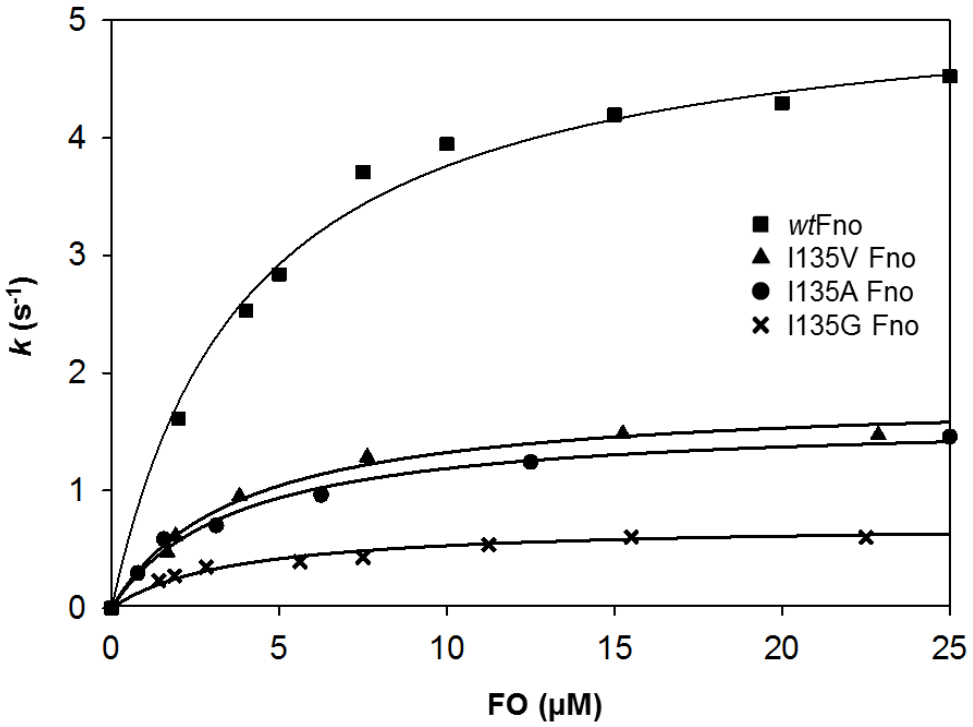


Figure 5.5 The steady state kinetics of reduction of FO by *wt*Fno and three variants are shown for varying FO concentrations. The reaction is carried out in 50 mM MES/NaOH (pH 6.5) buffer at 22 °C. A constant NADPH concentration of 600 µM was used. The plot of FO concentration vs rate constant during the steady state kinetics shows normal rectangular hyperbola. Kinetic data are summarized on Table 5.3.

The steady state reduction of FO, as catalyzed by Fno, yields plots of *k* versus substrate concentration that display typical saturation kinetics for *wt*Fno and variants. With respect to the FO cofactor, *the* $K_m$ values are the same within error (Table 5.3A and D). However, shortening the side chain will decrease the $k_{cat}$ values (Table 5.3B and D) and Fno catalytic efficiency (Table 5.3C and D). Plots of steady state for *wt*Fno and all variants are shown in Figure 5.5

Table 5.3 Steady state kinetics parameters of *wt*Fno and I135 variants w.r.t. FO. The steady state kinetics of reduction of FO by Fno is shown by varying FO concentrations.

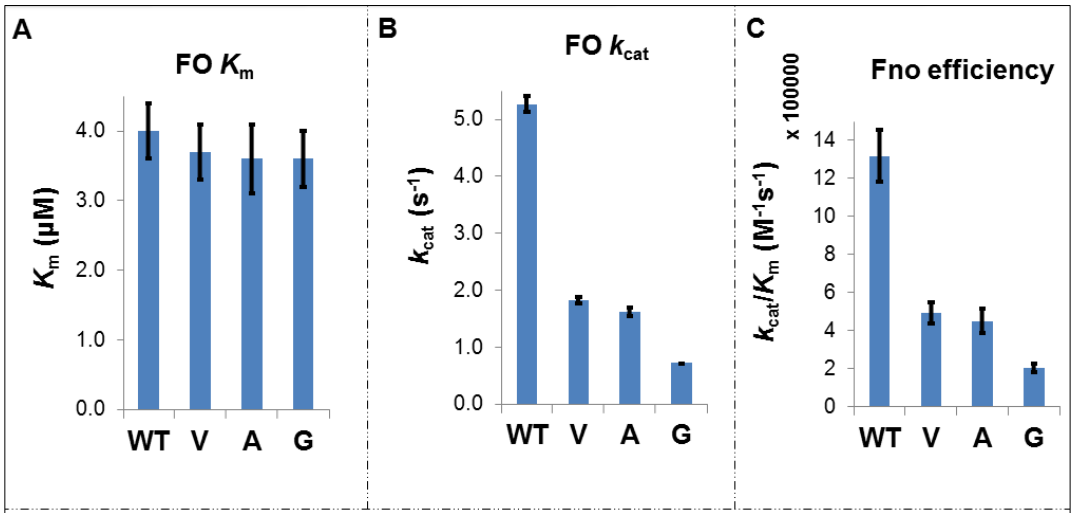


D

| Variants | Substrates | $K_m$ (μM) | $k_{cat}$ ($s^{-1}$) | $k_{cat}/K_m$ ($M^{-1}s^{-1}$) |
|---|---|---|---|---|
| WT | FO | 4.0 ± 0.4 | 5.3 ± 0.1 | $1.3 \times 10^6 \pm 1.4 \times 10^5$ |
| I135V | FO | 3.7 ± 0.4 | 1.82 ± 0.05 | $4.9 \times 10^5 \pm 5.5 \times 10^4$ |
| I135A | FO | 3.6 ± 0.5 | 1.62 ± 0.08 | $4.5 \times 10^5 \pm 6.6 \times 10^4$ |
| I135G | FO | 3.6 ± 0.4 | 0.72 ± 0.02 | $2.0 \times 10^5 \pm 2.3 \times 10^4$ |

With respect to NADPH, we observed that as chain length decreases, there is a decrease in $k_{cat.}$ and catalytic efficiency. There is also a decrease in $K_m$ values for our variants except glycine. As we have seen in *wt*Fno, plots of NADPH concentration vs *k* ($sec^{-1}$) for all three mutants also did not display the typical hyperbola at NADPH concentrations

greater than 100 μM (Figure 5.6). The plot displayed non Michaelis-Menten behavior with increasing concentrations of NADPH. The two phases included a steeper phase at low concentrations of NADPH. The steady state parameters were determined by using Equation 4.2 as shown in Figure 5.6 for *wt*Fno and all variants.

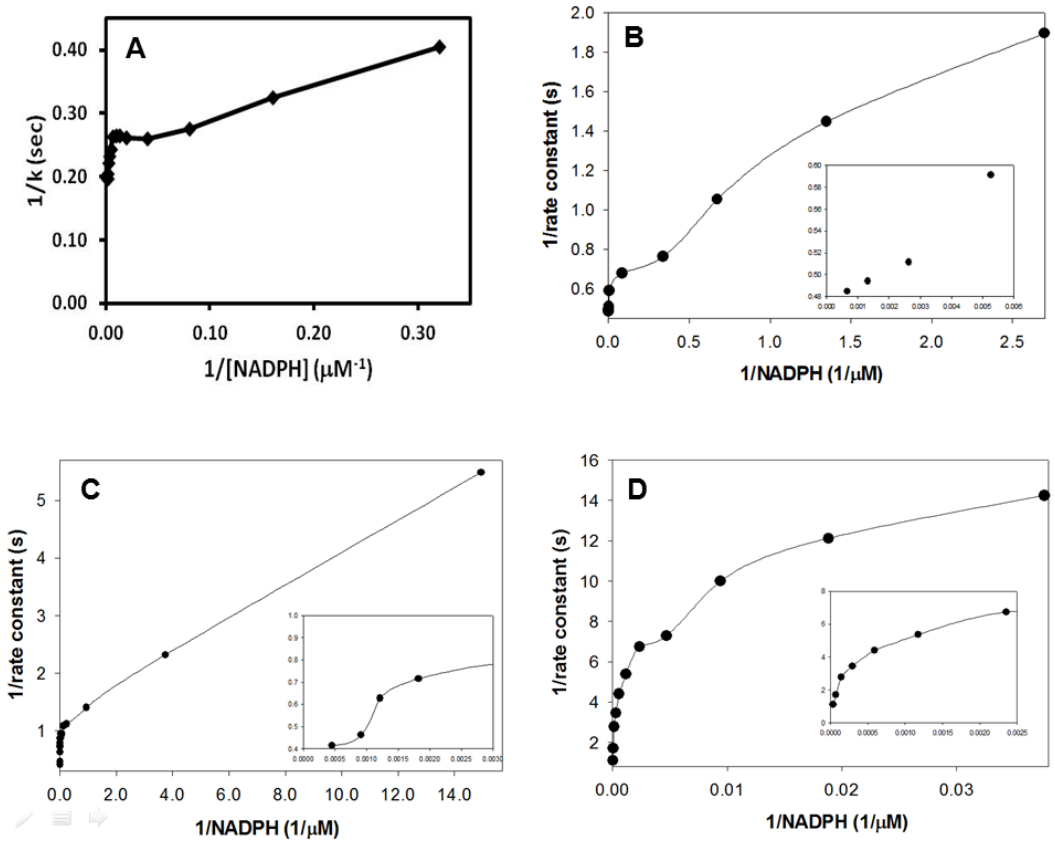


Figure 5.6 Double-reciprocal plots for steady state kinetics of *wt*Fno (**A**), I135V Fno **(B),** I135A Fno **(C)** and I135G Fno **(D)** by varying NADPH concentrations are plotted using equation 4.3. The reaction is carried out in 50 mM MES/NaOH (pH 6.5) buffer at 22 °C. A constant FO concentration of 25 μM was used. The kinetic parameters are shown in Table 5.4 and 5.5. The plot shows a concave downward curve typical of negative cooperativity

Table 5.4 Steady state kinetics parameters of *wt*Fno and I135 variants w.r.t NADPH. The steady state kinetics of reduction of FO by Fno is shown for varying NADPH concentrations. The data is shown for the first phases of the NADPH curves.

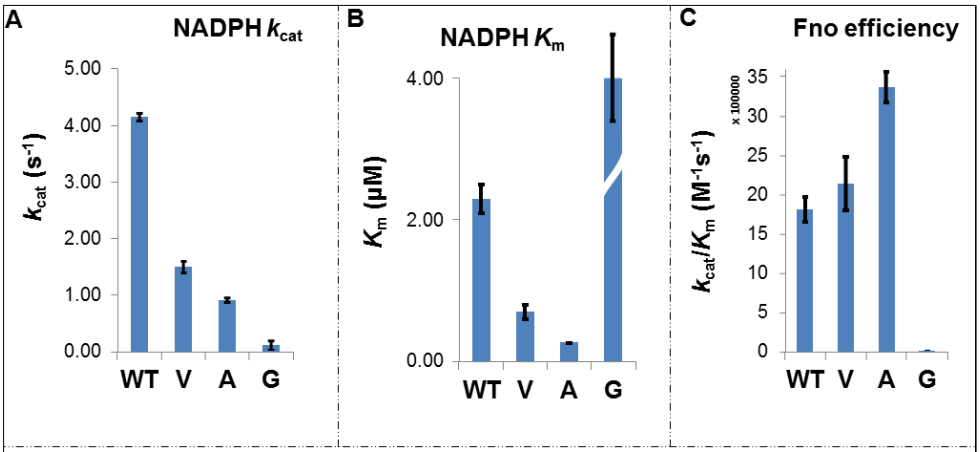


D

| Variants | Substrates | Phases | $K_m$ (µM) | $k_{cat}$ (s$^{-1}$) | $K_{cat}/K_m$ (M$^{-1}$s$^{-1}$) |
|---|---|---|---|---|---|
| ***wt*-Fno** | NAPDH | 1st | 2.3 ± 0.2 | 4.16 ± 0.07 | 1.8 x $10^6$ ± 1.6x$10^5$ |
| **I135V** | NADPH | 1st | 0.70 ± 0.10 | 1.5 ± 0.1 | 2.1 x $10^6$ ± 3.4x$10^5$ |
| **I135A** | NADPH | 1st | 0.27 ± 0.01 | 0.91 ± 0.04 | 3.4 x $10^6$ ± 1.9x$10^5$ |
| **I135G** | NADPH | 1st | 16.2 ± 3.4 | 0.11 ± .08 | 6.8 x $10^3$ ± 5.1x$10^3$ |

Table 5.5 Steady state kinetics parameters of *wt*Fno and I135 Fno variants w.r.t. NADPH. The steady state kinetics of reduction of FO by Fno is shown for varying NADPH concentrations. The data is shown for the second phases of the NADPH curves.

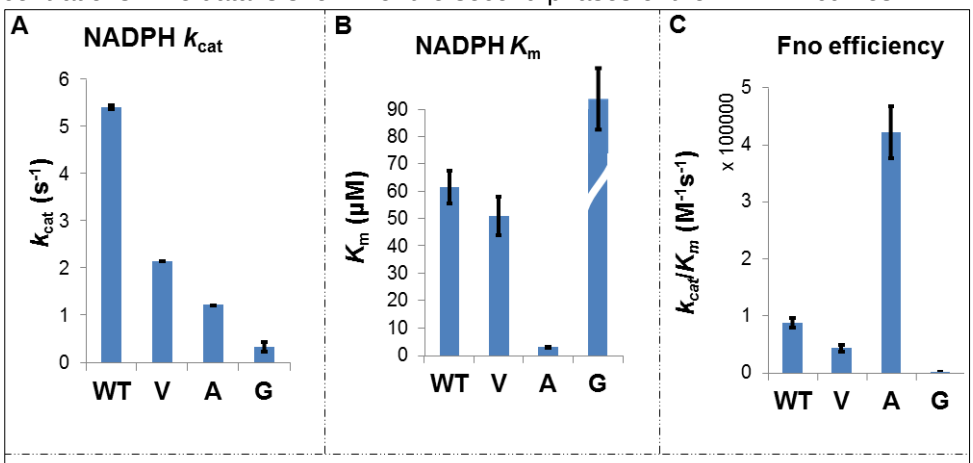


D

| Variants | Substrates | Phases | $K_m$ (µM) | $k_{cat}$ (s$^{-1}$) | $K_{cat}/K_m$ (M$^{-1}$s$^{-1}$) |
|---|---|---|---|---|---|
| ***wt*-Fno** | NAPDH | 2nd | 61.6 ± 5.9 | 5.41 ± 0.04 | 8.8 x $10^4$ ± 8.4x$10^3$ |
| **I135V** | NADPH | 2nd | 51 ± 7 | 2.16 ± 0.02 | 4.2 x $10^4$ ± 5.8x$10^3$ |
| **I135A** | NADPH | 2nd | 2.94 ± 0.31 | 1.24 ± 0.02 | 4.2 x $10^5$ ± 4.5x$10^4$ |
| **I135G** | NADPH | 2nd | 654 ± 100 | 0.33 ± 0.10 | 5.0 x $10^2$ ± 1.7x$10^2$ |

The rate constants for the first and second phases are summarized on Table 5.4 and Table 5.5. As compared to *wt*Fno, the rate constant for the second phase does not matchs with the $k_{cat}$ obtained for steady state kinetics varying FO, but they are closed. The values for $K_{m1}$ and $K_{m2}$ *(m2 for phase 2)* were also reported on Table 5.4 and 5.5. As comparing to *wt*Fno, the $K_m$ is also vastly different from the determined $K_d$. As we have mentioned on chapter 4, the difference between $K_m$ and $K_d$ could be due to the motion of Fno during catalysis. This could have an effect on the $K_m$ of both cofactors. However, no catalysis occurs with the binding experiments, which limits the motion of Fno.

### *5.3.3 Pre-steady state kinetics of I135 variants*

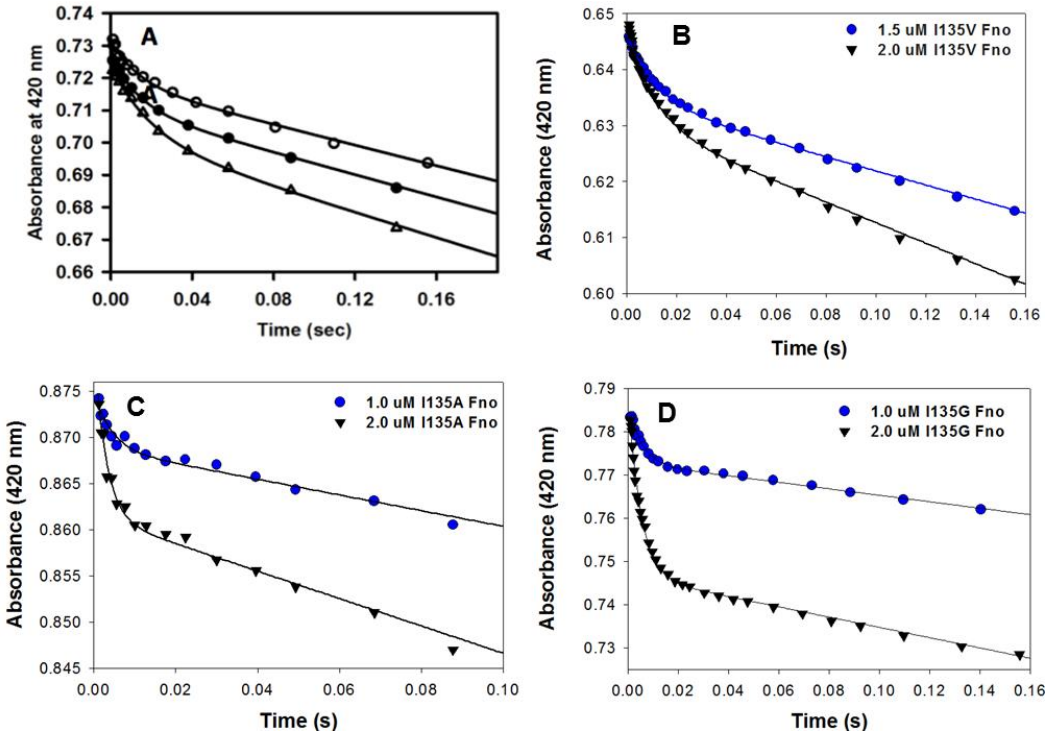


Figure 5.7 The pre-steady state kinetic trace *wt*Fno and Fno variants. Varying Fno concentrations are shown in the plots. **(A)** *wt*Fno – 1.0 μM (open circle), solid circle (1.5 μM) and open triangle (2.0 μM), **(B)** I135V Fno**, (C)** I135A Fno and **(D)** I135G Fno. The solid lines represent fit using Equation 4.4. The reaction was carried out in 50 mM MES/NaOH (pH 6.5) buffer at 22 °C in the stopped-flow spectrophotometer using 25 μM

FO and 600 µM NADPH. The progress curve shows biphasic kinetics with an initial burst phase followed by a steady state phase.

Table 5.6 Pre-steady state kinetic parameters of *wt*Fno and I135 variants:

| Fno | Fno (µM) | Burst phase | | | | | Steady state phase | |
|---|---|---|---|---|---|---|---|---|
| | | amplitude (µM) | active site (%) | avg active site (%) | k (s-1) | avg k ($s^{-1}$) | k ($s^{-1}$) | avg k ($s^{-1}$) |
| WT | 1.0 | 0.6477 | 64.77 | 54.3 ± 8.6 | 66.17 ± 4.7 | 48.18 | 3.9133 ± 0.05 | 3.40 ± 0.41 |
| | 1.5 | 0.8610 | 57.40 | | 38.55 ± 2.1 | | 3.542 ± 0.045 | |
| | 2.0 | 1.0090 | 50.45 | | 42.75 ± 1.9 | | 3.195 ± 0.030 | |
| | 2.5 | 1.1197 | 44.79 | | 45.25 ± 2.4 | | 2.969 ± 0.030 | |
| V | 1.5 | 0.349 ± 0.002 | 23 | 24 | 85.6 ± 1.6 | 92.0 ± 1.8 | 2.42 ± 0.02 | 2.54 ± 0.02 |
| | 2.0 | 0.504 ± 0.003 | 25 | | 98.5 ± 2.0 | | 2.65 ± 0.02 | |
| A | 1.5 | 0.124 ± 0.003 | 12 | 11 | 129.7 ± 7.0 | 111.5 ± 5.8 | 1.63 ± 0.02 | 1.88 ± 0.02 |
| | 2.0 | 0.196 ± 0.003 | 10 | | 93.3 ± 4.6 | | 2.14 ± 0.02 | |
| G | 1.0 | 0.403 ± 0.003 | 40 | 51 | 195.7 ± 2.8 | 199.9 ± 2.5 | 2.16 ± 0.01 | 1.93 ± 0.02 |
| | 2.0 | 1.236 ± 0.006 | 62 | | 204.1 ± 2.1 | | 1.71 ± 0.02 | |

This table summarizes the pre-steady state data of hydride transfer to FO from NADPH by wtFno and Fno variants.

FO reduction was followed by monitoring the absorbance changes at 420 nm. The reaction progress curve exhibited initial fast phase (burst), followed by a slow phase, as shown in Figure 5.7. These data were then fit using equation 4.3. The rate-limiting

step is either product release or a conformational change within Fno. The kinetic parameters of the two phases are recorded on Table 5.6.

The amplitude of the burst was also directly proportional to the concentration of *Fno variants* (Table 5.6) On average, it is about 25-60% of FO reduction (hydride transfer). These data suggest that Fno variants follow the half-sites reactivity model given in Scheme 4.1 for *wt*Fno.

## 5.4 Conclusion and Discussion

### *5.4.1 Binding of FO and NADPH to Fno*

In comparison to *wt*Fno, a decrease in FO affinity was observed for all Fno variants (Table 5.2). A decrease in NADPH affinity was observed for I135A and I135V. The $K_d$ for I135G Fno was similar to wt. This could be due to the fact that decreasing the length of the side chain affects binding with the I135A and I135V variants, but does not induce a conformational change. However, I135G by the loss of three carbons, induces a conformational change that causes the two cofactors to come into a closer proximity to one another, poising Fno for optimal hydride transfer.

### *5.4.2 Steady state kinetics of I135 variants*

The FO $K_m$ values for the Fno variants are similar to *wt*Fno. This suggests that FO $K_m$ is independent of the side chain length the 135 residue (Table 5.3) (*60*). However, as the length of the side chain decreases, there is a decrease in $k_{cat}$ as well as catalytic efficiency ($k_{cat}/K_m$) Table 5.3. The distance of 3.1 Å between the carbonyl oxygen of I135 and atom C4 of NADP(H) is of catalytic relevance (Figure 5.1) (*60*).

The steady state kinetic analysis of Fno with respect to NAPDH is summarized on Table 5.4 and Table 5.5. In comparison to *wt*Fno and with respect to the FO cofactor,

as the chain length decreases, there is a decrease in $k_{cat}$ and $K_m$ values except for glycine.

*5.4.3 Pre-steady state kinetics of I135 variants*

The pre-steady state kinetics of hydride transfer to FO from NADPH by *wt*Fno and variants are shown on Figure 5.7 and their kinetic parameters are shown on Table 57. The pre-steady state data reveals that as the length of the side chain is decreased, there is an increase in $k_{obs}$ for the fast phase. There was less of an effect on the slow phase for each of the variants, which decreased to ~2 $s^{-1}$.

In conclusion, the I135 variants have an effect upon the binding of both NADPH and the FO cofactor, Additionally, the affects upon the hydride transfer step with increasing rate constant. This is likely due to conformational changes within Fno to bring the two cofactors within a closer proximity for hydride transfer.

REFERENCES


1. DiMarco, A., Bobik, T., Wolfe, R. Unusual coenzymes of methanogenesis. *Annu Rev. Biochem.* **1990,** *59,* 355-449.
2. Bashiri, G., Rehan, A., Greenwood, D., Dickson, J., Baker, E. Metabolic engineering of cofactor $F_{420}$ production in *Mycobacterium smegmatis*. *PLoS One* **2010,** *5* (12), 1-10.
3. Isabelle, D., Simpson, D. R., Daniels, L. Large-scale production of coenzyme $F_{420}$-5,6 by using *Mycobacterium smegmatis*. *Appl. Environ. Microbiol.* **2002,** *68* (11), 5750-5755.
4. Howland, J. L. In The Biochemistry of Archaea (Archaebacteria), Kates, M., Kushner, D. J., Matheson A. T., Elsevier: Amsterdam, 1993, pp 582.
5. Tzeng, S., Wolfe, R., Bryant, M. Factor 420-dependent pyridine nucleotide-linked hydrogenase system of *Methanobacterium ruminantium*. *J. Bacteriol.* **1975,** *121* (1), 184-275.
6. Eirich, L. D., Vogels, G. D., Wolfe, R. S. Proposed structure for coenzyme $F_{420}$ from *Methanobacterium*. *Biochemistry* **1978,** *17* (22), 4583-4593.
7. Purwantini, E. Coenzyme $F_{420}$: Factors Affecting Its Purification from *Methanobacterium Thermoautotrophicum* and Its Conversion to $F_{390}$ and Effect of Temperature on the Spectral Properties of Coenzyme $F_{420}$ and Related Compounds. M.S. Thesis, University of Iowa, Iowa City, IA, **1991**.
8. Stojković, V., Perissinotti, L. L., Lee, J., Benkovic, S. J., Kohen, A. The effect of active-site isoleucine to alanine mutation on the DHFR catalyzed hydride-transfer. *Chem. Commun. (Cambridge, U. K.)* **2010,** *46* (47), 8974-8976.
9. Purwantini, E., Daniels, L. Purification of a novel coenzyme $F_{420}$-dependent glucose-6-phosphate dehydrogenase from *Mycobacterium smegmatis*. *J. Bacteriol.* **1996,** *178* (10), 2861-2866.
10. Selengut, J., Haft, D. Unexpected abundance of coenzyme F(420)-dependent enzymes in *Mycobacterium tuberculosis* and other actinobacteria. *J. Bacteriol.* **2010,** *192* (21), 5788-5886.
11. Cheeseman, P., Toms-Wood, A., Wolfe, R. S. Isolation and properties of a fluorescent compound, factor 420, from *Methanobacterium* strain M.o.H. *J. Bacteriol.* **1972,** *112* (1), 527-531.
12. Jacobson, F., Walsh, C. Properties of 7,8-didemethyl-8-hydroxy-5-deazaflavins relevant to redox coenzyme function in methanogen metabolism. *Biochemistry* **1984,** *23* (5), 979-988.
13. Walsh, C. Naturally occurring 5-deazaflavin coenzymes: biological redox roles. *Acc. Chem. Res.* **1986,** *19* (7), 216-221
14. Ferry, J. G. In Methanogenesis: Ecology, Physiology, Biochemistry & Genetics, Chapman & Hall Microbiology Series, Springer: New York, NY, 1993.
15. Lin, X., White, R. Occurrence of coenzyme $F_{420}$ and its gamma-monoglutamyl derivative in nonmethanogenic archaebacteria. *J. Bacteriol.* **1986,** *168* (1), 444-452.
16. Jones, W. J., Nagle, D. P., Whitman, W. B. Methanogens and the diversity of archaebacteria. *Microbiol. Rev.* **1987,** *51* (1), 135-177.
17. Eirich, L., Vogels, G., Wolfe, R. Distribution of coenzyme $F_{420}$ and properties of its hydrolytic fragments. *J. Bacteriol.* **1979,** *140* (1), 20-27.
18. Klenk, H., Clayton, R., Tomb, J., White, O., Nelson, K., Ketchum, K., Dodson, R., Gwinn, M., Hickey, E., Peterson, J., Richardson, D., Kerlavage, A., Graham, D., Kyrpides, N., Fleischmann, R., Quackenbush, J., Lee, N., Sutton, G., Gill, S., Kirkness, E., Dougherty, B., McKenney, K., Adams, M., Loftus, B., Peterson, S., Reich, C., McNeil, L., Badger, J., Glodek, A., Zhou, L., Overbeek, R., Gocayne, J., Weidman, J., McDonald, L., Utterback, T., Cotton, M.,Spriggs, T., Artiach, P., Kaine, B., Sykes, S., Sadow, P., D'Andrea, K.,

Bowman, C., Fujii, C., Garland, S., Mason, T., Olsen, G., Fraser, C., Smith, H., Woese, C., Venter, J. The complete genome sequence of the hyperthermophilic, sulphate-reducing archaeon *Archaeoglobus fulgidus*. *Nature* **1997,** *390* (6658), 364-370.
19. McCormick, J. R. D., Morton, G. O. Identity of cosynthetic factor I of *Streptomyces aureofaciens* and fragment FO from coenzyme $F_{420}$ of *Methanobacterium* species. *J. Am. Chem. Soc.* **1982,** *104* (14), 4014-4015.
20. Eisenreich, W., Bacher, A. Biosynthesis of 5-hydroxybenzimidazolylcobamid (factor III) in *Methanobacterium thermoautotrophicum*. *J. Biol. Chem.* **1991,** *266* (35), 23840-23849.
21. Choi, K. P., Bair, T. B., Bae, Y. M., Daniels, L. Use of transposon Tn5367 mutagenesis and a nitroimidazopyran-based selection system to demonstrate a requirement for fbiA and fbiB in coenzyme F(420) biosynthesis by *Mycobacterium bovis* BCG. *J. Bacteriol.* **2001,** *183* (24), 7058-7066.
22. Choi, K. P., Kendrick, N., Daniels, L. Demonstration that fbiC is required by *Mycobacterium bovis* BCG for coenzyme F(420) and FO biosynthesis. *J. Bacteriol.* **2002,** *184* (9), 2420-2428.
23. Rao, M. V., A THESIS SUBMITTED FOR THE DEGREE OF MASTER OF SCIENCE IN. **2009**.
24. Singh, R., Manjunatha, U., Boshoff, H. I., Ha, Y. H., Niyomrattanakit, P., Ledwidge, R., Dowd, C. S., Lee, I. Y., Kim, P., Zhang, L., Kang, S., Keller, T. H., Jiricek, J., Barry, C. E. PA-824 kills nonreplicating *Mycobacterium tuberculosis* by intracellular NO release. *Science* **2008,** *322* (5906), 1392-1395.
25. Grochowski, L. L., Xu, H.,White, R. H. Identification and characterization of the 2-phospho-L-lactate guanylyltransferase involved in coenzyme $F_{420}$ biosynthesis. Biochemistry **2008**, *47* (9), 3033-3037.
26. Taylor, M., Jackson, C., Tattersall, D., French, N., Peat, T., Newman, J., Briggs, L., Lapalikar, G., Campbell, P., Scott, C., Russell, R., Oakeshott, J. Identification and characterization of two families of $F_{420}H_2$-dependent reductases from Mycobacteria that catalyse aflatoxin degradation. *Mol. Microbiol.* **2010,** *78* (3), 561-636.
27. White, R. Biosynthesis of the methanogenic cofactors. *Vitam. Horm.* **2001,** *61*, 299-636.
28. Grochowski, L., Xu, H., White, R. An iron(II) dependent formamide hydrolase catalyzes the second step in the archaeal biosynthetic pathway to riboflavin and 7,8-didemethyl-8-hydroxy-5-deazariboflavin. *Biochemistry* **2009,** *48* (19), 4181-4189.
29. Graupner, M., Xu, H., White, R. The pyrimidine nucleotide reductase step in riboflavin and F(420) biosynthesis in archaea proceeds by the eukaryotic route to riboflavin. *J. Bacteriol.* **2002,** *184* (7), 1952-1959.
30. Eker, A. P. M., Pol, A., van der Meyden, P., Vogels, G. D. Purification and properties of 8-hydroxy-5-deazaflavin derivatives from *Streptomyces griseus*. *FEMS Microbiol. Lett.* **1980,** *8* (3), 161-165.
31. Grochowski, L. L., White, R. H. Biosynthesis of the Methanogenic Coenzymes. In Comprehensive Natural Products II, Lew, M., Hung-Wen, L., Elsevier: Oxford, 2010, pp 711-748.
32. Graupner, M., White, R. Biosynthesis of the phosphodiester bond in coenzyme F(420) in the methanoarchaea. *Biochemistry* **2001,** *40* (36), 10859-10931.
33. Mayerl, F., Piret, J., Kiener, A., Walsh, C., Yasui, A. Functional expression of 8-hydroxy-5-deazaflavin-dependent DNA photolyase from *Anacystis nidulans* in *Streptomyces coelicolor*. *J. Bacteriol.* **1990,** *172* (10), 6061-6066.
34. Daniels, L., Bakhiet, N., Harmon, K. Widespread Distribution of a 5-deazaflavin Cofactor in Actinomyces and Related Bacteria. *Syst. Appl. Microbiol.* **1985,** *6* (1), 12-17.

35. Muth, E., Mörschel, E., Klein, A. Purification and characterization of an 8-hydroxy-5-deazaflavin-reducing hydrogenase from the archaebacterium *Methanococcus voltae*. *Eur. J. Biochem.* **1987,** *169* (3), 571-578.
36. Ma, K., Linder, D., Stetter, K., Thauer, R. Purification and properties of N5,N10 methylenetetrahydromethanopterin reductase (coenzyme $F_{420}$-dependent) from the extreme thermophile *Methanopyrus kandleri*. *Arch. Microbiol.* **1991,** *155* (6), 593-1193.
37. McCormick, J., Morton, G. O. Identity of cosynthetic factor I of *Streptomyces aureofaciens* and fragment FO from coenzyme $F_{420}$ of *Methanobacterium* species. *J. Am. Chem. Soc.* **1982,** *104* (14), 4014-8029.
38. Eker, A., Hessels, J., Van de Velde, J. Photoreactivating enzyme from the green alga *Scenedesmus acutus*. Evidence for the presence of two different flavin chromophores. *Biochemistry* **1988,** *27*, 1758-3523.
39. Widdel, F., Wolfe, R. Expression of secondary alcohol dehydrogenase in methanogenic bacteria and purification of the $F_{420}$-specific enzyme from *Methanogenium thermophilum* strain TCI. *Arch. Microbiol.* **1989,** *152* (4), 322-650.
40. Walsh, C., Jacobson, F, Ryerson, C. C. Flavin Coenzyme Analogs as Probes of Flavoenzyme Reaction Mechanisms. In Biomimetic Chemistry. Dolphin, D., McKenna, C., Murakami, Y., Tabushi, I. Advances in Chemistry, American Chemical Society, **1980**, *191*, 119-138.
41. Van de Wijngaard, W., vermey, P., van der Drift, C. Formation of factor 390 by cell extracts of *Methanosarcina barkeri*. *J. Bacteriol.* **1991,** *173* (8), 2710-2711.
42. Thauer, R. K., Kaster, A.-K. K., Goenrich, M., Schick, M., Hiromoto, T., Shima, S. Hydrogenases from methanogenic archaea, nickel, a novel cofactor, and $H_2$ storage. *Annu. Rev. Biochem.* **2010,** *79,* 507-536.
43. Fox, J. A., Livingston, D. J., Orme-Johnson, W. H., Walsh, C. T. 8-Hydroxy-5-deazaflavin-reducing hydrogenase from *Methanobacterium thermoautotrophicum*: 1. Purification and characterization. *Biochemistry* **1987,** *26* (14), 4219-4227.
44. Aufhammer, S., Warkentin, E., Ermler, U., Hagemeier, C., Thauer, R., Shima, S. Crystal structure of methylenetetrahydromethanopterin reductase (Mer) in complex with coenzyme $F_{420}$: Architecture of the $F_{420}$/FMN binding site of enzymes within the nonprolyl cis-peptide containing bacterial luciferase family. *Protein Sci.* **2005,** *14* (7), 1840-1849.
45. Vaupel, M., Thauer, R. K. Coenzyme $F_{420}$-Dependent N5, N10-Methylenetetrahydromethanopterin Reductase (Mer) from *Methanobacterium Thermoautotrophicum* Strain Marburg. *Eur. J. Biochem.* **1995,** *231* (3), 773-778.
46. Te Brömmelstroet, B., Hensgens, C., Keltjens, J., van der Drift, C., Vogels, G. Purification and properties of 5,10-methylenetetrahydromethanopterin reductase, a coenzyme $F_{420}$-dependent enzyme, from *Methanobacterium thermoautotrophicum* strain delta H. *J. Biol. Chem.* **1990,** *265* (4), 1852-1859.
47. Rhodes, P., Winskill, N., Friend, E., Warren, M. Biochemical and genetic characterization of *Streptomyces rimosus* mutants impaired in oxytetracycline biosynthesis. *J. Gen. Microbiol.* **1981,** *124,* 329.
48. Sancar, A., Sancar, G. DNA repair enzymes. *Annu. Rev. Biochem.* **1988,** *57*, 29-96.
49. Jones, J., Stadtman, T. Reconstitution of a formate-$NADP^+$ oxidoreductase from formate dehydrogenase and a 5-deazaflavin-linked $NADP^+$ reductase isolated from *Methanococcus vannielii*. *J. Biol. Chem.* **1980,** *255* (3), 1049-1102.
50. Zeikus, J., Fuchs, G., Kenealy, W., Thauer, R. Oxidoreductases involved in cell carbon synthesis of *Methanobacterium thermoautotrophicum*. *J. Bacteriol.* **1977,** *132* (2), 604-617.

51. Widdel, F., Rouviere, P., Wolfe, R. Classification of secondary alcohol-utilizing methanogens including a new thermophilic isolate. *Arch. Microbiol.* **1988,** *150* (5), 477-958.
52. Bleicher, K., Zellner, G., Winter, J. Growth of methanogens on cyclopentanol/$CO_2$ and specificity of alcohol dehydrogenase. *FEMS Microbiol. Lett.* **1989,** *59* (3), 307-619.
53. Frimmer, U., Widdel, F. Oxidation of ethanol by methanogenic bacteria. *Arch. Microbiol.* **1989,** *152* (5), 479-962.
54. Weimer, P., Zeikus, J. Acetate assimilation pathway of *Methanosarcina barkeri*. J. Bacteriol. **1979,** *137* (1), 332-341.
55. Widdel, F. Growth of methanogenic bacteria in pure culture with 2-propanol and other alcohols as hydrogen donors. *Appl. Environ. Microbiol.* **1986,** *51* (5), 1056-1118.
56. Aufhammer, S., Warkentin, E., Berk, H., Shima, S., Thauer, R., Ermler, U. Coenzyme binding in $F_{420}$-dependent secondary alcohol dehydrogenase, a member of the bacterial luciferase family. *Structure (Oxford, U. K.)* **2004,** *12* (3), 361-431.
57. Bashiri, G., Squire, C. J., Moreland, N. J., Baker, E. N. Crystal structures of $F_{420}$-dependent glucose-6-phosphate dehydrogenase FGD1 involved in the activation of the anti-tuberculosis drug candidate PA-824 reveal the basis of coenzyme and substrate binding. *J. Biol. Chem.* **2008,** *283* (25), 17531-17541.
58. Bashiri, G., Squire, C., Baker, E., Moreland, N. Expression, purification and crystallization of native and selenomethionine labeled *Mycobacterium tuberculosis* FGD1 (Rv0407) using a *Mycobacterium smegmatis* expression system. *Protein Expression Purif.* **2007,** *54* (1), 38-82.
59. Dudley Eirich, L., Dugger, R. S. Purification and properties of an $F_{420}$-dependent NADP reductase from *methanobacterium thermoautotrophicum*. *Biochim. Biophys. Acta* **1984,** *802* (3), 454-458.
60. Warkentin, E., Mamat, B., Sordel-Klippert, M., Wicke, M., Thauer, R., Iwata, M., Iwata, S., Ermler, U., Shima, S. Structures of $F_{420}H_2$:$NADP^+$ Oxidoreductase with and without its substrates bound. *EMBO J.* **2001,** *20* (23), 6561-6570.
61. Yamazaki, S., Tsai, L. Purification and properties of 8-hydroxy-5-deazaflavin-dependent $NADP^+$ reductase from *Methanococcus vannielii*. *J. Biol. Chem.* **1980,** *255* (13), 6462-6465.
62. Berk, H., Thauer, R. Function of coenzyme $F_{420}$-dependent NADP reductase in methanogenic archaea containing an NADP-dependent alcohol dehydrogenase. *Arch. Microbiol.* **1997,** *168* (5), 396-402.
63. Hossain, M. S., Le, C. Q., Joseph, E., Nguyen, T. Q. Convenient synthesis of deazaflavin cofactor FO and its activity in $F_{420}$-dependent NADP reductase. *Org. Biomol. Chem.* **2015,** *13* (18), 5082-5085.
64. Yamazaki, S., Tsai, L., Stadtman, T. Analogues of 8-hydroxy-5-deazaflavin cofactor: relative activity as substrates for 8-hydroxy-5-deazaflavin-dependent $NADP^+$ reductase from *Methanococcus vannielii*. *Biochemistry* **1982,** *21* (5), 934-943.
65. Dudley Eirich, L., Dugger, R. S. Purification and properties of an $F_{420}$-dependent NADP reductase from *methanobacterium thermoautotrophicum*. *Biochim. Biophys. Acta* **1984,** *802* (3), 454-458.
66. Murzin, A. G., Brenner, S. E., Hubbard, T. SCOP: a structural classification of proteins database for the investigation of sequences and structures. *J. Mol. Biol.* **1995,** *247* (4), 536-540.
67. Berk, H., Thauer, R. K. $F_{420}H_2$:$NADP^+$ Oxidoreductase from *Methanobacterium thermoautotrophicum*: Identification of the encoding gene via functional overexpression in *Escherichia coli*. *FEBS Lett.* **1998,** *438* (1-2), 124-126.

68. Arora, K., Brooks, C. L., III. Functionally important conformations of the Met20 loop in dihydrofolate reductase are populated by rapid thermal fluctuations. *J. Am. Chem. Soc.* **2009,** *131* (15), 5642-5647.
69. Stojković, V., Perissinotti, L. L., Lee, J., Benkovic, S. J., Kohen, A. The effect of active-site isoleucine to alanine mutation on the DHFR catalyzed hydride-transfer. *Chem. Commun. (Cambridge, U. K.)* **2010,** *46* (47), 8974-8976.
70. Kohen, A., Klinman, J. P..Hydrogen tunneling in biology. Chemistry & Biology **1999**.
71. Wit, L. E. A., Eker, A. P. M. 8-Hydroxy-5-deazaflavin-dependent electron transfer in the extreme halophile *Halobacterium cutirubrum*. *FEMS Microbiol. Lett.* **1987,** *48*, 121-125.
72. Kunow, J., Schwörer, B., Stetter, K. O., Thauer, R. K. A $F_{420}$-dependent NADP reductase in the extremely thermophilic sulfate-reducing *Archaeoglobus fulgidus*. *Arch. Microbiol.* **1993,** *160* (3), 199-205.
73. Eker, A. P. M., Hessels, J. K. C., Meerwaldt, R. Characterization of an 8-hydroxy-5-deazaflavin: NADPH oxidoreductase from *Streptomyces griseus*. *Biochim. Biophys. Acta* **1989,** *990* (1), 80-86.
74. Levitzki, A., Koshland, D. E., Jr. The role of negative cooperativity and half-of-the-sites reactivity in enzyme regulation. *Curr. Top. Cell. Regul.* **1975,** *10,* 1-40.
75. Ferry, J. G. Biochemistry of methanogenesis. *Crit. Rev. Biochem. Mol. Biol.* **1992,** *27* (6), 473-503
76. Decamps, L., Philmus, B., Benjdia, A., White, R., Begley, T., Berteau, O. Biosynthesis of F0, precursor of the $F_{420}$ cofactor, requires a unique two radical-SAM domain enzyme and tyrosine as substrate. *J. Am. Chem. Soc.* **2012,** *134* (44), 18173-18176.
77. Van, L. Q., Schwarzkopf, B., Bacher, A. Biosynthesis of 7, 8-didemethyl-8-hydroxy-5-deazariboflavin, the chromophoric moiety of coenzyme $F_{420}$. *J. Am. Chem. Soc.* **1985,** 107 (26), 8300-8301.
78. Glas, A. F., Maul, M. J., Cryle, M., Barends, T. R., Schneider, S., Kaya, E., Schlichting, I., Carell, T. The archaeal cofactor F0 is a light-harvesting antenna chromophore in eukaryotes. *Proc. Natl. Acad. Sci. U. S. A.* **2009,** *106* (28), 11540-11545.
79. O'Brien, D. E., Weinslock, L. T., Cheng, C. C. Synthesis of 10-deazariboflavin and related 2,4-Dioxopyrimido[4,5-*b*] quinolines. *J. Heterocycl. Chem.* **1970**, *7* (1), 99-105.
80. Ashton, W. T., Brown, R. D., Jacobson, F., Walsh, C. Synthesis of 7,8-didemethyl-8-hydroxy-5-deazariboflavin and confirmation of its identity with the deazaisoalloxazine chromophore of Methanobacterium redox coenzyme $F_{420}$. *J. Am. Chem. Soc.* **1979,** *101* (15), 4419-4420.
81. Ashton, W. T., Brown, R. D., Synthesis of 8-demethyl-8-hydroxy-5-deazariboflavins. *J. Heterocycl. Chem.* **1980,** *17* (8), 1709-1712.
82. Tanaka, K., Kimachi, T., Kawase, M. First total synthesis of redox coenzyme factor 420. *J. Chem. Soc., Chem. Commun.* **1988,** 524-526.
83. Tetsutaro, K., Masahiro, K., Shinsuke, M., Kiyoshi, T., Fumio, Y. First total synthesis of coenzyme factor 420. *J. Chem. Soc., Perkin Trans. 1* **1990,** 253-256.
84. Janda, M., Hemmerich, P. 5-Deaza-and 5-Thiariboflavins: A Simple Pathway to Antimetabolites of Vitamin B2. *Angew. Chem. Int. Ed.* **1976,** *15,* 443–444.
85. Chaudhuri, S., Batabyal, S., Polley, N., Pal, S. K. Vitamin B2 in Nanoscopic Environments under Visible Light: Photosensitized Antioxidant or Phototoxic Drug. *J. Phys. Chem. A* **2014,** *118* (22), 3934-3943.
86. Carlson, E. E., Kiessling, L. L. Improved chemical syntheses of 1-and 5-deazariboflavin. *J. Org. Chem.* **2004**.
87. Manstein, D. J., Pai, E. F., Schopfer, L. M., Massey, V. Absolute stereochemistry of flavins in enzyme-catalyzed reactions. *Biochemistry* **1986,** *25* (22), 6807-6816.

88. Schlueter, J. A., Redfern, P. C., Curtiss, L., Amine, K. Understanding the redox shuttle stability of 3, 5-di-tert-butyl-1, 2-dimethoxybenzene for overcharge protection of lithium-ion batteries. *J. Power Sources* **2010,** *195* (15), 4957-4962.
89. Knaggs, S., Malkin, H., Osborn, H. M. I., Williams, N. A. O., Yaqoob, P. New prodrugs derived from 6-aminodopamine and 4-aminophenol as candidates for melanocyte-directed enzyme prodrug therapy (MDEPT). *Org. Biomol. Chem.* **2005,** *3* (21), 4002-4010.
90. Artigas, G., Marchán, V. Synthesis of Janus Compounds for the Recognition of GU Mismatched Nucleobase Pairs. *J. Org. Chem.* **2013,** *78* (21), 10666-10677.
91. F. Yoneda, patft.uspto.gov, **1986**, 544/250; 544/313, C07D 239/00 (20060101); C07D 239/553 (20060101); C07D 471/00 (20060101); C07D 471/04 (20060101); C07D 471/04 (); C07D –;544/250,313,314.
92. Bradford, M. M. A rapid and sensitive method for the quantitation of microgram quantities of protein utilizing the principle of protein-dye binding. *Anal. Biochem.* **1976,** *72* (1,2), 248-254.
93. Laemmli, U. K. Cleavage of structural proteins during the assembly of the head of bacteriophage T4. *Nature* **1970,** *227,* 680-685.
94. Lambin, P., Fine, J. M. Molecular weight estimation of proteins by electrophoresis in linear polyacrylamide gradient gels in the absence of denaturing agents. *Anal. Biochem.* **1979,** *98* (1), 160-168.
95. Fairbanks, G., Steck, T. L., Wallach, D. F. H. Electrophoretic analysis of the major polypeptides of the human erythrocyte membrane. *Biochemistry* **1971,** *10* (13), 2606-2617.
96. Wenrich, B. R., Trumbo, T. A. Interaction of nucleic acids with Coomassie Blue G-250 in the Bradford assay. *Anal. Biochem.* **2012,** *428* (2), 93-95.
97. Gasteiger, E., Hoogland, C., Gattiker, A., Duvaud, S., Wilkins, M. R., Appel, R. D., Bairoch, A. Protein identification and analysis tools on the ExPASy server. In The Proteomics Protocols Handbook, Walker, J. M. Humana Press Inc: Totowa, NJ. **2005**, 571-607.
98. Dumon-Seignovert, L., Cariot, G., Vuillard, L. The toxicity of recombinant proteins in *Escherichia coli*: a comparison of overexpression in *BL21 (DE3), C41 (DE3),* and *C43 (DE3). Protein Expression Purif.* **2004,** *37* (1), 203-206.
99. Burgess, R. R. Protein precipitation techniques. Methods Enzymol. **2009**, 331-342.
100. Conway, A., Koshland, D. E. Negative cooperativity in enzyme action. Binding of diphosphopyridine nucleotide to glyceraldehyde-3-phosphate dehydrogenase. *Biochemistry* **1968,** *7* (11), 4011-4023.
101. Levitzki, A., Koshland, D. E. Negative cooperativity in regulatory enzymes. *Proc. Natl. Acad. Sci. U. S. A.* **1969,** *62* (4), 1121-1128.
102. Nijvipakul, S., Ballou, D. P., Chaiyen, P. Reduction kinetics of a flavin oxidoreductase LuxG from *Photobacterium leiognathi* (TH1): Half-sites reactivity. *Biochemistry* **2010,** *49* (43), 9241-9248.
103. Binevski, P. V., Sizova, E. A., Pozdnev, V. F., Kost, O. A. Evidence for the negative cooperativity of the two active sites within bovine somatic angiotensin-converting enzyme. *FEBS Lett.* **2003,** *550* (1), 84-88.
104. Waight, R. D., Leff, P., Bardsley, W. G. Steady-state kinetic studies of the negative co-operativity and flip-flop mechanism for *Escherichia coli* alkaline phosphatase. **1977**, *167*, 787-798.
105. Megarity, C. F., Gill, J. R. E., Caraher, M. C., Stratford, I. J, Nolan, K. A., Timson, D. J. The two common polymorphic forms of human NRH-quinone oxidoreductase 2 (NQO2) have different biochemical properties. *FEBS Lett.* **2014,** *588* (9), 1666-1672.

106. Kurganov, B. I. Analysis of negative cooperativity for glutamate dehydrogenase. *Biophys. Chem.* **2000,** *87* (2,3), 185-199.
107. Slavens, K. D., Brown, T. R., Barakat, K. A., Cundari, T. R. Valine 44 and valine 45 of human glutathione synthetase are key for subunit stability and negative cooperativity. *Biochem. Biophys. Res. Commun.* **2011,** 410 (3), 597-601.
108. Abeliovich, H. An empirical extremum principle for the hill coefficient in ligand-protein interactions showing negative cooperativity. *Biophys. J.* **2005**, *89* (1), 76-79.
109. Hartman, J. H., Knott, K., Miller, G. P. CYP2E1 hydroxylation of aniline involves negative cooperativity. *Biochem. Pharmacol.* **2014**, *87* (3), 523-533.
110. Henis, Y. I., Levitzki, A. Mechanism of negative cooperativity in glyceraldehyde-3-phosphate dehydrogenase deduced from ligand competition experiments. *Proc. Natl. Acad. Sci. U. S. A.* **1980**, *77* (9), 5055-5059.
111. Klein, R. A. Lack of intramolecular hydrogen bonding in glucopyranose: vicinal hydroxyl groups exhibit negative cooperativity. *Chem. Phys. Lett.* **2006**, *433* (1), 165-169.
112. Mishanina, T. V., Koehn, E. M., Kohen, A. Mechanisms and inhibition of uracil methylating enzymes. *Bioorg. Chem.* **2012,** *43,* 37-43.
113. Koehn, E. M., Kohen, A. Flavin-dependent thymidylate synthase: a novel pathway towards thymine. *Arch. Biochem. Biophys.* **2010,** *493* (1), 96-102.
114. Miller, S. M., Massey, V., Jr, W. C. H., Ballou, D. P. Communication between the active sites in dimeric mercuric ion reductase: an alternating sites hypothesis for catalysis. *Biochemistry* **1991,** *30* (10), 2600-2612.
115. Foster, T. J. Plasmid-determined resistance to antimicrobial drugs and toxic metal ions in bacteria. *Microbiol. Rev.* **1983,** *47* (3), 361-409.
116. Koshland, D. E., Jr, Nemethy, G., Filmer, D. Comparison of experimental binding data and theoretical models in proteins containing subunits. *Biochemistry* **1966,** *5* (1), 365-385.
117. Le, C. Q., Joseph, E., Nguyen, T., and Johnson-Winters, K. A new purification protocol of a novel $F_{420}$ cofactor dependent enzyme: $F_{420}H_2$:$NADP^+$ Oxidoreductase. *Plos One* **2015***,* submitted.
118. Möller, M., Denicola, A. Study of protein-ligand binding by fluorescence. *Biochem. Mol. Biol. Educ.* **2002**, *30* (5), 309-312.
119. Neet, K. E. Cooperativity in enzyme function: equilibrium and kinetic aspects. *Methods Enzymol.* **1994,** *249,* 519-567.
120. Wharton, C., Eisenthal, R. Complex Kinetics and Cooperativity. *Molecular Enzymology,* First Edition, Tertiary Level Biology, Springer: United States, 1981, pp 169-203.
121. Fenselau, A. Structure-Function Studies on Glyceraldehyde 3-Phosphate Dehydrogenase IV. SUBUNIT INTERACTIONS OF THE RABBIT MUSCLE AND YEAST ENZYMES. *J. Biol. Chem.* **1972,** *217* (4), 1074-1079.
122. Vijlder, J. J. M., Boers, W., Slater, E. C. Binding and properties of $NAD^+$ in glyceraldehydephosphate dehydrogenase from lobster-tail muscle. *Biochim. Biophys. Acta* **1969,** *191* (2), 214-220.
123. Sturtevant, J. M., Velick, S. F., Baggott, J. P. Thermodynamics of nicotinamide-adenine dinucleotide addition to the glyceraldehyde 3-phosphate dehydrogenases of yeast and of rabbit skeletal muscle. An equilibrium and calorimetric analysis over a range of temperatures. *Biochemistry* **1971,** *10* (5), 779-786.
124. Chappelet-Tordo, D., Iwatsubo, M., Lazdunski, M. Negative cooperativity and half of the sites reactivity. Alkaline phosphatases of *Escherichia coli* with $Zn^{2+}$, $Co^{2+}$, $Cd^{2+}$, $Mn^{2+}$ and $Cu^{2+}$ ions in the active sites. *Biochemistry* **1974,** *13* (18), 3754-3762.

## BIOGRAPHICAL INFORMATION

Cuong Quang Le graduated from the University of Texas at Arlington with a bachelor's degree in biology in 2009. He continued his undergraduate studies and graduated with a second bachelor's degree in biological chemistry in 2010. With a high interest in enzyme kinetics he directly joined Dr. Kayunta Johnson-Winters' research group for the BS-Ph.D. degree program in 2010. The focus of his research is to study the hydride transfer reactions of $F_{420}$ dependent enzymes, specifically Fno, using site-directed mutagenesis, steady-state and pre-steady state kinetic methods. His plan is to work in a national laboratory and eventually come back to academia.